Breast Cancer Detection Using Microwave Low-Frequency Metasurface-Based Techniques

by

Mauricio Hernández

A thesis
presented to the University of Waterloo
in fulfillment of the
thesis requirement for the degree of
Doctor of Philosophy
in
Electrical and Computer Engineering

Waterloo, Ontario, Canada, 2025

© Mauricio Hernádez 2025

Examining Committee Membership

The following served on the Examining Committee for this thesis. The decision of the Examining Committee is by majority vote.

External Examiner:	Mohammad Zarifi Professor, School of Engineering, Faculty of Applied Science, University of British Columbia
Supervisor(s):	Omar M. Ramahi Professor, Dept. of Electrical and Computer Engineering, University of Waterloo
Internal Member:	Alfred Yu Professor, Dept. of Electrical and Computer Engineering, Assistant Vice-President (Research and International) University of Waterloo
Internal Member:	George Shaker Associate Professor, Dept. of Electrical and Computer Engineering, University of Waterloo
Internal-External Member:	Parsin Haji Reza Associate Professor, Dept. of System Design Engineering, University of Waterloo

Author's Declaration

I hereby declare that I am the sole author of this thesis. This is a true copy of the thesis, including any required final revisions, as accepted by my examiners.

I understand that my thesis may be made electronically available to the public.

Abstract

Breast cancer has become an important global public health issue and is the leading cause of death among women. Early detection plays a pivotal role in the effective treatment of breast cancer. Microwave modalities offer a promising alternative because they allow deep penetration into the breast, resulting in an adequate contrast between the electrical properties of the malignant and benign breast tissue. Microwaves are also a mature technique that is relatively affordable and non-ionizing, thus addressing many of the deficiencies of traditional methods.

In the first part of this study, we use computer biomechanics finite element simulation software (FEBio) to simulate the physical compression of anatomically realistic breast phantoms. The phantoms are 3D anatomically realistic and made up of MRI images. The compressed breast models derived from this part of this study will create a realistic scenario for the electromagnetic simulation in CST software. We successfully compressed a set of realistic phantoms, and these accurate compressed models created several natural scenarios to test the microwave technology developed in this investigation.

The second part of this work introduces an electromagnetic energy scanning technique with a specific application to detect breast cancer. The technique is based on a field detector probe inspired by the concept of a metasurface composed of an ensemble of electrically small elements where a single element represents the field detector. This novel probe provides a resolution that cannot be matched by either electrically small probes or resonance-based probes that have dimensions comparable to the wavelength. The field emanating from a specific structure, such as a human female breast, can be scanned by the proposed probe to achieve a resolution in the millimeter range while operating in the low-microwave frequency spectrum. The probe was tested numerically, and a prototype was tested experimentally, demonstrating its effectiveness in providing a field resolution of approximately 5 mm.

The third part of this thesis introduces a novel metasurface sensor designed to detect breast cancer by operating at sub-microwave frequency. Each cell of the metasurface gives rise to a voltage difference that can be measured at the back of the metasurface. Thus, the metasurface has the ability to generate an impression that relates to the constituents of the breast. Simulations were performed to capture and analyze a collection of images using artificial intelligence methodologies. The findings of this testing stage demonstrated the device's capability to identify anomalies in the breast that may or may not be cancerous. This concept was also extended and validated in an experimental trial; the fabricated device was able to detect a small PEC sphere of 10 mm diameter. Both results, simulation and experimental test, show the potential of this device in successfully detecting breast cancer.

This study also explores, in part four, the classification between healthy and unhealthy breast tissue by integrating a microwave probe and a self-organized algorithm. This system

collects the reflection coefficients from multiple breast samples where there may or may not be the presence of cancerous tissue. The probe showed remarkable capability to detect the changes in dielectric properties in the breast tissue, and the self-organized algorithm addressed the challenge of classifying this complex data overpassing traditional machine learning methods. We tested the capabilities of this detection system under simulation and experimental validation.

Acknowledgements

I express my deepest gratitude to my supervisor, Professor Omar M. Ramahi. I am incredibly grateful for his guidance, support, encouragement, and insightful advice during my Ph.D. journey.

I also extend my gratitude to the committee members, Professors Alfred Yu, George Shaker, and Parsin Haji Reza, for their thorough review of my thesis, their constructive feedback, and their invaluable time serving on my PhD examination committee.

I am extremely grateful to Professor Mohammad Zarifi for serving as an external examiner, for dedicating his valuable time to reading my thesis, and for providing helpful feedback.

I would like to express my sincere appreciation to my colleagues, Hamid Akbari Chelaresi and Ghazaleh Tashtarian, for their invaluable support and encouragement.

I am grateful to the team of the Advance Concepts Research Laboratory (ARC) for our collaborative work throughout this sojourn https://aer-laboratory.site123.me/research-team.

I would like to thank the team at the Electrical and Computer Engineering Department, particularly the Network Systems Department, for their assistance with hardware and software needs.

I want to thank my wife for her constant support and motivation throughout my academic journey. Her involvement has been essential, and I deeply appreciate her commitment.

I am sincerely grateful to the Advanced Human Capital Program of the National Research and Development Agency for providing me with the opportunity and support of the Chilean National Scholarship Program for Graduate Studies.

Dedication

To Marietta and my community.

Table of Contents

Examining Committee ii

Author's Declaration iii

Abstract iv

Acknowledgements vi

Dedication vii

List of Figures xi

List of Tables xx

List of Abbreviations xxi

1 Introduction 1

1.1 Overview 1

1.2 Microwave Imaging 3

1.2.1 Microwave imaging tomography 4

1.2.2 Microwave imaging radar-based 5

1.3 Machine Learning - Convolutional Neural Network 6

1.4 Realistic phantoms for electromagnetic simulations 8

1.5 Relevant theoretical framework . . . 14
1.5.1 Wave propagation and Skin penetration in materials . . . 14
1.5.2 Metasurface . . . 17
1.6 Problem statement . . . 18
1.7 Research motivation . . . 19
1.8 Research Objectives . . . 19
1.9 Thesis outline . . . 20

2 Simulation of the physical compression of a anatomically-realistic MRI-derived numerical breast phantom 21

2.1 Introduction . . . 21
2.2 Methods . . . 22
2.3 Simulation of the compression of the realistic breast phantom . . . 26
2.3.1 Compression results of the realistic breast phantom - Class 3- Heterogeneously Dense Phantom 3 Breast ID: 062204 . . . 29
2.3.2 Compression results of the realistic breast phantom - Class 4 - Very Dense Phantom 1 Breast ID: 012304 . . . 30
2.3.3 Compression results of the realistic breast phantom - Class 1- Mostly Fatty Phantom 1 Breast ID: 071904 . . . 32
2.4 Conclusion . . . 34

3 Microwave low frequency scanning in the near-field for cancer detection 36

3.1 Introduction . . . 36
3.2 Theory and application methodology . . . 37
3.3 Numerical simulation . . . 40
3.4 Experimental results . . . 50
3.5 Future Implementation . . . 59
3.6 Conclusion . . . 59

4 Microwave low frequency imaging in the near-field for cancer detection **61**
4.1 Introduction . . . 61
4.2 Theory and application methodology . . . 62
4.3 Numerical results . . . 63
4.4 Application of the Convolutional Neural Network . . . 80
4.5 Experimental verification . . . 82
4.6 Conclusion . . . 86

5 Breast cancer detection using a microwave probe and self-organized algorithm **87**
5.1 Introduction . . . 87
5.2 Theory and application methodology . . . 88
5.3 Probe design . . . 90
5.4 Self-organized Cellular automata classifier with genetic algorithm . . . 95
5.4.1 Self-Organized Cellular Automata . . . 96
5.4.2 Genetic algorithm . . . 100
5.5 Simulation results . . . 101
5.6 Experimental results . . . 106
5.7 Conclusion . . . 111

6 Conclusion and Future Work **112**
6.1 Accomplished Work . . . 112
6.2 List of Publications . . . 113
6.3 Future Work . . . 114

References **116**

List of Figures

1.1 Comparison between X-ray mammography, MRI, Ultrasound, and MW 3

1.2 The MW techniques, passive, hybrid and active approaches 4

1.3 CNN visualization: input image 30x30 pixels, two Convoluiton layers (CL), one max-Pooling layers (PL), one Fully connected layers (FCL), and four outputs . . 7

1.4 Real part of the relative permittivity (ϵ_r) between tumorous and normal tissue, using Cole-Cole model parameters presented in Table 1.2, data from 0.5 to 1 GHz 9

1.5 ARBP Class 1 - Mostly Fatty Phantom 1 Breast ID: 071904. 1.5a XY Slice. 1.5b XZ Slice. 1.5c YZ Slice. 11

1.6 ARBP Class 1 - Mostly Fatty Phantom 1 Breast ID: 071904 3D representation. 1.6a Entire 3D view. 1.6b XZ section view. 1.6c XY section view. 1.6d YZ section view. 12

1.7 ARBP Class 4 Very Dense Phantom 1 Breast ID: 012304. 1.7a XY Slice. 1.7b XZ Slice. 1.7c YZ Slice. 12

1.8 ARBP Class 4- Very Dense Phantom 1 Breast ID: 012304. 1.8a Entire 3D view. 1.8b XZ section view. 1.8c XY section view. 1.8d YZ section view. 12

1.9 Anatomically Realistic Breast Phantoms (ARBP) Dataset - 12.1 % and 28.7% average and minimum in fraction by mass respectively - Nine samples with z-axis cutting plane for EM simulation in CST ®: 1.9a, 1.9b, 1.9c, 1.9d, 1.9e, 1.9f, 1.9g, 1.9h, and 1.9i 14

1.10 Penetration into normal breast tissue using parameters presented in Table 1.2, data from 0.5 to 1 GHz 17

2.1 Example of the original layers tissues of the realistic breast phantom. 2.1a fibroglandular type 1, 2.1b fibroglandular type 2, 2.1c fibroglandular type 3, 2.1g transitional tissue, 2.1d fat type 1, 2.1e fat type 2, 2.1f fat type 3, 2.1h 3D view of the all fat, fibro, and transitional layers, and 2.1i skin tissue. 23

2.2 3D Slicer view: Skin, Fatty, and Fibro Material views for Anatomically Realistic Breast Phantoms (ARBP) ACR Class 3- Heterogeneously Dense Phantom 3 Breast ID: 062204. 2.2a Axial view. 2.2b Coronal view. 2.2c Sagittal view. 2.2d 3D view. 24

2.3 Skin, Fatty, and Fibro STL files Material views for ARBP ACR Class 3- Heterogeneously Dense Phantom 3 Breast ID: 062204. 2.3a 3D Skin STL file. 2.3b 3D Fibro STL file. 2.3c 3D Fatty STL file. 25

2.4 Process for prepare ARBP to simulate the physical compression of the breast phantoms. From the left to the right: 25

2.5 Meshing in TetGen of Skin, Fatty, and Fibro Material views for ARBP ACR Class 3- Heterogeneously Dense Phantom 3 Breast ID: 062204. 2.5a TetGen mesh Skin geometry. 2.5b TetGen mesh Fatty geometry. 2.5c TetGen mesh Fibro geometry. 2.5d TetGen mesh Complete geometry. 27

2.6 Illustration of the initial and end compression simulation of ARBP ACR Class 3- Heterogeneously Dense Phantom 3 Breast ID: 062204. 2.6a Geometry TetGen initial position and Contact position. 2.6b Geometry TetGen Applied force 121.34 N. 28

2.7 Uncompressed view of the ARBP ACR Class 3- Heterogeneously Dense Phantom 3 Breast ID: 062204. 2.7a Geometry TetGen uncompressed fat . 2.7b Geometry TetGen uncompressed fibro. 2.7c Geometry TetGen uncompressed skin. 2.7d Complete view of the uncompressed phantom. 29

2.8 Compressed view of the ARBP ACR Class 3- Heterogeneously Dense Phantom 3 Breast ID: 062204. 2.8a Geometry TetGen compressed fat . 2.8b Geometry TetGen compressed fibro. 2.8c Geometry TetGen compressed skin. 2.8d Complete view of the compressed phantom. 29

2.9 Force vs position paddle top over Skin, Fatty, and Fibro Material for ARBP ACR Class 3- Heterogeneously Dense Phantom 3 Breast ID: 062204 30

2.10 Uncompressed view of the ARBP ACR Class 4 - Very Dense Phantom 1 Breast ID: 012304. 2.10a Geometry TetGen uncompressed fat. 2.10b Geometry TetGen uncompressed ffibro. 2.10c Geometry TetGen uncompressed skin. 2.10d Complete view of the uncompressed phantom. 31

2.11 Compressed view of the ARBP ACR Class 4 - Very Dense Phantom 1 Breast ID: 012304. 2.11a Geometry TetGen compressed fat . 2.11b Geometry TetGen compressed ffibro. 2.11c Geometry TetGen compressed skin. 2.11d Complete view of the compressed phantom. 31

2.12 Force vs position paddle top over Skin, Fatty, and Fibro Material for ARBP ACR Class 4 - Very Dense Phantom 1 Breast ID: 012304 32

2.13 Uncompressed view of the ARBP ACR Class 1- Mostly Fatty Phantom 1 Breast ID: 071904. 2.13a Geometry TetGen uncompressed fat . 2.13b Geometry TetGen uncompressed ffibro. 2.13c Geometry TetGen uncompressed skin. 2.13d Complete view of the uncompressed phantom. 33

2.14 Compressed view of the ARBP ACR Class 1- Mostly Fatty Phantom 1 Breast ID: 071904. 2.14a Geometry TetGen compressed fat . 2.14b Geometry TetGen compressed ffibro. 2.14c Geometry TetGen compressed skin. 2.14d Complete view of the compressed phantom. 33

2.15 Force vs position paddle top over Skin, Fatty, and Fibro Material for ARBP ACR Class 1- Mostly Fatty Phantom 1 Breast ID: 071904 34

3.1 RF-Scanning energy concept illustration. Composed by: MW energy source, the Object Under Test (OUT), and the plane to be scanned 38

3.2 MW Absorber circuit model. Z_d is the equivalent impedance of the substrate, H_s thickness of the substrate, and Z_{UC} is the impedance of the UC. 39

3.3 ELC resonance frequency at 0.7 GHz, perspective, front, and back view. 3.3a ELC perspective view. Top and bottom dielectric material FR-4, and inter-media material polycarbonate. Resonance frequency at 0.7 GHz. 3.3b ELC top view. 3.3c ELC bottom view 41

3.4 Simulation results of the UC ELC absorption, reflection, and transmission 42

3.5 Simulation results ELC efficiency, data from 0.5 to 0.9 GHz, case FR-4 and polycarbonate 43

3.6 Simulation results ELC efficiency, data from 0.5 to 0.9 GHz. , case FR-4. 44

3.7 Simulation results ELC efficiency, data from 0.5 to 0.9 GHz. Case TMM13i 45

3.8 CST ® Simulation results using MW energy scanning 5x5 sensor, and heterogeneously dense breast identified as a Class 3 phantom (I.D. 062204). 3.8a XY cut of the simulated ARBP. 3.8b Simulation in CST ®, 900 samples by scanning 30×30 positions vertically and horizontally. 3.8c HOG representation of the Figure 3.8b. 47

3.9 CST ® Simulation results using MW energy scanning 5x5 sensor, and heterogeneously dense breast identified as a Class 3 phantom (I.D. 062204) with 10 mm radius tumor. 3.9a XY cut of the simulated ARBP with 10 mm radius tumor. 3.9b Simulation in CST ®, 900 samples by scanning 30×30 positions vertically and horizontally with 10 mm radius tumor. 3.9c HOG representation of the Figure 3.9b. 48

3.10 CST ® Simulation results using MW energy scanning 5x5 sensor, and heterogeneously dense breast identified as a Class 3 phantom (I.D. 062204) with 7 mm radius tumor. 3.10a XY cut of the simulated ARBP with 7 mm radius tumor. 3.10b Simulation in CST ®, 900 samples by scanning 30×30 positions vertically and horizontally with 7 mm radius tumor. 3.10c HOG representation of the Figure 3.10b. 49

3.11 3.11a Overview RF-Scanning system hardware Composed by: 3.11b Dipole antenna operating at 700 MHz. 3.11c Phantom make of TRITON X-100, 5×5 Metasurface (MS) sensor, and MW power meter. 3.11d MW power amplifier, manual control, and stop emergency. 3.11e Signal generator. 3.11f MW Isolator. 3.11g Step motors & screws for XY-axis control. 51

3.12 MW sensor 5×5. 3.12a Top view design. 3.12b Bottom view design. 3.12c Fabricated view of MW senser of 5×5 cells. Only the center cell is designed to take the measurements from the scanning system. 53

3.13 Twelve fabricated phantoms using TRITON X-100 and distilled water. 3.13a Fabricated phantom 26% TRITON X-100 and 74% distilled water. 3.13b Fabricated phantom 28% TRITON X-100 and 72% distilled water. 3.13c Fabricated phantom 30% TRITON X-100 and 70% distilled water. 3.13d Fabricated phantom 32% TRITON X-100 and 68% distilled water. 3.13e Fabricated phantom 34% TRITON X-100 and 66% distilled water. 3.13f Fabricated phantom 36% TRITON X-100 and 64% distilled water. 3.13g Fabricated phantom 38% TRITON X-100 and 62% distilled water. 3.13h Fabricated phantom 40% TRITON X-100 and 60% distilled water. 3.13i Fabricated phantom 42% TRITON X-100 and 58% distilled water. 3.13j Fabricated phantom 44% TRITON X-100 and 56% distilled water. 3.13k Fabricated phantom 46% TRITON X-100 and 54% distilled water. 3.13l Fabricated phantom 48% TRITON X-100 and 52% distilled water 55

3.14 RF-Scanning energy system schematic diagram composed by:. 56

3.15 Experimental results using MW 5x5 sensor for scanning 60x60 pixels image plane over 110x100 mm^2. 3.15a Scanned healthy phantom, 3.15b Scanned of a phantom with a tumor of 5 mm diameter at the left, 3.15c Scanned of a phantom with a tumor of 5 mm diameter at the right, 3.15d Scanned of a phantom with a tumor of 7 mm diameter at the left, 3.15e Scanned of a phantom with a tumor of 7 mm diameter at the right, 3.15f Scanned of a phantom with a tumor of 10 mm diameter at the left, 3.15g Scanned of a phantom with a tumor of 10 mm diameter at the right. 57

3.16 CNN model architecture composed by: 58

3.17 CNN Confusion matrix of the experimental validation 59

4.1 Illustrated concept of the transmitted and received MW power 62

4.2 ELC UC design in CST ® software. 3D view, top and bottom layers. 64

4.3 ELC UC simulation results reflection coefficient s_{11} 65

4.4 absorption, reflection, and transmission of the ELC UC. $1 - R(\omega) - T(\omega)$ where $R(\omega) = |S_{11}|^2$ and $T(\omega) = |S_{21}|^2$ 66

4.5 The efficiency of the ELC corresponds to the power the resistor consumes on the bottom layer. The MW power the source delivers is 0.5 W. The graph shows on the left the value in Watts and on the right in percentage % 67

4.6 relative permittivity (ϵ_r) and relative permeability (μ_r) of the ELC cell 68

4.7 Input impedance of the ELC cell 69

4.8 Power flow of the Metasurface (MS) of 30 by 30 ELC cell simulation in software CST ® 70

4.9 MS top and bottom layers. 4.9a Top layer composed by 30x30 ELC UC of 3 mm each. 4.9b Bottom layer that holds 900 resistors in 30×30 2D array for voltage measurements 71

4.10 MS Sensor 3D view and simulation system setup. 4.10a MS 30 by 30 cells of 3 mm size. 4.10b Representation of the CST ® simulation system with electrically small loop antenna, ARBP, and MS 72

4.11 CST ® Setup of the Simulation of ACR Class 3- Heterogeneously Dense Phantom 3 Breast ID: 062204 showing the four simulated location of the PEC tumor. 4.11a location center right, 4.11b location center left, 4.11c location bottom right, 4.11d location bottom left. The z-axis position of the tumor was set for all the simulation 10 mm from the skin of the ARBP 73

4.12 Plane representations of the voltage magnitudes of the 30 by 30 resistors at the bottom of the MS using CST ® Simulation of ACR Class 3- Heterogeneously Dense Phantom 3 Breast ID: 062204. 4.12a healthy. 4.12b unhealthy with 7 mm radius PEC tumor at center right. 4.12c Representation of the algebraic difference between the voltages magnitudes of the healthy 4.12a and unhealthy 4.12b 73

4.13 Plane representations of the voltage magnitudes of the 30 by 30 resistors at the bottom of the MS using CST ® Simulation of ACR Class 3- Heterogeneously Dense Phantom 3 Breast ID: 062204. 4.13a healthy. 4.13b unhealthy with 7 mm radius PEC tumor at center left. 4.13c Representation of the algebraic difference between the voltages magnitudes of the healthy 4.13a and unhealthy 4.13b . . . 74

4.14 Plane representations of the voltage magnitudes of the 30 by 30 resistors at the bottom of the MS using CST ® Simulation of ACR Class 3- Heterogeneously Dense Phantom 3 Breast ID: 062204. 4.14a healthy. 4.14b unhealthy with 7 mm radius PEC tumor at bottom right. 4.14c Representation of the algebraic difference between the voltages magnitudes of the healthy 4.14a and unhealthy 4.14b . . . 74

4.15 Plane representations of the voltage magnitudes of the 30 by 30 resistors at the bottom of the MS using CST ® Simulation of ACR Class 3- Heterogeneously Dense Phantom 3 Breast ID: 062204. 4.15a healthy. 4.15b unhealthy with 7 mm radius PEC tumor at bottom left. 4.15c Representation of the algebraic difference between the voltages magnitudes of the healthy 4.15a and unhealthy 4.15b . . . 75

4.16 Plane representations of the voltage magnitudes of the 30 by 30 resistors at the bottom of the MS using CST ® Simulation of ACR Class 3- Heterogeneously Dense Phantom 3 Breast ID: 062204. 4.16a healthy. 4.16b unhealthy with 5 mm radius PEC tumor at center right. 4.16c Representation of the algebraic difference between the voltages magnitudes of the healthy 4.16a and unhealthy 4.16b . . . 75

4.17 Plane representations of the voltage magnitudes of the 30 by 30 resistors at the bottom of the MS using CST ® Simulation of ACR Class 3- Heterogeneously Dense Phantom 3 Breast ID: 062204. 4.17a healthy. 4.17b unhealthy with 5 mm radius PEC tumor at center left. 4.17c Representation of the algebraic difference between the voltages magnitudes of the healthy 4.17a and unhealthy 4.17b . . . 76

4.18 Plane representations of the voltage magnitudes of the 30 by 30 resistors at the bottom of the MS using CST ® Simulation of ACR Class 3- Heterogeneously Dense Phantom 3 Breast ID: 062204. 4.18a healthy. 4.18b unhealthy with 5 mm radius PEC tumor at center right. 4.18c Representation of the algebraic difference between the voltages magnitudes of the healthy 4.18a and unhealthy 4.18b . . . 76

4.19 Plane representations of the voltage magnitudes of the 30 by 30 resistors at the bottom of the MS using CST ® Simulation of ACR Class 3- Heterogeneously Dense Phantom 3 Breast ID: 062204. 4.19a healthy. 4.19b unhealthy with 5 mm radius PEC tumor at center right. 4.19c Representation of the algebraic difference between the voltages magnitudes of the healthy 4.19a and unhealthy 4.19b 77

4.20 Plane representations of the voltage magnitudes of the 30 by 30 resistors at the bottom of the MS using CST ® Simulation of ACR Class 3- Heterogeneously Dense Phantom 3 Breast ID: 062204. 4.20a healthy. 4.20b unhealthy with 3 mm radius PEC tumor at center right. 4.20c Representation of the algebraic difference between the voltages magnitudes of the healthy 4.20a and unhealthy 4.20b 77

4.21 Plane representations of the voltage magnitudes of the 30 by 30 resistors at the bottom of the MS using CST ® Simulation of ACR Class 3- Heterogeneously Dense Phantom 3 Breast ID: 062204. 4.21a healthy. 4.21b unhealthy with 3 mm radius PEC tumor at center left. 4.21c Representation of the algebraic difference between the voltages magnitudes of the healthy 4.21a and unhealthy 4.21b . . . 78

4.22 Plane representations of the voltage magnitudes of the 30 by 30 resistors at the bottom of the MS using CST ® Simulation of ACR Class 3- Heterogeneously Dense Phantom 3 Breast ID: 062204. 4.22a healthy. 4.22b unhealthy with 3 mm radius PEC tumor at bottom right. 4.22c Representation of the algebraic difference between the voltages magnitudes of the healthy 4.22a and unhealthy 4.22b 78

4.23 Plane representations of the voltage magnitudes of the 30 by 30 resistors at the bottom of the MS using CST ® Simulation of ACR Class 3- Heterogeneously Dense Phantom 3 Breast ID: 062204. 4.23a healthy. 4.23b unhealthy with 3 mm radius PEC tumor at bottom right. 4.23c Representation of the algebraic difference between the voltages magnitudes of the healthy 4.23a and unhealthy 4.23b 79

4.24 illustration of the CNN indicating Convoluiton layers (CL), Pooling layers (PL), filters, and Fully connected layers (FCL) 81

4.25 Fabricated Metasurface (MS). 4.25a MS top layer and 3D view of the 30×30 UC ELC 3 mm size. 4.25b MS bottom holding 30×30 resistors for amplitude voltage measurements 83

4.26 Experimental: setup including. 84

4.27 Experiment result using the fabricated MS of 30 by 30 UC ELC. 4.27a Original image without PEC sphere. 4.27b Image with a PEC sphere of 10 mm diameter inside. 4.27c Image with the algebraic difference between the voltage magnitudes of images 4.27a and 4.27b 85

5.1 Block diagram of the proposed system integrating three major components: . . 88

5.2 Concept of detection using reflection coefficient 90

5.3 Reflection coefficients S_{11} of the simulated designs, and fabricated MW probe. . 92

5.4 Top and bottom layer of the probe design. 5.4a Top layer optimization 1. 5.4b Bottom layer optimization 1. 5.4c Top layer optimization 2. 5.4d Bottom layer optimization 2. 93

5.5 Top and bottom layer of the probe design. 5.5a Top layer optimization 1. 5.5b Bottom layer optimization 1. 5.5c Top layer optimization 2. 5.5d Bottom layer optimization 2. 94

5.6 Design and fabricated - top and bottom layer antenna. 5.6a Fabricated antenna - FR-4 material - top layer view. 5.6b Fabricated antenna - FR-4 material - bottom layer view. 95

5.7 Representation of von Neuman and Moore neigh- borhoods. 5.7a von Neuman space. 5.7b Moore space. 97

5.8 Game of Life rules: 99

5.9 Eight of the 30 Simulated Phantoms in CST ® - XZ cutting plane and 3D view . 102

5.10 Simulated realistic phantom in CST ® X-Z cut 103

5.11 Eight S_{11} measurements taken from four different phantoms (with and without tumor) using the designed antenna CST ® 104

5.12 Training data sample S_{11} for seeding the self-organizing algorithm was measured from the designed antenna using CST ® during numerical simulation, mimicking healthy and tumor breast tissue with a tumor diameter of 10 mm. . . 105

5.13 Experiment Setup. 5.13a Antenna experiment setup NanoVNA H4 and antenna - top view. 5.13b Antenna experiment setup NanoVNA H4 and antenna and phantom - top view. 5.13c Antenna experiment setup NanoVNA H4 and antenna and phantom - side view 107

5.14 Eight S_{11} measurements taken from four different phantoms (with and without tumor) using the designed antenna and Nano VNA H4 108

5.15 Training data sample S_{11} for seeding the self-organizing algorithm was measured from the designed antenna using the Nano VNA during experimental validation, mimicking healthy and tumor breast tissue with a tumor diameter of 10 mm. 110

List of Tables

1.1 Some breast cancer studies in the literature 6
1.2 Cole-Cole model parameters for normal and tumorous tissue 9
1.3 Color distribution for Anatomically Realistic Breast Phantoms (ARBP) in Figures 1.5, 1.6, 1.7, and 1.8 11

3.1 List of parameters of the designed ELC according Figures 3.3a, 3.3b, and 3.3c . . 41
3.2 CNN Results of the experimental validation 58

4.1 Results of the CNN 82

5.1 The rule n4_v1_nonstable 98
5.2 The basic Genetic Algorithm (GA) 100
5.3 Classifier performance on data from the tumor detection system phantom-antenna 106
5.4 Classifier performance on data from the tumor detection system phantom-antenna 111

List of Abbreviations

ϵ permittivity 5, 17, 18, 63

ϵ_r relative permittivity xi, xv, 8–10, 37, 44, 54, 63, 66, 68, 82, 91

μ permeability 5, 17, 18, 63

μ_r relative permeability xv, 66, 68, 91

σ conductivity 14

MATLAB ® MATrix LABoratory® R2022a 10, 13, 24, 25, 34, 45, 101

2D Two dimension xv, 4–7, 10, 18, 22, 36, 37, 54, 58, 61, 71, 80, 87, 89, 97, 98, 100, 109

3D Three dimension xi, xii, xv, xvii, xviii, 4, 5, 10, 12, 13, 18, 22–25, 29–33, 40, 64, 70, 72, 83, 101, 102, 112

3D Slicer 3D Slicer image computing platform xii, 13, 24, 25, 35, 101

Accuracy It provides the efficiency of the test or states the number of individuals correctly classified by the test 7, 58, 60, 81, 86, 106

ACR American College of Radiology xii, xiii, xv–xvii, 10, 24, 25, 27–34, 45, 73–79

AI Artificial Intelligence 20, 36, 59, 80, 86, 89

AL Artificial Life 87, 96, 111

ARBP Anatomically Realistic Breast Phantoms xi–xv, xx, 10–14, 22, 24–34, 36, 45, 47–49, 61, 70–73, 80, 81, 86, 108

BC Breast Cancer 1, 2, 5, 7, 18, 19, 36, 59, 61, 70, 72, 80, 86, 87, 95, 96, 101

CA Celular automata 87–89, 96–98, 100, 103, 105, 106, 109, 111

CC view Craniocaudal CC view is one of the two standard projections for screening mammography 26

CL Convoluiton layers xi, xvii, 7, 81

CNN convolution neural network xi, xiv, xv, xvii, xx, 6, 7, 58–60, 80–82

Cole-Cole model Variation of the Debye mode, representing the dispersion of the material as a function of the frequency interpolating permittivity and conductivity xi, xx, 8, 9

CST ® Computer Simulation Technology Studio Suite® 2020 xi, xiii–xviii, 10, 13, 14, 40, 45, 47–49, 63, 64, 70, 72–79, 101–105

CSV Comma-separated values (CSV) is a format based on text that separates values with commas, and each row is separated by newlines 54

DAS Delay and Sum Alogarithm 6

DICOM Digital Imaging and Communications in Medicine 13, 22, 61, 70

DT Decision Tree 95, 96, 105, 109

Edema Swelling caused by abnormal accumulation of fluid in tissues 8

effective conductivity σ represents electrical properties in the tissue, which can vary as the direction changes, it can be take complex expression, and also is frequency dependent 10

ELC Electric-Inductive-Capacitive xiii, xv, xvii, xviii, xx, 40–45, 52, 61, 63–71, 82–85

EM Electromagnetic xi, 3–5, 10, 13, 14, 16, 18–22, 28, 35–40, 43–45, 50, 52, 59, 61, 63, 64, 69, 70, 80, 81, 86–90, 101

FCL Fully connected layers xi, xvii, 7, 81

FEA Finite Element Analysis 86

FEBio Finite Elements for Biomechanics 24–26, 28

FR-4 FR-4 indicates flame retardant material for a glass-reinforced epoxy resin laminate xiii, xviii, 40, 41, 43, 44, 52, 63, 64, 91, 95, 111

GA Genetic Algorithm xx, 87–89, 96, 100, 105, 106, 109

Globocan Global Cancer Observatory 1

HOG Histograms of Oriented Gradients xiii, xiv, 46–49

IDC Interdigital Ccapacitor 91

IR Infrared 7

Lymphedema Blockage in or damage to the lymphatic systems, causing lymphatic fluid to build up in tissues, making them swell 1

MeshLab The open source system for processing and editing 3D triangular meshes 24, 25

Meshmixer Meshmixer is a state-of-the-art software for working with triangle meshes. Autodesk, Inc. 35

MI Microwave Imaging 62

MIST Microwave Imaging Via Space-Time 4, 5

ML Machine Learning 6, 7, 61, 89

MLO view Mediolateral oblique MLO view is one of the two standard mammography views 26

MM Metamaterial 18

MMs Metamaterials 17, 18

MRI Magnetic Resonance Imaging xi, 1–3, 10, 25, 70, 86

MS Metasurface xiv–xviii, 18, 20, 36, 37, 40, 43, 51, 56, 61, 63, 66, 69–79, 82–86

MSs Metasurfaces 18

MW Microwave xi, xiii–xv, xviii, 2–5, 7, 16, 19, 21, 36–40, 47–54, 56, 57, 59, 61–64, 66, 67, 69, 70, 82, 84, 86–88, 92, 96, 105, 106, 108, 109, 111

MWD Microwave Detection 19

MWI Microwave Image 3–6, 19

MWR Microwave radar-based 4, 5

MWT Microwave tomography 4, 5

Neo-Hookean The neo-Hookean model can predict non-linear stress-strain behaviour deformations for materials; it was proposed by Ronald Rivlin in 1948 27

Neoangiogenesis is the mechanism in cancer that permits the creation of new blood vessels to supply cancerous tumours and ensure their growth 8

NPV Negative predictive value is the probability of the absence of disease in apatient given a negative test 106

NRRD Nearly Raw Raster Data file capable to store and visualize n-dimensional raster data. It was developed to support scientific visualization 24, 25

OUT Object Under Test xiii, 3–5, 37, 38, 63, 82, 83, 86, 87

Overdiagnosis Detection and treatment of breast cancers that could remained asymptomatic during the lifetime 3

PCB Printed Circuit Board 40, 52, 64, 91

PEC Perfect Electric Conductor xv–xviii, 54, 60, 71, 73–79, 83–85, 101, 108, 109, 111

PL Pooling layers xi, xvii, 7, 81

PPV Positive predictive value is the probability of disease in a patient given a positive test 3

Prognosis The medical prediction of recovering from a disease can be adjusted according to age, sex, treatment, and other factors 3, 18

Quiescent A quiescent state remains in the same state as its neighbours, which have the same quiescent status. In Cellular Automata, this state is represented by “0” or “blank”. It can also be associated with “vacuum”. 100, 103

RELU Rectified Linear Unit 58, 80

RGB Red, Green, and Blue 7, 54, 80

ROI Regions of Interest 46

Sensitivity The inherent ability of a test to detect correctly a condition when it is present 3, 106

shear modulus The shear modulus quantifies the elastic shear stiffness of a material and is defined as the ratio of shear stress to shear strain. 27

SMD surface-mount device 61

Specificity The inherent ability of a test to rule it out correctly when it is absent 3, 106

STL stereolithography xii, 24, 25

SVM Support Vector Machine 95, 96, 105, 106, 109

T1 T1 (longitudinal relaxation time) is the time constant which determines the rate at which excited protons return to equilibrium 22

TetGen It is a program to generate tetrahedral meshes of any 3D polyhedral xii, xiii, 26–29, 31, 33, 34

TRITON X-100 polyethylene glycol mono phenyl ether xiv, 51, 53–56, 89

TSAR Tissue Sensing Adaptive Radar 4, 5

UC unit cell xiii, xv, xvii, xviii, 18, 39, 40, 42, 63–66, 69, 71, 82–85

UofC University of Calgary 10

UW University of Wisconsin 10, 70

UWB Ultra-wideband 4, 5

VNA Vector Network Analyzer xviii, xix, 106–111

Voxel In 3D computer graphics, a voxel represents a value on a regular grid in three-dimensional space 10, 22

Chapter 1

Introduction

1.1 Overview

Cancer has become one of the greatest concerns in public health and is present throughout the world. In 2022, Global Cancer Observatory (Globocan) reported (9,976,499) new cancer cases, with Breast Cancer (BC) accounting for the highest incident with (11.4%). It is also reported that of the (9,743,832) deaths, BC is the first among women, and the fourth cause of mortality in general (6.8%), after lung (18. 7%), colorectum (9.3%), and liver (7.8%) [1].

In Canada, there were 28,026 cases of BC, which accounted for 10.1% of the total cancer cases (274,364) in 2020 [1]. According to the Canadian Cancer Society, the leading cause of cancer among women is BC, which is also reported in [2]. In general, BC ranks second in mortality with (5,500) deaths in 2020, over more than (40,000) deaths for all cancers, and the percentage of survival at 5 years is (89%) [3].

BC affects women negatively in the long term; among cancer patients, psychological side effects such as depression, physical negative effects, and financial stress have been reported [4, 5]. Among the long-term physical adverse effects reported are shoulder morbidity, arm Lymphedema, and reduction in shoulder mobility, without mention of the pain involved [6].

Since early detection is a crucial factor in the treatment of cancer, particularly BC, several techniques have been developed to detect tumors in their incipient stages. Although mammography is the standard for early detection, it has shown certain problems in detecting dense breasts, not to mention how invasive this technique can be for women [7]. Three techniques are widely recognized in the field of early detection of BC: ultrasound, Magnetic Resonance Imaging (MRI), and X-ray mammography. The following Figure 1.1 shows the advantages and disadvantages of these techniques.

The detection of BC is essential for successful therapy, suggesting the importance of applying a highly efficient diagnostic test. However, many cases arise where early detection programs encounter various obstacles during their operational implementation, including social and economic constraints or geographical considerations that complicate the accessibility of effective, affordable screening programs. In particular, in low- and middle-income countries, a large number of women are diagnosed with advanced BC stages [8].

The Microwave (MW) technique has been extensively researched for its application in medical screening, especially for BC; however, despite its advantages over established techniques, it is still not currently a screening option. There is a need to promote a close relationship between MW developers and end users to improve the relative position of MW technology. By improving communication and understanding between these two groups, MW techniques can gain recognition and expand their natural benefits and capabilities in medical imaging and detection [9]. Another burden for MW is their competition with techniques widely accepted by the clinical community, such as mammography, MRI, or ultrasound [10], which is difficult to overcome. MW also have challenges in their application that can be engineering-channeled by talented researchers; some of these challenges are high reflection from the surface [11, 12, 13], resolution limitations [14, 15, 16, 17, 18], reconstruction limitation [19, 20, 21], coupling and noise limitations [22, 23], these relative disadvantages can drive new research and innovative solutions. However, MW modalities offer a promising alternative because they are an affordable, non-ionizing, and mature approach [24], thus addressing many of the shortcomings of traditional imaging methods.

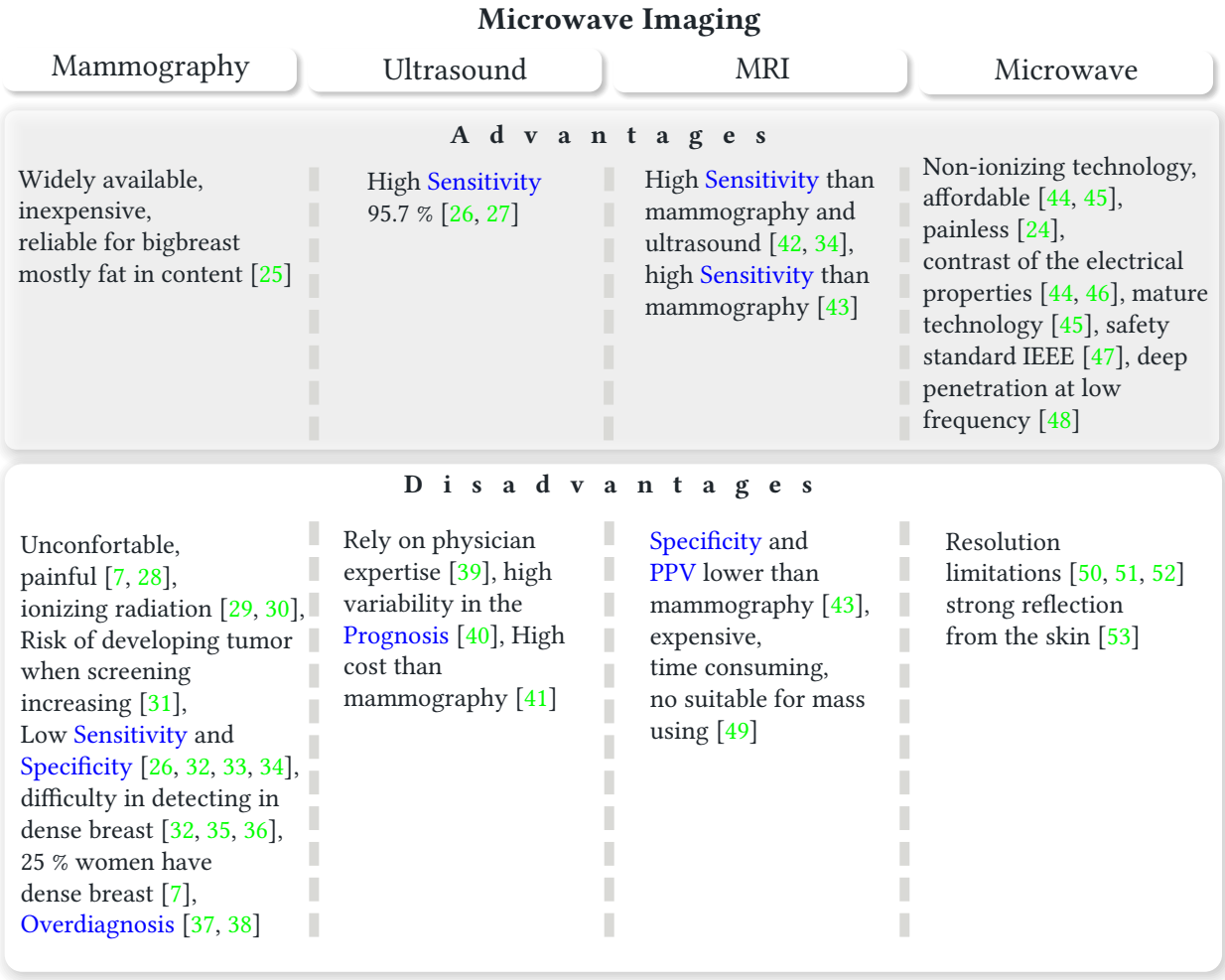


Figure 1.1: Comparison between X-ray mammography, MRI, Ultrasound, and MW

1.2 Microwave Imaging

The Microwave Image (MWI) method could address numerous limitations associated with traditional approaches and could significantly transform breast cancer detection [54]. MWI consists of examining an object's internal electrical properties by collecting Electromagnetic (EM) signals (information) in a simulated or experimental setting within the microwave frequency spectrum [55]. When a MW transmitter emits waves toward Object Under Test (OUT), some of the EM waves pass through OUT, while others are reflected from its surface, and the material

absorbs a portion as well. The combination of transmitted, reflected, and absorbed signals forms a distinctive representation of the electrical characteristics of the materials within the OUT.

When we alter the material composition of an OUT, the energy of the EM signals that are transmitted, reflected, and absorbed also changes. This change reflects the new electrical properties of the material. Researchers have developed two related techniques: 1. the reflection and transmission technique, known as Microwave tomography (MWT), and 2. the reflection method, referred to as Microwave radar-based (MWR) [7]. A schematic diagram illustrates the MWI techniques in Figure 1.2.

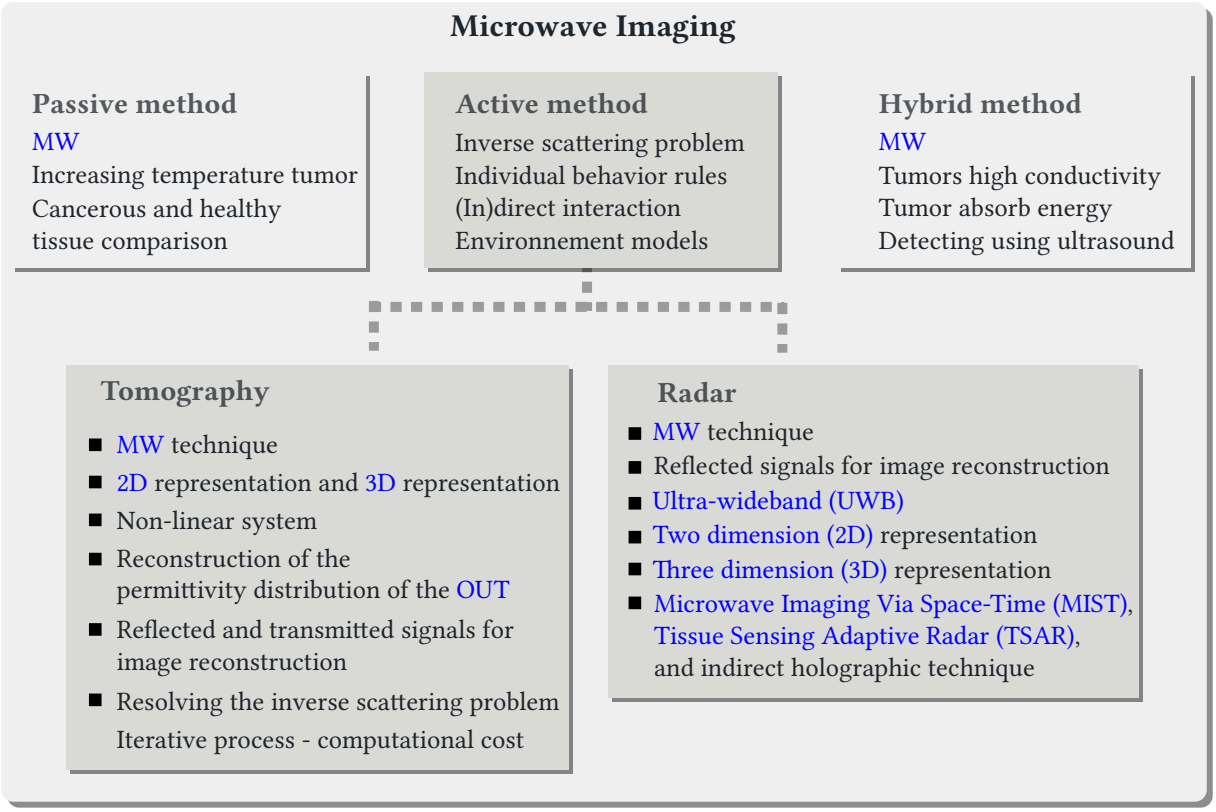


Figure 1.2: The MW techniques, passive, hybrid and active approaches

1.2.1 Microwave imaging tomography

MWT was developed in the late 1970s, and its biomedical applications emerged in the 1980s. This technique utilizes EM waves to analyze the components of an object. Various approaches exist within this concept, including single-frequency and multifrequency methods, as well as

techniques in the time domain [56]. The method requires multiple antennas to scan the OUT, which is often coupled to the antennas using a saline solution. The signals acquired during this process are processed to represent the electrical properties of OUT, specifically in terms of complex permittivity (ϵ) and magnetic permeability (μ) [57].

The first documented application of MWI for breast tumor detection comes from Dartmouth College, which developed a 2D imaging system. This system operated between 300 and 1000 MHz and used 16 monopole transmitting and receiving antennas (Tx / Rx) [58].

Another MWT system, presented by Son et al., also aimed at the detection of BC. This system featured a circular configuration of monopole antennas and operated within a frequency range of 500 MHz to 3 GHZ. It is considered a preclinical prototype designed to vertically scan the breast with 16 Tx / Rx antennas. To improve performance, a matching saline liquid was placed between the antennas and the breast [59]. In 2016, researchers tested a prototype MWI in 15 volunteers at Seoul National University Hospital. This system used the Fast Forward Solver and was designed to operate in the frequency range of 3 to 6 GHz [60].

1.2.2 Microwave imaging radar-based

The process of using reflected EM waves to explore an object and create an image is called MWR. The MW device emits waves that illuminate the OUT and capture the reflected EM signals for image reconstruction. The first clinical trial that used a MWR technique was reported by Klemm et al. in 2008 at the University of Bristol. The researchers implemented a multistatic radar array UWB in a matching medium to perfectly couple the hemispherical 16-antenna array with the breast; the system detected tumors as small as 8 mm in size [61, 62]. An additional example is from a 3D system introduced in 2010. In this study, the researchers developed a multichannel architecture that includes 32 measurement channels capable of wideband operation up to 3 GHz. They also created an acquisition system to manage the measurements and connect the system to a computer. Two broadband power dividers supplied the MW energy. The 32 antennas were placed in a cylindrical array inside a tank filled with a mixture of glycerin and water [63].

The recent literature highlights important developments in this modality. For example, a study in 2004 examined MWI through MIST beam formation, which was tested using 3D phantoms connected to UWB antennas via a liquid medium. The antennas UWB were arranged to mechanically scan the breast phantom, and the collected data were processed using a data-adaptive algorithm; the system successfully detected tumors as small as 4 mm in size [64]. Another important work highlighted in the literature is TSAR, a system developed to test this technique on a small sample of eight volunteers. The system operated within a frequency range of 50 MHz to 15 GHz, utilizing laser estimation of breast volume to improve 3D image reconstruction [65]. In another approach, the indirect holographic technique, researchers used a

reference plane wave to analyze the complex near-field, simplifying the complexities involved in image reconstruction [66].

Several examples of MWI applications can be found in the literature, as presented in Table [1]. This table is divided into five categories: (1) Study, (2) Antenna Technology, (3) Frequency of Operation, (4) Size of Tumor Detection as reported by the study, (5) Scan Time, and (6) Image Reconstruction Technology.

Table 1.1: Some breast cancer studies in the literature

Study	Antenna	Frequency	Tumor size	Scan time	Imaging
Dartmouth College [67, 68]	16 monopole antennas	0.5-2.1 GHz	10.5 mm	15 min	Tomography
University of Calgary [65]	UWB antenna	0.05-15 GHz	10 mm	30 min	Delay and Sum Alogarithm (DAS)
McGill University [69]	WB antenna	2-4 GHz	–	5 min	DAS
University of Bristol [70]	60 UWB antennas	3-8 GHz	–	2 min	DAS
Shizuoka University [71]	30 UWB antennas	4-9 GHz	15 mm	3.3 min	DAS
SUSTech [72]	2 UWB horn antennas	4-8.5 GHz	–	4 min	DAS
Hiroshima University Hospital [73]	16 UWB antennas	3.1-10.6 GHz	5 mm	14 min	DAS

1.3 Machine Learning - Convolutional Neural Network

Various researchers have directed their focus towards Machine Learning (ML) particularly convolution neural network (CNN) in order to address a wide variety of problems in different areas, such as speech recognition [74, 75], industrial [76, 77, 78, 79], biomedical [80, 81, 82], and defense [83] to mention a few. ML encompasses a wide range of techniques, with CNN being particularly preferred for its ability to identify patterns across a broad spectrum of data sources. CNNs have a remarkable ability to process 2D images. The conventional arrangement consists

of Convoluiton layers (CL), Pooling layers (PL), and Fully connected layers (FCL), which can learn and enhance their processing efficiency during the training stage, thereby reducing the demand for computer resources [84]. An CNN with an input image of 30x30 pixels, two CL, followed by a PL, a FCL, and an output of four classes for classification is shown in Figure 1.3.

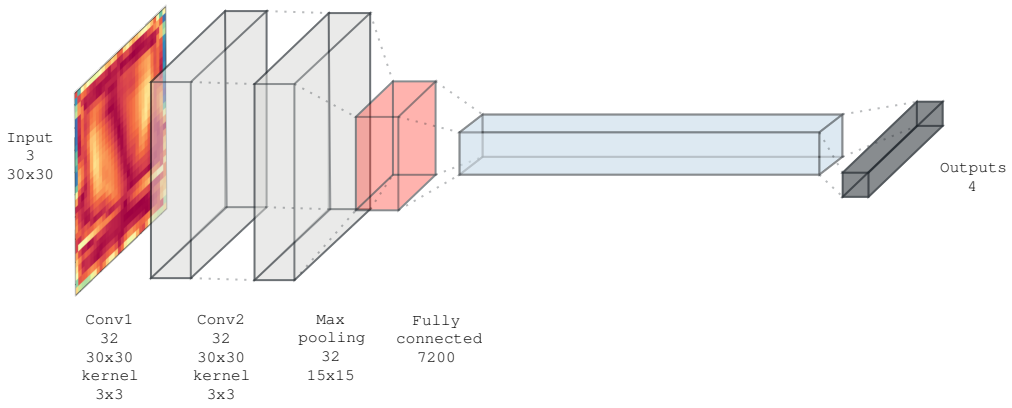


Figure 1.3: CNN visualization: input image 30x30 pixels, two Convoluiton layers (CL), one max-Pooling layers (PL), one Fully connected layers (FCL), and four outputs

2D arrays are frequently used to represent data in image processing. In this representation, each element of the array corresponds to the position of a pixel on the x- and y-axes. The images can be considered as separate 2D grayscale or color representations, usually consisting of three 2D arrays for Red, Green, and Blue (RGB).

In the biomedical field, CNN have contributed significantly to improving the identification and categorization of cancer [85]. The study in [86] introduces a method for detecting multiple types of cancer using a CNN architecture. In addition, the authors investigate the ability to identify the exact location of the tumor.

The use of ML in the area of MW for cancer detection has been very effective. The authors in [87] collected the reflection signals from the phantoms over a frequency range of 2 to 4 GHz. They used a system ML and CNN to detect, categorize, and measure tumor dimensions. Our research group has used machine learning techniques to effectively classify BC with a high level of Accuracy. The study carried out by [88] employed CNN to improve Accuracy cancer detection in images of healthy and tumorous breasts. The images were captured using a polycarbonate film that recorded the MW energy emitted by a horn antenna operating at a frequency of 700 MHz. An Infrared (IR) camera captured the image produced on the polycarbonate film after 10 seconds of exposure to MW radiation.

1.4 Realistic phantoms for electromagnetic simulations

Some major efforts have been made to provide information about the dielectric properties of breast tissue. For example, in [48], the authors present the profile for breast tissue from 0.5 to 50 GHz. This work used real material from 53 patients who provided 222 samples. The analysis of the data shows that the dielectric relative permittivity (ϵ_r) between normal and tumor tissue reveals strong differences in the water content. The high contents of water in the tumors would be determined by the presence of Edema, a large fat content, and Neoangiogenesis. Because of the polarization phenomenon, it is clear that the differences in dielectric ϵ_r are a result of the different water contents of the tumor and normal breast tissue.

With regard to the classification of tumors as invasive or non-invasive, no significant differences in their dielectric properties were detected between them. It is useful to note that as the fat content in the tissue increases, the values of the dielectric properties decrease, and it is particularly interesting that at low frequencies, the real part of the complex dielectric properties shows a strong difference. This fact suggests that the ability to detect anomalies, such as the mentioned invasive and non-invasive tumors, lies in the difference between the mean values of the dielectric properties of tumors and normal tissue over a wide range of frequencies. This fact is illustrated in Figure 1.4 using the model parameters of Cole-Cole model in Table 1.2 for normal and tumor tissue presented in [48].

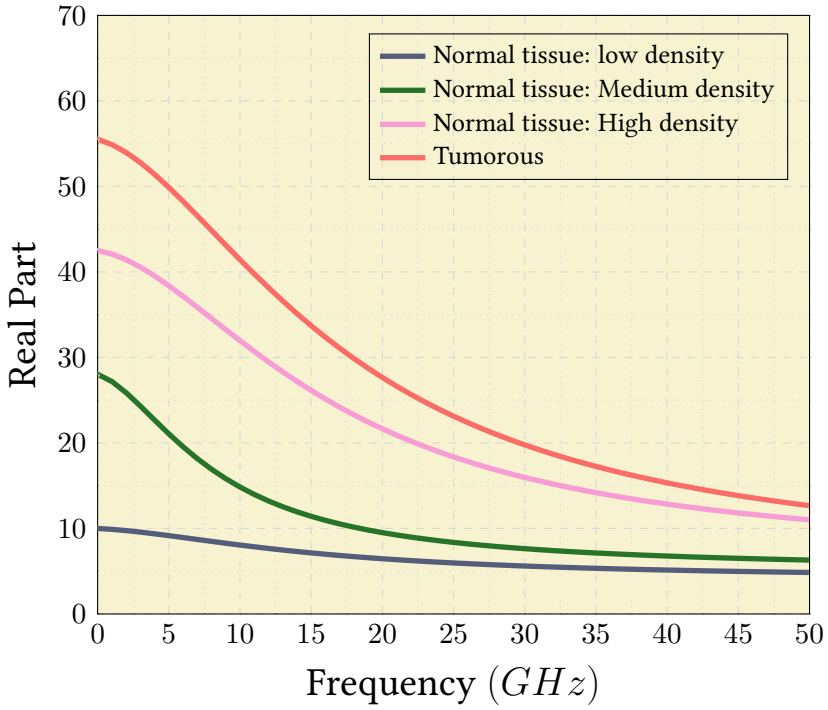


Figure 1.4: Real part of the relative permittivity (ϵ_r) between tumorous and normal tissue, using Cole-Cole model parameters presented in Table 1.2, data from 0.5 to 1 GHz

Table 1.2: Cole-Cole model parameters for normal and tumorous tissue

	Normal tissue			
	Low density	Medium density	High density	Tumorous
Δ_ϵ	6	23	36.5	50.5
ϵ_∞	4	5	6	5
$\tau(ps)$	10	19	9.4	9
α	0.09	0.08	0.06	0.07
$\sigma_s(S/m)$	0.1	0.5	0.7	0.9

Another study included a large sample size to achieve a profile of the dielectric properties of breast tissue from 0.5 to 20 GHz [89]. This work was based on 488 samples from reduction

surgeries and 319 samples from cancer surgeries in 196 patients in University of Wisconsin (UW) and University of Calgary (UofC). Similar work was performed in [90] on 354 samples, and after data analysis, the results showed a strong distance between the dielectric properties of breast tissues and cancerous samples. The frequency range for this study was the same as in [89], 0.5 to 20 GHz.

As in this work [91] is stated, the ϵ_r and effective conductivity σ of the matter have a predominant influence on the interaction with the electrical field; this interaction can be used to discriminate between healthy and tumorous tissues.

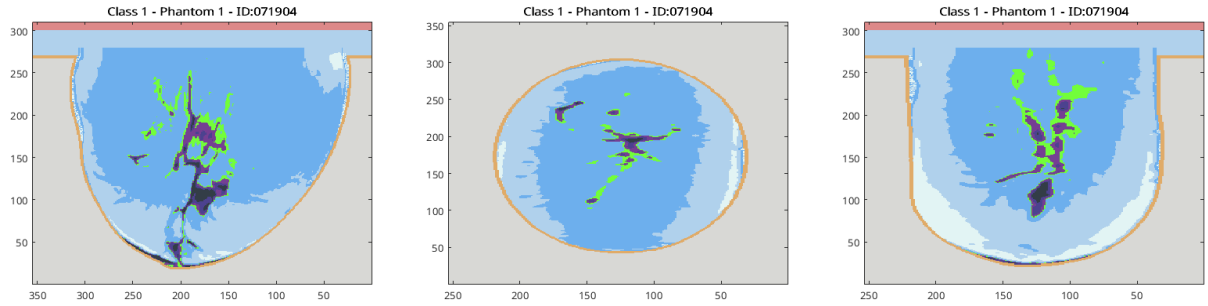
In testing the ongoing simulation in a realistic scenario, this work will use a Anatomically Realistic Breast Phantoms (ARBP). The Department of Electrical and Computer Engineering at UW provides a database of breast phantoms, particularly for EM simulations. These phantoms are anatomically realistic and resemble normal breast tissue, in addition to having the dispersive dielectric properties of normal breast tissue from 0.5 to 20 GHz [92]. The database consists of MRI scans of patients that are positioned horizontally. They provide nine (9) phantom databases, each of them in a 3D Voxel configuration; each Voxel is originally 0.5mm $\times$ 0.5mm $\times$ 0.5mm. In addition, the breast phantom has a skin layer of approximately 1.5mm, a subcutaneous layer of fat of approximately 15mm, and 5mm of chest muscle.

The ARBP database is made up of three (3) files in plain text format: 1. "***breastInfo.txt***", 2. "***mtype.txt***", and 3. "***pval.txt***". The first file, "breastInfo.txt", provides basic information about the structure 3D Voxel, such as identification, variable volume dimensions (s1, s2, s3) and classification. Breast density is classified according to the American College of Radiology (ACR) as follows: breast almost entirely fat with fibrous and glandular tissue (25%) Figures (1.5 and 1.6), breast scattered fibroglandular fibrous and glandular between 25% and 50%, breast heterogeneously dense, fibrous and glandular between 51% and 75% of the breast, and breast extremely dense Figures (1.7 and 1.8), fibrous and glandular over 75% of the breast [93].

With the help of MATrix LABoratory® R2022a (MATLAB ®) [94] and Computer Simulation Technology Studio Suite® 2020 (CST ®) [95], the files ***breathInfo.txt***, ***mtype.txt***, and ***pval.txt*** were programmed according to [96] to generate computationally realistic phantoms. Two of the nine ARBP are presented as an example; the images were realized in 2D in MATLAB ® and 3D using CST ®. The following Table 1.3 illustrates the distribution of colors for each tissue on the ARBP, for Figures (1.5,1.6, 1.7, and 1.8).

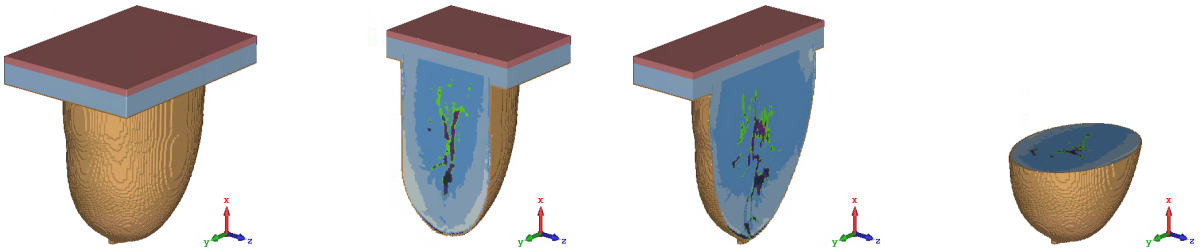
Table 1.3: Color distribution for Anatomically Realistic Breast Phantoms (ARBP) in Figures 1.5, 1.6, 1.7, and 1.8

Tissue type	Media color
Muscle	
Skin	
Immersion medium	
Fibroconnective/glandular-1	
Fibroconnective/glandular-2	
Fibroconnective/glandular-2	
Transitional	
Fatty-1	
Fatty-2	
Fatty-3	



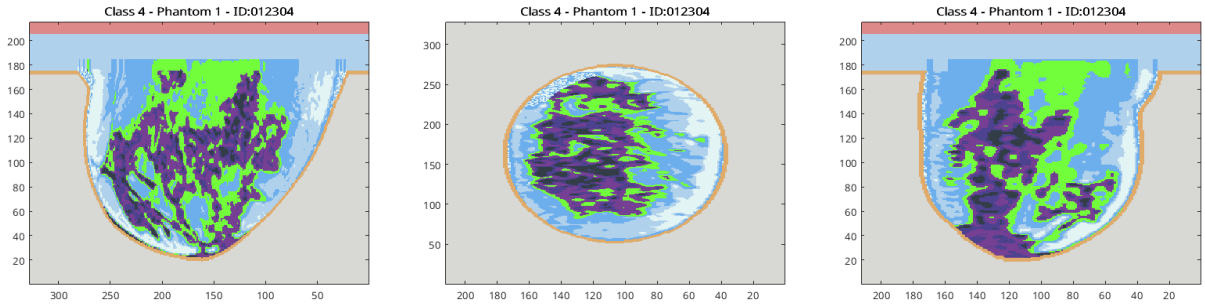
(a) (b) (c)

Figure 1.5: ARBP Class 1 - Mostly Fatty Phantom 1 Breast ID: 071904. 1.5a XY Slice. 1.5b XZ Slice. 1.5c YZ Slice.



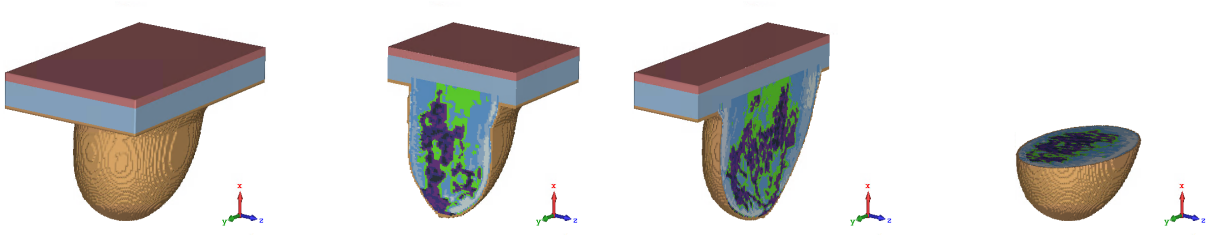
(a) (b) (c) (d)

Figure 1.6: ARBP Class 1 - Mostly Fatty Phantom 1 Breast ID: 071904 3D representation. 1.6a Entire 3D view. 1.6b XZ section view. 1.6c XY section view. 1.6d YZ section view.



(a) (b) (c)

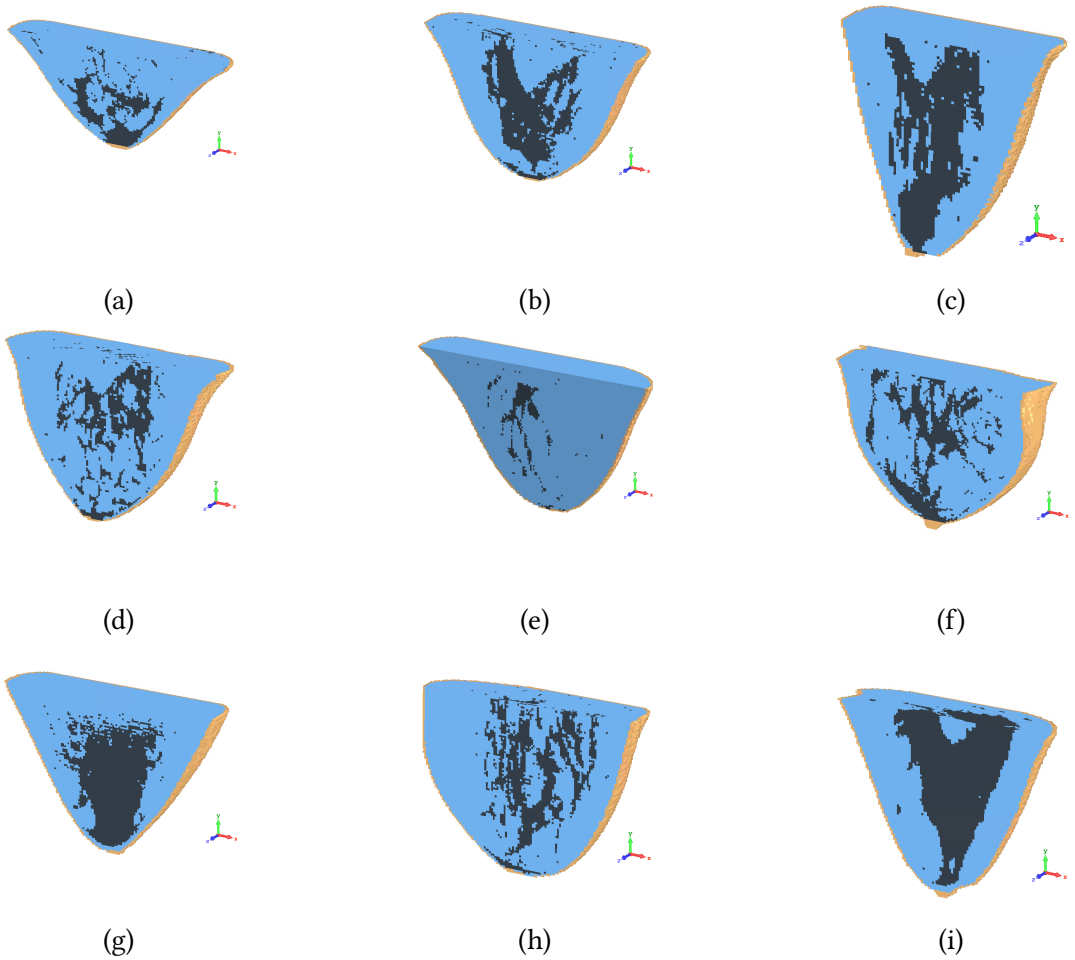
Figure 1.7: ARBP Class 4 Very Dense Phantom 1 Breast ID: 012304. 1.7a XY Slice. 1.7b XZ Slice. 1.7c YZ Slice.



(a) (b) (c) (d)

Figure 1.8: ARBP Class 4- Very Dense Phantom 1 Breast ID: 012304. 1.8a Entire 3D view. 1.8b XZ section view. 1.8c XY section view. 1.8d YZ section view.

Since this study will use EM software for simulation, it is expected that including an extensive realistic phantom dataset will contribute to achieving the projected goals. In this regard, the data set presented in [97] was considered to expand the phantom data set for this study. The authors of this data set generated 150 uncompressed phantoms, which were obtained from 3D images using computational algorithms. They reported an average of 2.1% difference in the magnitude of the glandular fraction by mass between the uncompressed and compressed phantoms; notably, the compressed phantoms showed an average of 12.1% and a maximum of 28.7% in fraction by mass and an average thickness of 61 mm. This data set is available in Digital Imaging and Communications in Medicine (DICOM) files, and the authors have classified each phantom using four materials: air, fat, glandular, and skin, with values 0, 1, 2, and 3, respectively. In this study, the entire uncompressed data set was processed using 3D Slicer image computing platform (3D Slicer), MATLAB ®, and CST ® to create realistic phantoms for microwave simulation purposes. Figure 1.9 shows 9 of these ARBP in a cutting plane on the z-axis.



(a) (b) (c)

(d) (e) (f)

(g) (h) (i)

Figure 1.9: Anatomically Realistic Breast Phantoms (ARBP) Dataset - 12.1 % and 28.7% average and minimum in fraction by mass respectively - Nine samples with z-axis cutting plane for EM simulation in CST ®: 1.9a, 1.9b, 1.9c, 1.9d, 1.9e, 1.9f, 1.9g, 1.9h, and 1.9i

1.5 Relevant theoretical framework

1.5.1 Wave propagation and Skin penetration in materials

Typically, an EM wave traveling through a medium with electrical conductivity (σ) $\neq 0$ experiences energy loss as a result of the properties of the dielectric material. Consider, for example, a medium that is linear, isotropic, homogeneous, and exhibits loss. The time-harmonic *Maxwell*

equations can be expressed as shown in Equations 1.1a, 1.1b, 1.1c, and 1.1d:

$$\nabla \cdot \mathbf{E} = 0 \tag{1.1a}$$
$$\nabla \cdot \mathbf{H} = 0 \tag{1.1b}$$
$$\nabla \times \mathbf{E} = -j\omega\mu\mathbf{H} \tag{1.1c}$$
$$\nabla \times \mathbf{H} = (\sigma + j\omega\epsilon)\,\mathbf{E} \tag{1.1d}$$

Manipulating Equations 1.1c and 1.1d, using the identity $\nabla \times (\nabla \times \mathbf{A}) = \nabla(\nabla \cdot \mathbf{A}) - \nabla^2\mathbf{A}$, and invoking Equations 1.1a and 1.1b, we obtained the wave Equations 1.2a and 1.2b:

$$\nabla^2\mathbf{E} - \gamma^2\mathbf{E} = 0 \tag{1.2a}$$
$$\nabla^2\mathbf{H} - \gamma^2\mathbf{H} = 0 \tag{1.2b}$$

Where

$$\gamma^2 = j\omega\mu\,(\sigma + j\omega\epsilon) \tag{1.3}$$

and γ is the propagation constant of the medium, and it is a *complex* number that can be wrote as

$$\gamma = \alpha + j\beta \tag{1.4}$$

The values for α and β in Equation 1.4 can be found using Equations 1.3 and 1.4 then solving Equations 1.5a and 1.5b:

$$\beta^2 - \alpha^2 = \omega^2\mu\epsilon \tag{1.5a}$$
$$\beta^2 + \alpha^2 = \omega\mu\sqrt{\sigma^2 + \omega^2\epsilon^2} \tag{1.5b}$$

Then

$$\alpha = \omega\sqrt{\frac{\mu\epsilon}{2}\left[\sqrt{1 + \left[\frac{\sigma}{\omega\epsilon}\right]^2} - 1\right]} \tag{1.6a}$$
$$\beta = \omega\sqrt{\frac{\mu\epsilon}{2}\left[\sqrt{1 + \left[\frac{\sigma}{\omega\epsilon}\right]^2} + 1\right]} \tag{1.6b}$$

The wave propagates in the positive direction of the $+\hat{z}$, and the electric field has just an x-component. The electrical and magnetic fields can be expressed in the following manner:

$$\mathbf{E}\,(z,t) = E_0 e^{-\alpha z}\cos\,(\omega t - \beta z)\hat{x} \tag{1.7a}$$
$$\mathbf{H}\,(z,t) = \frac{E_0}{|\eta|}e^{-\alpha z}\cos\,(\omega t - \beta z - \theta_\eta)\hat{y} \tag{1.7b}$$

Where $\eta = \frac{E_0}{H_0}$ and is known as *intrinsic impedance*, and it can be expressed as $\eta = \sqrt{\frac{j\omega\mu}{\sigma+j\omega\epsilon}} = |\eta| \angle\theta_\eta = |\eta| e^{j\theta_\eta}$

From Equations 1.7a and 1.7b, it is observed that the wave propagates in the z direction and its magnitude decreases exponentially with $e^{-\alpha z}$. The constant α represents the signal attenuation and can be quantified in decibels per meter (dB/m). An attenuation of e^{-1} corresponds to a reduction of $8.686dB$. Upon examination of Equation 1.6a, it is noted that if $\sigma = 0$ (in the context of free space and a lossless medium), then α equals zero. This implies that there is no reduction in the intensity of the wave signal during its propagation.

The MW penetration of the material is an important factor to consider in human body anomaly detection. As mentioned above, the EM wave decreases by e^{-1} as travel, this attenuation is known as the depth of the skin or the penetration depth. This attenuation can be expressed in terms of the magnitude of the signal wave Equation 1.8.

$$E_0 e^{-\alpha\delta} = E_0 e^{-1} \tag{1.8a}$$

$$\delta = \frac{1}{\alpha} \tag{1.8b}$$

Now replacing Equation 1.6a into Equation 1.8b it is obtained the penetration Equation 1.9.

$$\delta = \frac{1}{\omega\sqrt{\frac{\mu\epsilon}{2}\left[\sqrt{1+\left[\frac{\sigma}{\omega\epsilon}\right]^2}-1\right]}} \tag{1.9}$$

From 1.1d can be obtained the ***complex permittivity***

$$\nabla \times \mathbf{H} = (\sigma + j\omega\epsilon)\,\mathbf{H} = j\omega\epsilon\left[1 - \frac{j\sigma}{\omega\epsilon}\right] \tag{1.10a}$$

$$= j\omega\epsilon_c \mathbf{E} \tag{1.10b}$$

where $\epsilon_c = \epsilon\left[1 - j\frac{\sigma}{\omega\epsilon}\right] = \epsilon\left[1 - j\tan\theta\right]$, and this expression can be wrote as $\epsilon_c = \epsilon' - j\epsilon''$ The power penetration can be derived from the power density into the material [98] as fallowing Equation 1.11

$$\delta_p = \frac{c_0}{\omega\sqrt{2\epsilon'\left[\sqrt{1+\left(\frac{\epsilon''}{\epsilon'}\right)^2}-1\right]}} \tag{1.11}$$

The dielectric constant and dielectric loss factor formulas are proposed in [99], and are shown in the Equations 1.12a and 1.12b. These formulas are in function of Δ_∞ representing the difference between the dielectric constant at infinite and the static dielectric constant, τ_{ps} representing the

relaxation time that represents the random orientation of the dipole moment when the electric field is removed.

$$\epsilon' = \epsilon_\infty + \frac{\Delta_\infty}{1 + (\omega)^2 \tau_{ps}^2} \tag{1.12a}$$

$$\epsilon'' = \frac{\Delta_\infty \omega \tau_{ps}}{1 + \omega^2 \tau_{ps}^2} \tag{1.12b}$$

The dielectric property parameters presented in Table 1.2 were used to calculate the penetration depths for normal, medium, and high density tissues expressed in meters. These calculations are based on Equation 1.11 and are illustrated in Figure 1.10. Since this study uses low-frequency microwave techniques, Figure 1.10 indicates sufficient penetration for frequencies below 1 GHz.

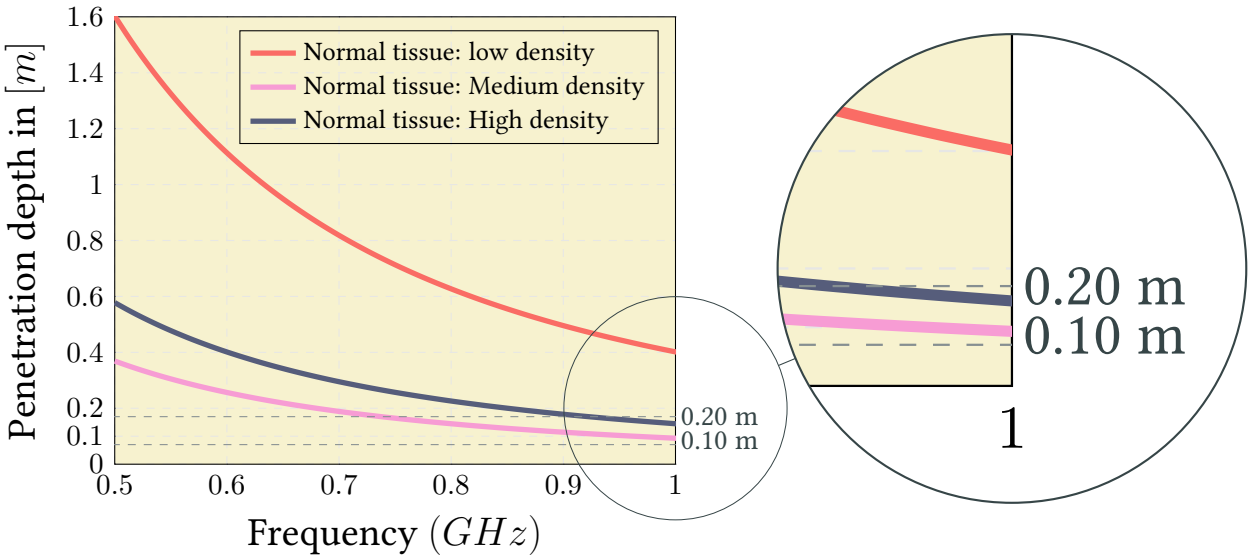


Figure 1.10: Penetration into normal breast tissue using parameters presented in Table 1.2, data from 0.5 to 1 GHz

1.5.2 Metasurface

The idea of Metamaterials (MMs) was first proposed at the end of the 1960s [100], in research about materials with negative ϵ and μ. In this medium, the electric field **E**, the magnetic field

H, and the propagation **k** are configured as orthogonal left-handed. A Metamaterial (MM) is a 3D structure that combines physical and chemical aspects and is available in periodic or non-periodic configurations. These properties of MMs provide considerable flexibility in the creation of materials not present in nature [101]. For example, researchers have manipulated the EM properties, making the absorption of incident electric and magnetic waves by the material possible and minimizing the reflective effect by matching with ϵ and μ and the free space [102, 103].

MSs are 2D surface structures composed of unit cell (UC) with a thickness smaller than the wavelength of the waves they manipulate and typically consist of a single layer. UC are the fundamental subwavelength structures of MS, designed using electrically small components that simulate electric and magnetic resonators. Metasurfaces (MSs), being 2D structures, are simpler to design and fabricate than MMs, which has led to increased interest from researchers in various applications. For example, in biomedical devices [104, 105], absorbers [106], wireless applications [107], and EM energy harvesting [108].

Another structure based on MS is an absorber, designed to capture EM energy by controlling the electrical properties of the material by tuning the UC geometry structures. Absorbers have gained attention in various applications, especially in defense, due to their affordability. When an EM wave travels from one homogeneous medium to another with a different refractive index, the incident wave is impacted, generating a reflected wave that propagates back and a transmitted wave that continues into the second medium. MSs can be designed to modify interactions by artificially changing the impedance to match the medium; some applications include, but are not limited to, anechoic chambers and solar cells. [109].

When an EM wave interacts with a MS, it induces surface currents on the small UC components, creating a circulating current with the metal ground. The interaction between this current and the electric field at the surface leads to EM resonance, resulting in energy absorption. In the absorber, the dielectric impedance can be matched to the impedance of UC at the resonant frequency. This impedance becomes equal in magnitude but opposite in phase, resulting in a purely real impedance. If the impedance of the free space matches the MS impedance in resonance, reflection decreases to a minimum, leading to maximum absorption by the MS structure.

1.6 Problem statement

Detecting BC in its early stages is crucial for successful treatment and Prognosis [110, 111]. Although mammography is the standard method for the early detection of BC, several studies

have raised concerns about its effectiveness. In particular, mammography has low effectiveness in identifying malignant tumors in dense breast tissue.

Mammography also has other drawbacks, such as pain experienced during the procedure, which can discourage many women from participating in regular screening programs. Furthermore, some women need to repeat the screening process and these results can lead to additional tests, contributing to significant mental stress [112]. This situation has inspired and attracted researchers to advance and implement novel screening methods that effectively address the limitations of current practices.

1.7 Research motivation

MW techniques have shown effectiveness in detecting malignant tumors; two modalities Microwave Detection (MWD) and MWI have captured the interest of many researchers. These methods show unique benefits compared to traditional techniques, making the microwave approach an effective option for many disciplines, especially in biomedicine. Within this framework, microwaves can be an important resource for the medical community to improve diagnostic tests for the identification of diseases.

Contrary to the disadvantages and limitations of traditional imaging techniques, the MW approach has shown to be affordable, nonionizing, and safe for women [24]. Furthermore, as the frequency increases, the propagation of EM waves within the material diminishes, so operating at lower frequencies will promote enhancements in imaging and overall testing performance. However, minimizing the electrical dimensions of a device at lower frequencies makes its design and fabrication more challenging.

1.8 Research Objectives

The primary objective of this research is to propose an alternative method for the detection of BC using microwave technology. Microwave techniques have demonstrated their effectiveness in identifying anomalies within the human body, as they can penetrate deeply at low frequencies. In addition, these techniques are safe, nonionizing, well-established, and relatively low-cost. The use of microwaves will help to achieve the main objective of this study while also developing specific goals.

1. Exploring concepts related to breast tissue and tumor materials for the detection of breast cancer.

2. Exploring the concepts of antennas and sensors that are metamaterial-based in the detection of breast cancer.

3. Developing compressed three-dimensional realistic breast phantoms for electromagnetic simulations using biomechanics software.

4. Improving accuracy of tumor anomaly classification using microwave technology as a detection method.

5. Introducing a breast cancer detection method that utilizes microwave technology based on a metasurface.

6. Introducing a microwave energy scanning system for cancer detection.

1.9 Thesis outline

This thesis is organized into five chapters, each focused on the research goals. The first chapter introduces the dissertation topic and summarizes the objectives of this research. The subsequent chapters are structured as follows:

The chapter 2 explores the compression of anatomically realistic phantoms. Its findings are related to the goal of the next chapter, where these compressed model phantoms are used for EM simulations.

The chapter 3 introduces the concept of using EM energy scanning for breast cancer detection and incorporating Artificial Intelligence (AI) into the detection process. The novel probe is inspired by the idea of a MS ensemble with electrically small elements. This study includes simulations using anatomically realistic phantoms and experimental validation of the proposed concept.

In chapter 4, we introduce a sensor designed to detect breast cancer that operates at submicrowave frequencies. This MS can create an image that represents the components of breast tissue. Our work includes numerical experiments conducted with realistic phantoms and experimental validation.

Chapter. 5 discusses breast cancer detection, introducing a microwave probe and a self-organizing algorithm. This study included a simulation phase that uses anatomically realistic phantoms and experimental validation.

Chapter 6 details the achievements of the thesis and provides recommendations for future enhancements.

Chapter 2

Simulation of the physical compression of a anatomically-realistic MRI-derived numerical breast phantom

2.1 Introduction

This section explores the simulation of the physical compression of a realistic breast model. The simulation results will provide important outcomes that correspond to the various research goals of this work. A flat realistic phantom can be used for additional EM simulations to evaluate new microwave devices. Using MW on authentic compressed breast models during an EM simulation phase will produce high-quality data for image generation. For example, compression improves image quality by reducing breast thickness [113, 114]. Compression also has shown a positive impact in reducing the time to exposure to a radiation source [115], improving image quality by decreasing the scatter effect, and reducing motion during the test [116].

To conduct this study, we will use anatomically realistic phantoms as discussed in the introduction chapter, sourced from [117, 96]. Specifically, we will use the Class 3 Heterogeneously Dense Breast Phantom 3 (ID: 062204) and the Class 4 Very Dense Breast Phantom 1 (ID: 012304). Both phantoms have dense breast tissue, which is relevant to our study, as such breast characteristics can complicate tumor detection. Additionally, we will simulate the compression of the Class 1 Mostly Fat Breast Phantom 1 (ID: 07109). The breast models that we used to simulate physical compression include 1. skin, 2. fat, and 3. fibroglandular tissue, allowing the phantoms to maintain their authentic anatomical structure.

2.2 Methods

Incorporating breast phantoms in the testing of microwave methods has positively impacted the assessment of innovative technologies, ideas, and devices to identify tumor tissues. Computational models have been instrumental in examining the physical conditions present during compression in mammography. Two methods have been documented for simulating breast phantoms: 1. mathematical representations that outline breast anatomy and 2. models developed through voxelization utilizing 2D or 3D medical imaging. However, there is still an apprehension about the realism of these models [118].

This research used realistic anatomical phantoms from MRI scans captured in the T1 phase. Due to their anatomically realistic features, we anticipate that the compression simulation will face difficulties reproducing the intricate geometries within finite element analysis software. The phantoms are built using cubic Voxel measuring 0.5 mm on each side. They feature a skin layer of approximately 1.5 mm thick, a 15 mm thick fat layer, and a 5 mm thick chest muscle layer. Realistic breast phantoms are designed to replicate the EM properties of breast tissue. To achieve this, they incorporate detailed specifications for the design of dielectric characteristics based on specific parameters [89, 90]. The materials needed for constructing these phantoms can be found in [117, 96, 92].

Since the breast model is based on medical imaging DICOM, its geometric model is highly complex and has several parts. The breast model consists of eight layers of tissue: 1. Skin, 2. Fibroglandular type 1, 3. Fibroglandular type 2, 4. Fibroglandular type 3, 5. Adipose type 1, 6. Adipose type 2, 7. Adipose type 3, 8. Intermediate. Figure 2.1 illustrates all the layers involved to simulate the compression of ARBP.

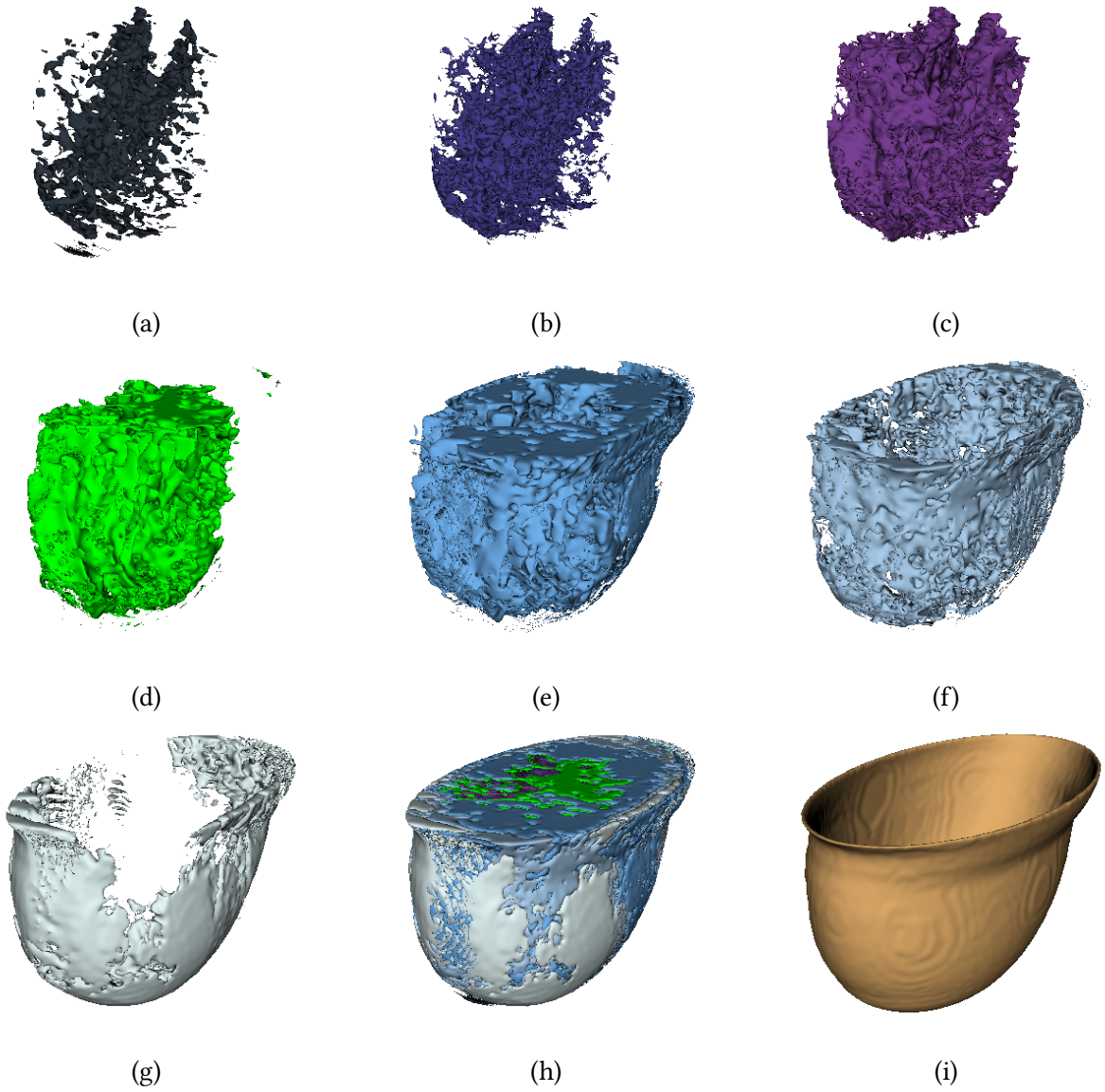
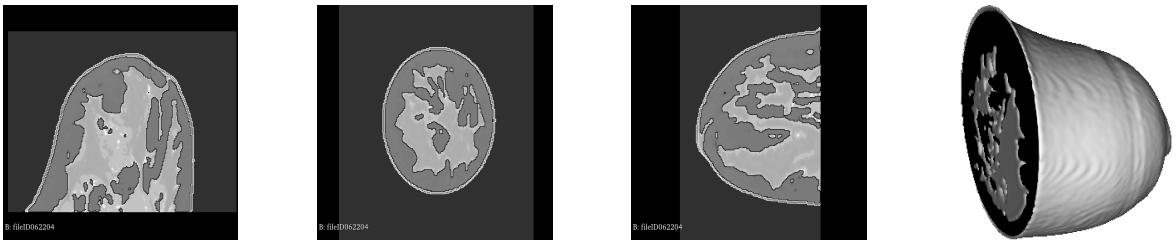


Figure 2.1: Example of the original layers tissues of the realistic breast phantom. 2.1a fibroglandular type 1, 2.1b fibroglandular type 2, 2.1c fibroglandular type 3, 2.1g transitional tissue, 2.1d fat type 1, 2.1e fat type 2, 2.1f fat type 3, 2.1h 3D view of the all fat, fibro, and transitional layers, and 2.1i skin tissue.

In order to allow the compression of this breast phantom model, we reduced its complexity through the following methods: 1. The three fatty layers were consolidated into one layer re-

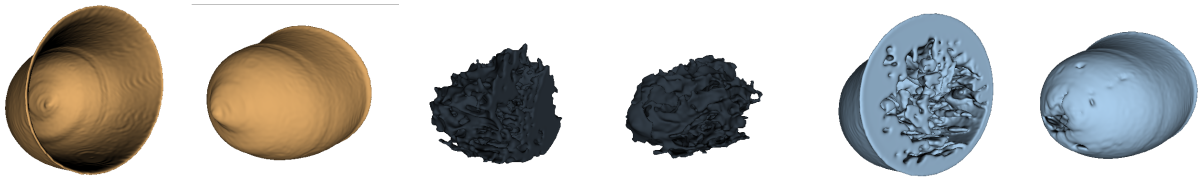
ferred to as“fat”, 2. while the three fibro-glandular layers, together with the transitional layer, were combined into a single layer called “fibro”

The compression process consists of several steps, each involving specific inputs and outputs. The main steps involved in this process are explained as follows: The three raw files, “breastInfo.txt”, “mtype.zip”, and “pval.zip”, which come with the original uncompressed model and also define the anatomy of the breast, are processed in MATLAB ® to eliminate the original immersion and muscle layers. The three fatty layers and the three fibro-glandular layers plus the transitional layers are merged into two distinct layers named “fat” and “fibro”, respectively. The skin, fat and fibro layers are ultimately combined into a single file NRRD. After processing the NRRD file using 3D Slicer [119], we generate three stereolithography (STL) files corresponding to “skin”, “fat”, and “fibro-glandular” tissues. Figure 2.2 illustrates the segmented image of this phantom, showing the axial, coronal, sagittal and 3D views produced in 3D Slicer. The next step involves refining the three STL models using MeshLab [120, 121]. The geometries depicted in Figures 2.3a, 2.3b, and 2.3c correspond to the skin, fibro glandular tissue, and fat, respectively. Once the three layers have been cleaned, we can proceed to create the finite element analysis model in the biomechanics software Finite Elements for Biomechanics (FEBio) [122]. The total summarized steps for the preparation of the phantoms to perform the simulation of the physical compression are illustrated in Figure 2.4.



(a) (b) (c) (d)

Figure 2.2: 3D Slicer view: Skin, Fatty, and Fibro Material views for Anatomically Realistic Breast Phantoms (ARBP) ACR Class 3- Heterogeneously Dense Phantom 3 Breast ID: 062204. 2.2a Axial view. 2.2b Coronal view. 2.2c Sagittal view. 2.2d 3D view.



(a) (b) (c)

Figure 2.3: Skin, Fatty, and Fibro STL files Material views for ARBP ACR Class 3- Heterogeneously Dense Phantom 3 Breast ID: 062204. 2.3a 3D Skin STL file. 2.3b 3D Fibro STL file. 2.3c 3D Fatty STL file.

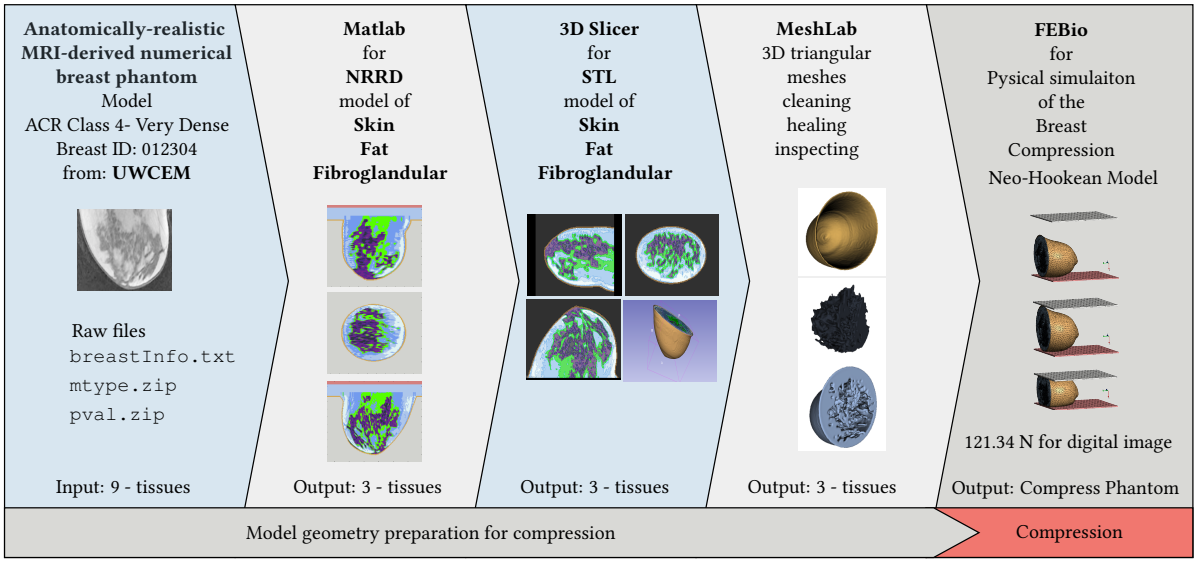
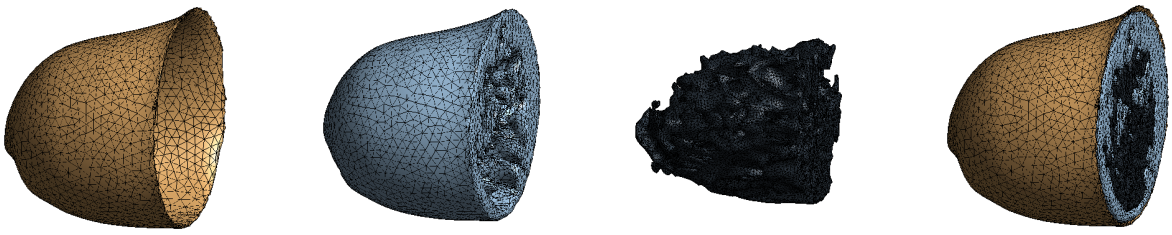


Figure 2.4: Process for prepare ARBP to simulate the physical compression of the breast phantoms. From the left to the right: (1) Original ARBP MRI derived, with raw files for construction in MATLAB ® software, (2) Raw files processed in MATLAB ® software generating the NRRD file with the three breast tissue layer: skin, fat, and fibroglandular, (3) NRRD file processed with 3D Slicer software, the output are three STL models for skin, fat, and fobroglandular breast tissues. (4) Enhencing STL models with MeshLab software, and (5) Compression process using FEBio software.

2.3 Simulation of the compression of the realistic breast phantom

The next part outlines the compression simulation of a ARBP conducted with the FEBio software. The initial phase of the simulation involves deducing the amount of force that should be applied to the breast model to achieve a compressed representation of ARBP. Despite efforts to optimize the force applied during mammography and enhance image quality, studies show considerable variation in the force used during screening. As a result, no specific level of force has been standardized for these tests. The recommendation in [123] states that compression should be minimal to achieve a quality image. A relatively large statistical study was conducted that involved 4,790 patient images. This research found that a force of 121.34 N creates a perfect image for the digital CC view [124], while a force of 134.23 N creates a perfect digital image for the MLO view. The mentioned values also align with the suggested range of 100 to 200 N, as indicated by [125]. The study referenced in [126] found that applying a force of 90 N resulted in an overall compression reduction of 2.97±1.26 mm while maintaining image quality. However, this compression also reported an increase 20% in the radiation dose. The researchers suggested that a 90 N force for compression is acceptable for women with sensitive breasts. Another study used information from 14 breast medical centers. The data set included 17,951 digital screened tests. The mean value force applied in these screenings was 116 N; meanwhile, the minimum and maximum values were 91 N and 147 N, respectively [127]. A study of more than 200 patients found an average compression force of 69 N for digital mammography imaging in fully automated screening [128], which is much lower than recommended [125]. A study collected data from three screening facilities, including more than 11,000 mammography images for analysis. The compression force applied in each facility varied significantly, with the following ranges for the minimum and maximum forces recorded at the three facilities: 47 N to 122 N, 42 N to 114 N and 103 N to 158 N [129].

Once we have defined the force among, we can import the STL files into the finite element analysis software environment FEBio. STL geometries are processed using TetGen [130], the only meshing method available in the software. In Figure 2.5, the created meshed geometries are displayed.



(a) (b) (c) (d)

Figure 2.5: Meshing in TetGen of Skin, Fatty, and Fibro Material views for ARBP ACR Class 3-Heterogeneously Dense Phantom 3 Breast ID: 062204. 2.5a TetGen mesh Skin geometry. 2.5b TetGen mesh Fatty geometry. 2.5c TetGen mesh Fibro geometry. 2.5d TetGen mesh Complete geometry.

In this study, the Neo-Hookean model is used for the simulation objectives. The model is detailed in Equation 2.1, which specifies the strain energy potential.

$$W = C_{10}\left(\bar{I}_1 - 3\right) + \frac{K}{2}\left(J - 1\right)^2 \tag{2.1}$$

where $C_{10} = u/2$ and u is defined as the initial shear modulus Equation 2.2a of the material, $\bar{I}_1$ is the first deviatoric strain invariant, K is the bulk moduli of the material Equation 2.2b, and J the Jacobian is the determinant of the elastic deformation gradient.

$$u = \frac{Ey}{2\left(1 + v\right)}, \tag{2.2a}$$

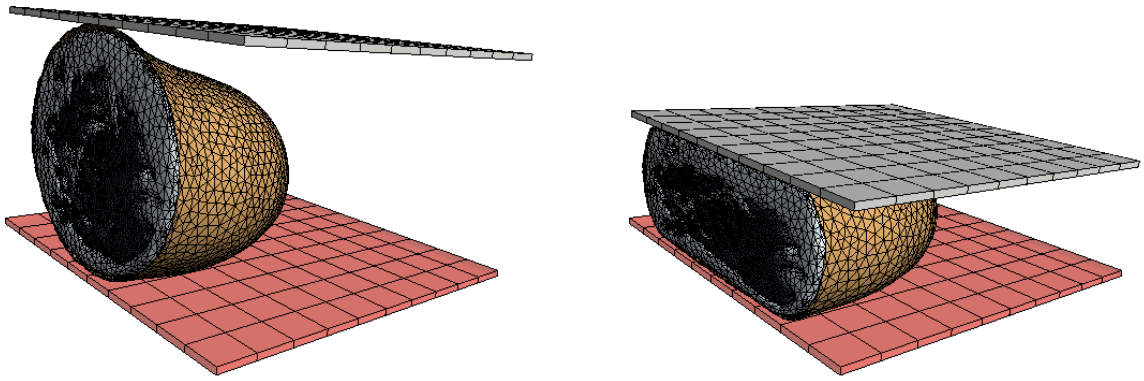
$$K = \frac{Ey}{3\left(1 - 2v\right)}, \tag{2.2b}$$

Where E_y is the Young's modulus and v is Poisson's ratio. Since the material is considered incompressible, which means that under force exposition, it conserves its volume, the Jacobian takes a value of 1. On the other hand, a material that changes its volume under load is called compressible. Regarding material expansion, it is considered perpendicular to the compress direction and is defined as the Poisson ratio or the coefficient of expansion; this coefficient has a range of $]-1, 0.5]$ for linear elastic material.

The study in [131] determined that a Neo-Hookean material model in its simple form is capable of describing the behavior of the fat and gland; the values of the parameter C_{10} were estimated at $3kPa$ and $12kPa$ for the fat and gland, respectively. The same estimated model

parameters are used in other work [132], where skin segmentation is studied and validated. In the case of Young's modulus for breast skin, an in vivo study [133] determined a value of $(344 \pm 88)\, kPa$. Meanwhile, all geometric components were modeled as quasi-incompressible material, setting the Poisson ratio at 0.49 [134].

The compression in its initial and final states is illustrated in Figure 2.6 using FEBio. In order to apply force to the breast phantom, we used two paddles: (1) Top paddle, and (2) Bottom paddle. The paddles are modelled as rigid bodies in FEBio software to simulate a rigid paddle. There are two types of paddles for breast compression: rigid and flexible [127]. Since our objective is to simulate the compression process to create a flattened model for EM simulation, we have chosen to use a rigid paddle. Figure 2.6a illustrates the system's initial state; at this point, there is contact between the top and bottom paddles and the skin layer. We set zero displacement and zero rotation for the bottom paddle across all Cartesian directions (X, Y, Z). The top paddle allows for vertical movement to compress the breast phantom. It is programmed to gradually apply a 121.34 N target force once it contacts the surface of the breast phantom until this target is achieved. Figure 2.6b illustrates the end of the simulation, where the top paddle reaches a force of 121.34 N [124].

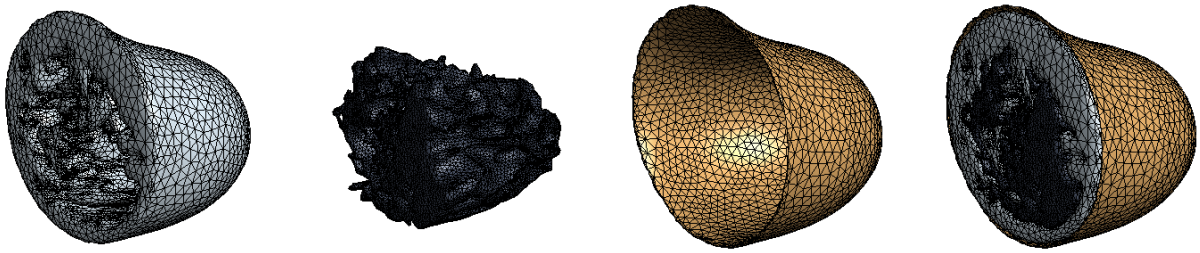


(a) (b)

Figure 2.6: Illustration of the initial and end compression simulation of ARBP ACR Class 3-Heterogeneously Dense Phantom 3 Breast ID: 062204. 2.6a Geometry TetGen initial position and Contact position. 2.6b Geometry TetGen Applied force 121.34 N.

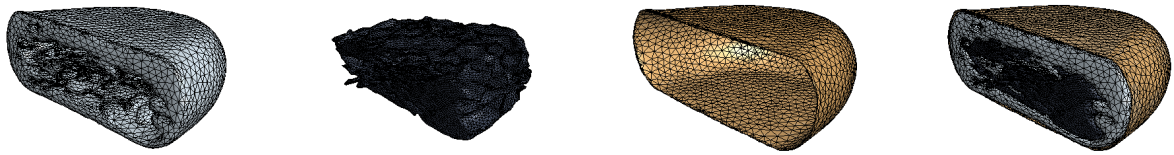
2.3.1 Compression results of the realistic breast phantom - Class 3- Heterogeneously Dense Phantom 3 Breast ID: 062204

Figure 2.7 illustrates the initial uncompressed breast model: Figure 2.7a represents the uncompressed fat geometry model, Figure 2.7b pictures the uncompressed fibro glandular geometry model in TetGen, Figure 2.7c shows the uncompressed skin geometry model, and Figure 2.7d displays whole 3D uncompressed geometry model, The final compressed geometry resulting from the compression process is shown in Figure 2.8. In the picture, we can see the compressed skin layer shown in Figure 2.8a, the compressed fat layer in Figure 2.8b, and the fibro glandular layer in Figure 2.8c. Finally, the whole 3D compressed breast phantom model is presented in Figure 2.8d. Figure 2.9 below shows the position (in mm) of the top paddle relative to the force applied (in N).



(a) (b) (c) (d)

Figure 2.7: Uncompressed view of the ARBP ACR Class 3- Heterogeneously Dense Phantom 3 Breast ID: 062204. 2.7a Geometry TetGen uncompressed fat . 2.7b Geometry TetGen uncompressed fibro. 2.7c Geometry TetGen uncompressed skin. 2.7d Complete view of the uncompressed phantom.



(a) (b) (c) (d)

Figure 2.8: Compressed view of the ARBP ACR Class 3- Heterogeneously Dense Phantom 3 Breast ID: 062204. 2.8a Geometry TetGen compressed fat . 2.8b Geometry TetGen compressed fibro. 2.8c Geometry TetGen compressed skin. 2.8d Complete view of the compressed phantom.

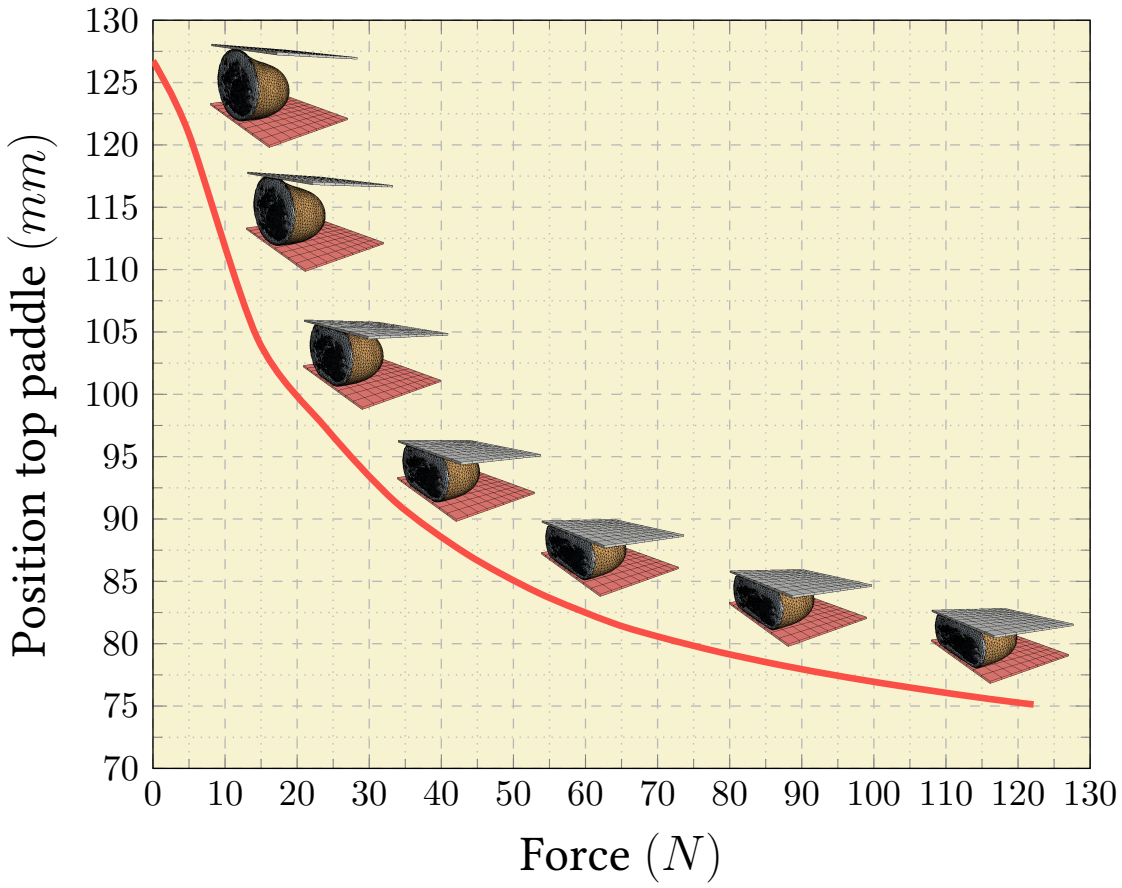
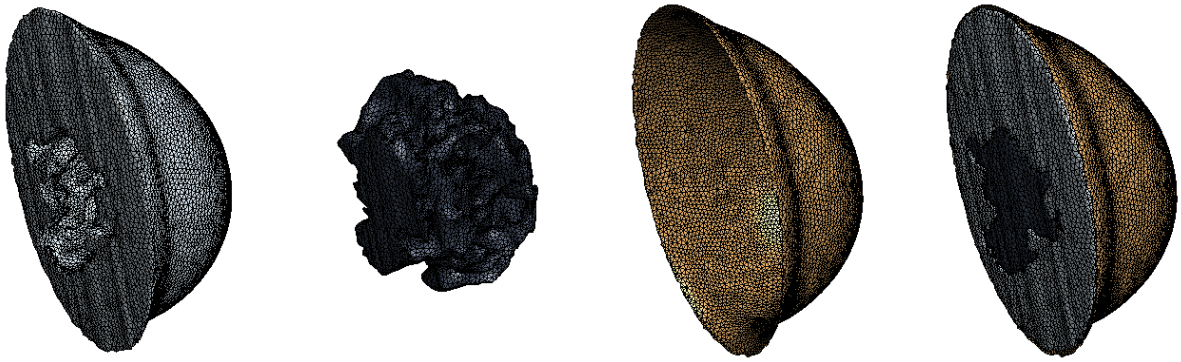


Figure 2.9: Force vs position paddle top over Skin, Fatty, and Fibro Material for ARBP ACR Class 3- Heterogeneously Dense Phantom 3 Breast ID: 062204

2.3.2 Compression results of the realistic breast phantom - Class 4 - Very Dense Phantom 1 Breast ID: 012304

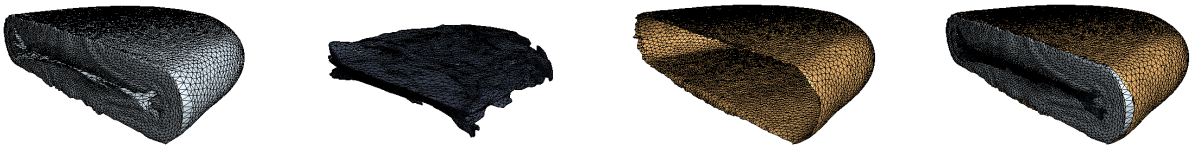
In the case of a very dense breast phantom, the target force applied by the top paddle was 121.32 N to simulate breast compression. To illustrate the compression effect on the breast phantom model, we present the uncompressed and compressed models in Figures 2.10 and 2.11, respectively. In Figure 2.10, we can see the initial state of the uncompressed layers of fat, fibro glandular, and skin in Figures 2.10a, 2.10b, and 2.10c, respectively. Figure 2.10d shows the complete uncompressed 3D geometry model. The compressed layers of fat, fibro glandular

and skin tissues are illustrated in Figures 2.11a, 2.11b, and 2.11c, respectively. A 3D model encompasses the three layers, as shown in Figure 2.11d. The thickness of the compression breast phantom at 121.32 N reached approximately 52 mm; the complete results, including the position of the top paddle and the applied force, are presented in Figure 2.12.



(a) (b) (c) (d)

Figure 2.10: Uncompressed view of the ARBP ACR Class 4 - Very Dense Phantom 1 Breast ID: 012304. 2.10a Geometry TetGen uncompressed fat. 2.10b Geometry TetGen uncompressed ffibro. 2.10c Geometry TetGen uncompressed skin. 2.10d Complete view of the uncompressed phantom.



(a) (b) (c) (d)

Figure 2.11: Compressed view of the ARBP ACR Class 4 - Very Dense Phantom 1 Breast ID: 012304. 2.11a Geometry TetGen compressed fat . 2.11b Geometry TetGen compressed ffibro. 2.11c Geometry TetGen compressed skin. 2.11d Complete view of the compressed phantom.

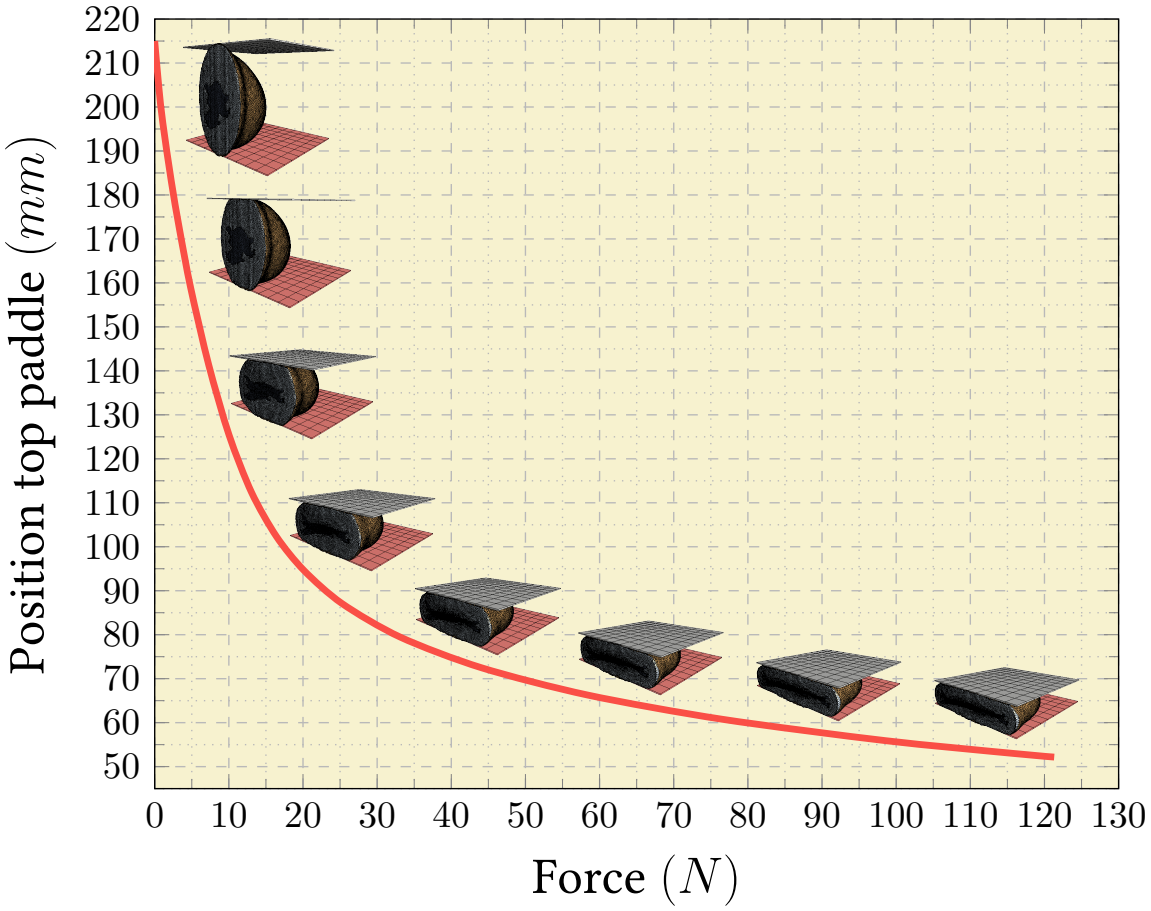
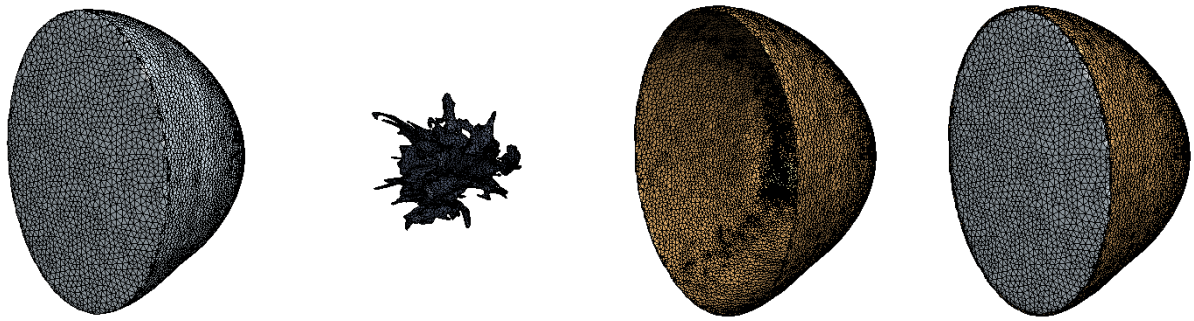


Figure 2.12: Force vs position paddle top over Skin, Fatty, and Fibro Material for ARBP ACR Class 4 - Very Dense Phantom 1 Breast ID: 012304

2.3.3 Compression results of the realistic breast phantom - Class 1- Mostly Fatty Phantom 1 Breast ID: 071904

The final example in this work refers to the predominantly fatty breast phantom, to which the same simulated compression process was applied. As suggested in the literature, a target force of 121.34 N was set on the top paddle, resulting in a thickness of approximately 57 mm with this applied force. A complete set of uncompressed geometry models for fat, fibro glandular, and skin is shown in Figures 2.13a, 2.13b, and 2.13c; meanwhile, Figure 2.13d presents the whole 3D model for this breast phantom. The complete set of simulated compression models is illustrated

in Figure 2.15. The compressed versions of the fat, fibro glandular, and skin tissues are shown in Figures 2.14a, 2.14b, and 2.14c, respectively. Additionally, Figure 2.14d depicts the entire 3D model.



(a) (b) (c) (d)

Figure 2.13: Uncompressed view of the ARBP ACR Class 1- Mostly Fatty Phantom 1 Breast ID: 071904. 2.13a Geometry TetGen uncompressed fat . 2.13b Geometry TetGen uncompressed ffibro. 2.13c Geometry TetGen uncompressed skin. 2.13d Complete view of the uncompressed phantom.



(a) (b) (c) (d)

Figure 2.14: Compressed view of the ARBP ACR Class 1- Mostly Fatty Phantom 1 Breast ID: 071904. 2.14a Geometry TetGen compressed fat . 2.14b Geometry TetGen compressed ffibro. 2.14c Geometry TetGen compressed skin. 2.14d Complete view of the compressed phantom.

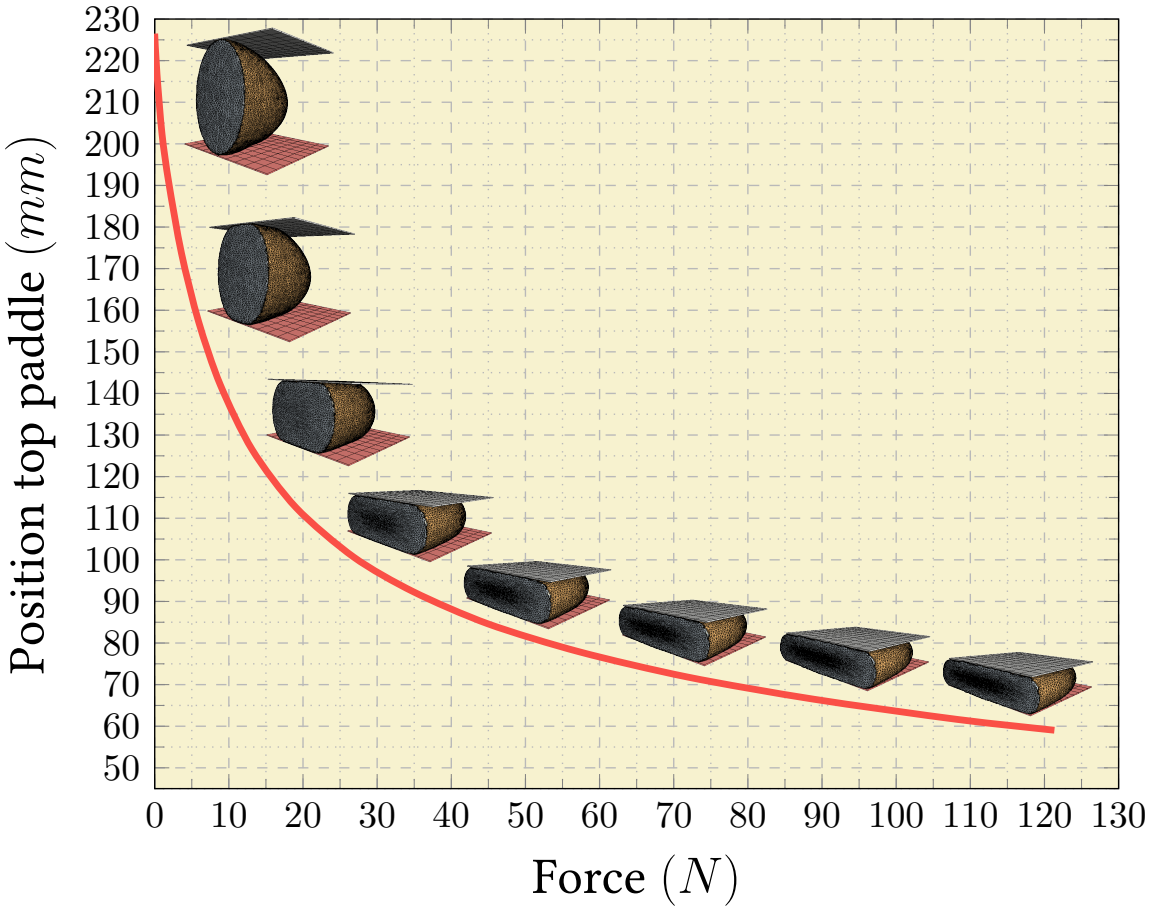


Figure 2.15: Force vs position paddle top over Skin, Fatty, and Fibro Material for ARBP ACR Class 1- Mostly Fatty Phantom 1 Breast ID: 071904

2.4 Conclusion

In this part of the study, anatomically realistic breast phantoms were successfully compressed using biomechanics finite element analysis. We present three phantoms for compression: (1) phantom ACR Class 3- Heterogeneously Dense Phantom 3 Breast ID: 062204 (2) phantom ACR Class 4 - Very Dense Phantom 1 Breast ID: 012304 (3) phantom ACR Class 1- Mostly Fatty Phantom 1 Breast ID: 071904. Initially, phantoms consist of nine tissue layers, resulting in a complex geometry for meshing TetGen. We used MATLAB ® to manipulate the phantoms,

reducing the geometry complexity from nine layers to three tissue layers: (1) fat, (2) fibro, and (3) skin. After simplifying the tissue layers, we utilized the 3D Slicer software to create the geometry, which we then enhanced using Meshmixer before simulating physical compression.

This work applied a compression force of 121.34 N for each of the three simulated phantom models. After compression, the resulting measurements of breast thickness were as follows. The class 3 phantom thickness was 75 mm, the class 4 phantom thickness was 52 mm, and the class 1 phantom thickness was 57 mm.

This study demonstrated the feasibility of using biomedical finite element analysis to compress the complex geometry of an anatomically realistic breast phantom. It also provided a set of compressed phantoms for further EM simulation and testing of microwave devices in a realistic scenario.

Chapter 3

Microwave low frequency scanning in the near-field for cancer detection

3.1 Introduction

This study introduces a novel MW low-frequency scanning technique to detect BC. This method utilizes energy collected near the object being examined to generate a contrast image based on the dielectric properties of the breast. It uses a low-frequency microwave source in conjunction with an innovative sensor based on MW MS to detect the EM energy transmitted from the MW source as it passes through the breast. The intensity of the MW energy captured by the sensor is recorded as a 2D matrix, which is then transformed into an image for classification using AI.

This study proposed that scanning microwave energy in a parallel plane close to the material being examined generates a unique and specific representation of the material by recording a portion of the transmitted MW energy. In this endeavor, we present the application of a novel low-frequency probe to detect anomalies in the human body using MW. The system will scan a ARBP illuminated by an electrically small dipole antenna operating at 700 MHz. Using this novel probe to capture EM radiation that flows through the breast as a contrast image, we can construct an image of $n \times n$ pixels resolution that contains the information of the constituents of the breast, and we can use this image to identify whether the tissue is healthy or unhealthy.

3.2 Theory and application methodology

EM energy can be transmitted, reflected, or absorbed in interaction with the medium, and this dynamic relation depends on the constitutive parameters of the material. Then, when a MW source illuminates a OUT, the dielectric composition of this object influences the amount of energy transmitted by the EM source, and this portion of the transmitted energy provides crucial information on the composition of OUT. It is also true that introducing a perturbation in the medium in question will produce a change in the transmitted energy; consequently, the transmitted energy will encrypt the new condition of OUT. Therefore, in both cases, with and without perturbation, the transmitted energy will encapsulate information specifically about the unique composition of the current status of the medium, which, more importantly, leads to a distinctive and unrepeatable representation of the material. This phenomenon also manifests itself in heterogeneous materials such as human tissue. In this case, the energy transmitted from the source MW encrypts the status of the part of the human body under examination.

We propose that by performing a plane scan near OUT, a portion of the transmitted energy can be collected and utilized to produce a unique and distinctive representation of the medium under examination. Figure 3.1 illustrates this concept: a MW source, denoted as T_x, illuminates an OUT. A portion of the MW energy passes through and is transmitted, while some of this transmitted energy can be collected by a receiver, denoted by R_x when scanning the plane close to OUT. The scan starts from the initial position $(1, 1)$ and moves forward in a direction until it reaches position $(1, n)$, then the scan moves in reverse to reach position $(2, 1)$, and so on, until the end at position (n, n). After performing a complete scan of the 2D MW plane energy from the original OUT, the magnitude of the energy is saved in a 2D array. This array can then be transformed into a 2D image of n$\times$n pixels that represents the dielectric properties of OUT. Introducing a perturbation within the dielectric material of OUT will result in a change in the MW energy transmitted, and then a new scan will capture this change in a new 2D matrix of energy magnitudes. This new image will exhibit changes from the original without perturbation and, more importantly, serve as an anomaly detection system.

Since this concept involves scanning MW energy to acquire the image contrast of an OUT, it can be extended to detect cancerous anomalies in women's breasts. For that purpose, we can use a dipole MW source operating at low frequency to illuminate the women's breast and a MS-based probe to scan the MW energy in the 2D plane close to OUT. It is important to emphasize that the contrast image obtained from the scanning system does not pretend to be an identical representation of the inside properties of the breast tissue but a contrast image that represents the material ϵ_r. This contrast image is unique, as is the foundation of the proposed anomaly detection scanning system. Two other important properties that make this technique suitable are the fact that both women's breasts can be considered similar in size and shape [135, 136] and

a small probability of developing a tumor in both breasts simultaneously [137, 138, 139, 140].

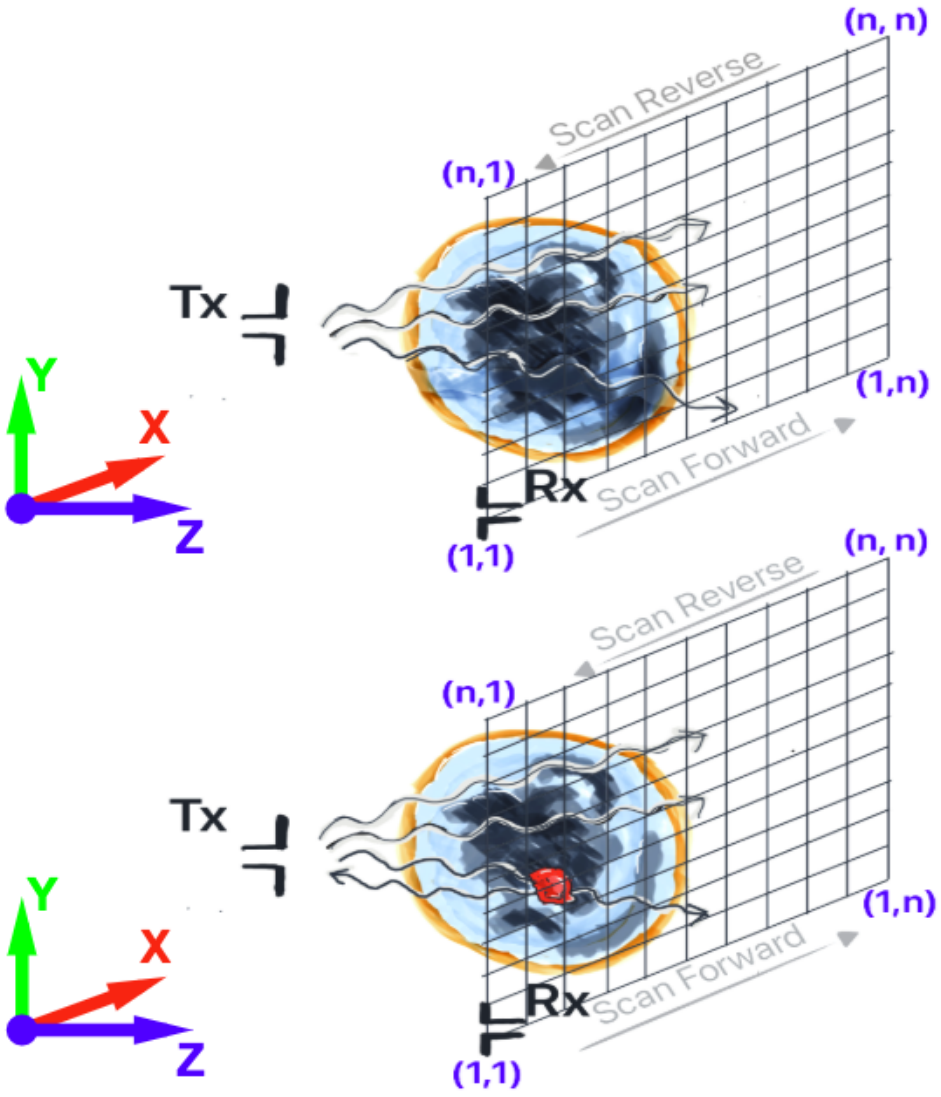


Figure 3.1: RF-Scanning energy concept illustration. Composed by: MW energy source, the Object Under Test (OUT), and the plane to be scanned

As the device needs to collect the energy of the transmitted EM wave, we can model it as an absorber of MW energy. Absorbers have several applications in many fields, such as evading

radar signals in defense [141]. The absorber design aims for optimal alignment to enable deep penetration of EM waves into the absorber structure[142]. In particular, for this work, the absorber will be matched to the free-space impedance and greatly reduces the reflection of the MW energy. The top layer of the absorber, displaying the geometric shape UC, generates currents when the MW signal interacts with the cell. This interaction induces electric and magnetic fields, leading to maximum EM absorption. An absorber grounded by metal in the bottom layer, as modeled in Figure 3.2, has its input impedance expressed by Equation 3.1:

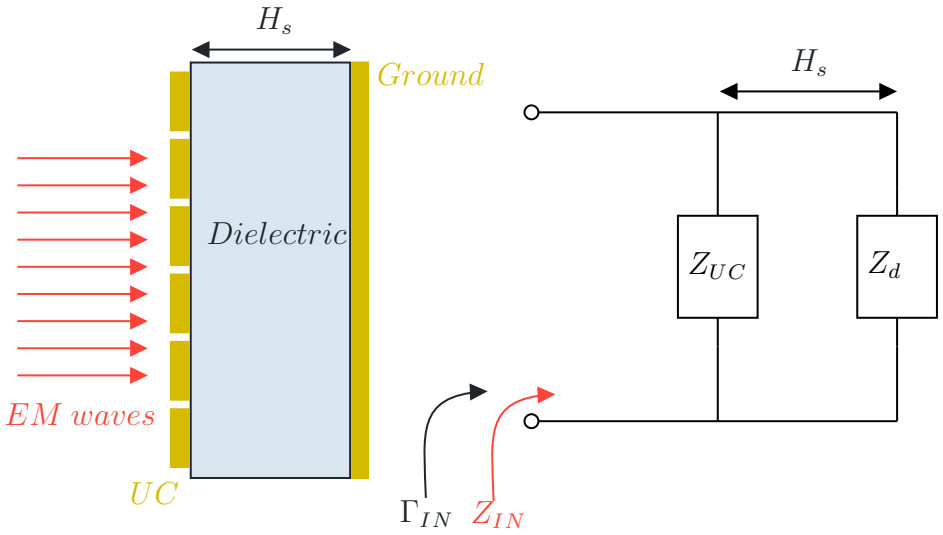


Figure 3.2: MW Absorber circuit model. Z_d is the equivalent impedance of the substrate, H_s thickness of the substrate, and Z_{UC} is the impedance of the UC.

$$Z_{in} = Z_{UC} || Z_d \tag{3.1}$$

Where Z_d is the equivalent impedance of the substrate that has a thickness of H_s, and it represents by the Equation $Z_d = \left(Z_0/\sqrt{\epsilon_r}\right) \tan(\beta t)$, Z_0 it is the characteristic impedance, β is the propagation constant and t is the thickness of the substrate H_s in Figure 3.2. Then Z_{in} derived in the following Equation 3.2:

$$Z_{in} = Z_{UC} || \left(Z_0/\sqrt{\epsilon_r}\right) \tan(\beta t) \tag{3.2}$$

When the circuit of Figure 3.2 resonates, the magnitudes of the impedance Z_{UC} and Zd are equal, but the phases are opposite, making the value of Z_{in} purely real. The impedance of the absorber and the free space will be equal when the reflection is minimum Equation 3.3 resulting in maximum absorption by the MS. The relationship between the absorption, reflection, and transmission of the absorber device can be described by Equation 3.4.

$$\Gamma_{in} = \frac{Z_{in} - Z_0}{Z_{in} + Z_0} \tag{3.3}$$

$$A(\omega) = 1 - R(\omega) - T(\omega) = 1 - |s_{11}|^2 = 1 - \left|\frac{Z_{in} - 120\pi}{Z_{in} + 120\pi}\right|^2 \tag{3.4}$$

Where A(ω), R(ω) and T(ω) stand for absorption, reflection, and transmission of the Electric-Inductive-Capacitive (ELC), and $R(\omega) = |S_{11}|^2$ and $T(\omega) = |S_{21}|^2$.

3.3 Numerical simulation

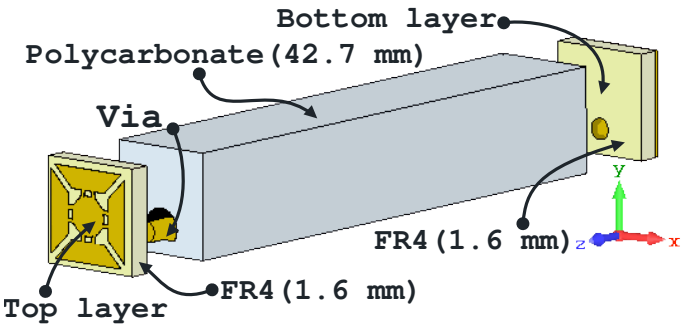
The MW sensor presented in this study in Figure 3.3 is based on a unit ELC cell that enhances inductive capacitance effects. These cells have a specific geometric shape designed to resonate at 700 MHz. The geometric design of the cell was chosen to be symmetric to enhance absorption in all directions [143]. The substrate used in the design is *polycarbonate* with $\epsilon_r = 2.9$ [144] and FR-4 with $\epsilon_r = 4.3$. The selection of these two materials allows for low-cost manufacturing of the probe. FR-4 is the global standard for the fabrication of Printed Circuit Board (PCB) and is available at a low cost in thicknesses up to 6 mm. The thickness of this MS-based sensor of 42.7 mm was determined by optimization with EM software. Polycarbonate, a relatively inexpensive material, can be used to achieve this thickness and by combining FR-4 and polycarbonate, we can successfully fabricate this innovative device.

The UC is constructed by simulating a waveguide and employing two ports for its excitation sources. The boundary conditions are defined as electrically and magnetically perfect conductors for the xz and yz planes, respectively. In the z-direction, an open space condition is assumed. The boundary conditions described permit propagation of the TEM mode. The dimensions of the design unit cell were determined using CST ® software to ensure optimal performance at the desired frequency. The optimized sensor sizes are listed in Table 3.1. A 3D view of the model design is presented in Figure 3.3a, while Figure 3.3b illustrates the top layer and Figure 3.3c depicts the bottom layer. Using the expressions from Equation 3.4, the respective absorption, reflection and transmission are computed and illustrated in Figure 3.4,

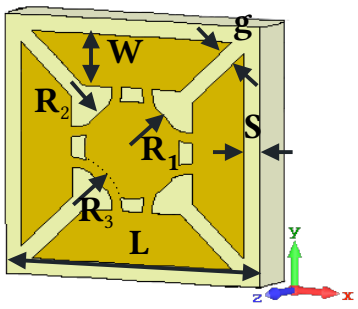
while the efficiency achieved by the cell (when present in a periodic array of cells) is shown in Figure 3.5.

Table 3.1: List of parameters of the designed ELC according Figures 3.3a, 3.3b, and 3.3c

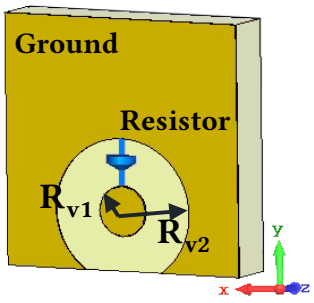
Parameter	Value	Unit	Parameter	Value	Unit
L	8.0	mm	H	42.7	mm
W	1.6	mm	S	0.5	mm
g	0.5	mm	R_1	1.3	mm
R_2	1.3	mm	R_3	1.6	mm
R_{v1}	0.8	mm	R_{v2}	2.3	mm



(a)



(b)



(c)

Figure 3.3: ELC resonance frequency at 0.7 GHz, perspective, front, and back view. 3.3a ELC perspective view. Top and bottom dielectric material FR-4, and inter-media material polycarbonate. Resonance frequency at 0.7 GHz. 3.3b ELC top view. 3.3c ELC bottom view

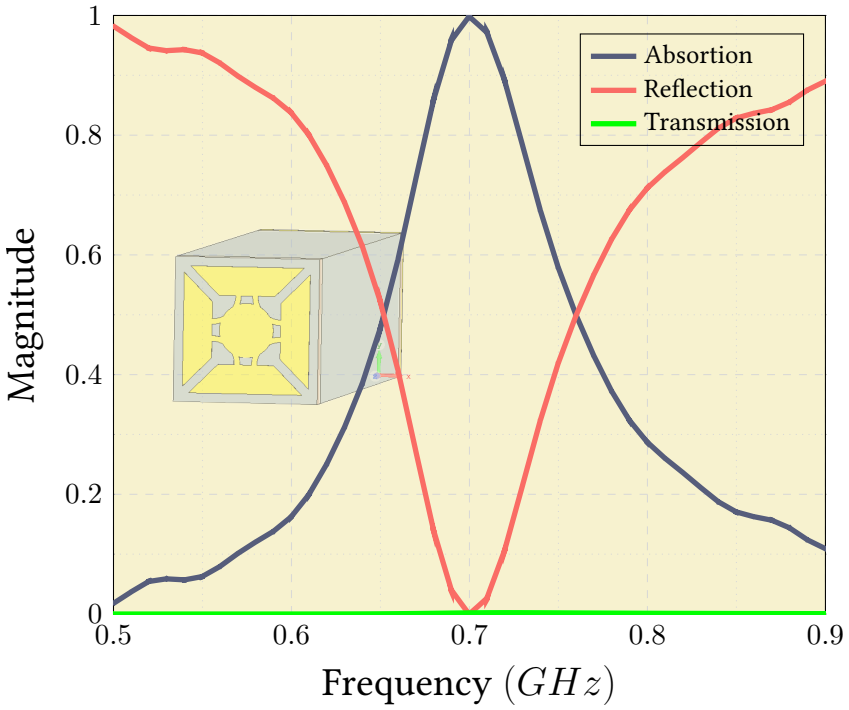


Figure 3.4: Simulation results of the UC ELC absorption, reflection, and transmission

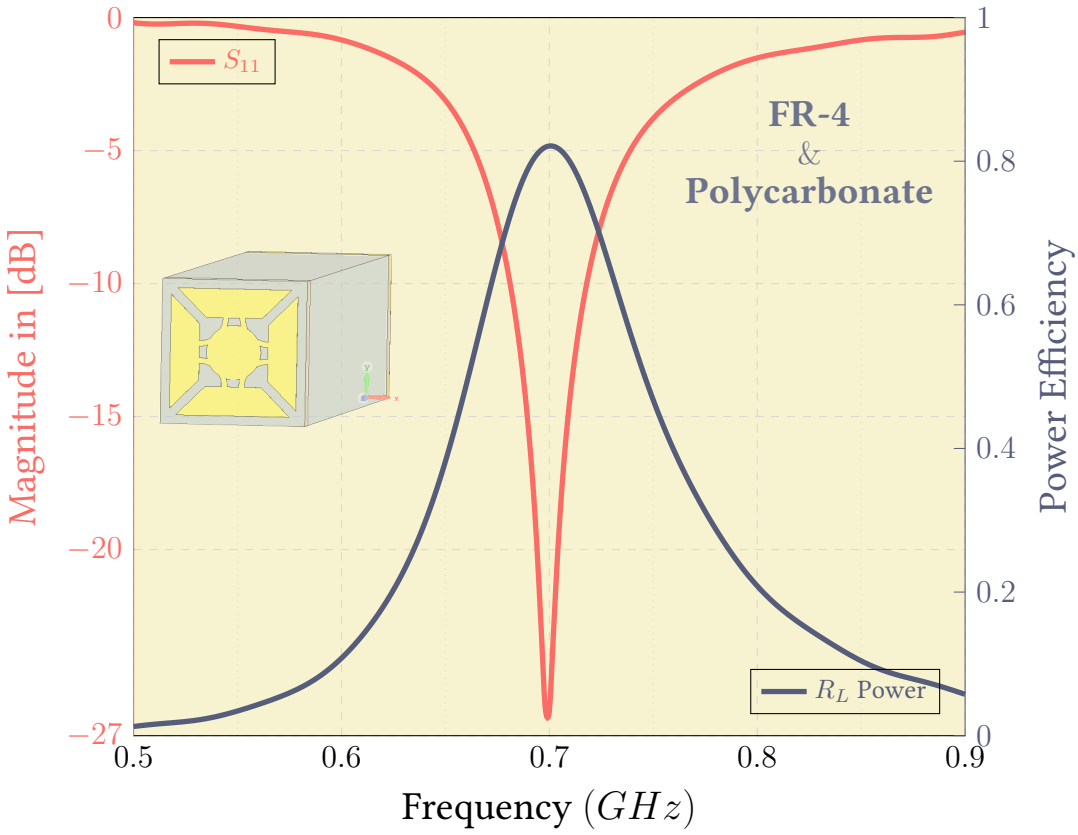


Figure 3.5: Simulation results ELC efficiency, data from 0.5 to 0.9 GHz, case FR-4 and polycarbonate

In theory, the system depicted in Figure 3.1 can cover a substantial area, enabling it to function as a virtual MS. The MS-based sensor discussed in this work can accommodate various configurations of $N \times N$ arrays; however, only the core cell is intended to measure microwave energy. Unfortunately, simulation time costs are highly demanding; for example, simulating a grid of 30×30 requires significant time and computer resources, making it impractical to conduct extensive simulations using EM software. For this reason, this study has implemented a brief simulation to test the concept, followed by an empirical phase to validate its ultimate effectiveness.

It is essential to emphasize the purpose of using inexpensive materials to make the fabrication of this device affordable. The effect of the material substrate on the efficiency of this cell is

illustrated in Figures 3.5, 3.6, and 3.7. Using a material with relatively high ϵ_r, such as TMM13i, allows a greater flow of EM energy to the resistor located in the bottom layer. As illustrated in Figure 3.7, the efficiency is almost perfect. In contrast, the use of FR4 and polycarbonate offers a satisfactory level of power absorption at a lower cost, making the fabrication of this device feasible. The efficiency in Figure 3.5 is achieved 81% at 700 MHz; this represents the power level of the absorber device presented in this study. Using only FR-4, the design presented in Figure 3.6 achieves slightly below the efficiency 80%. This value could be improved through optimization; however, that is beyond the scope of this work.

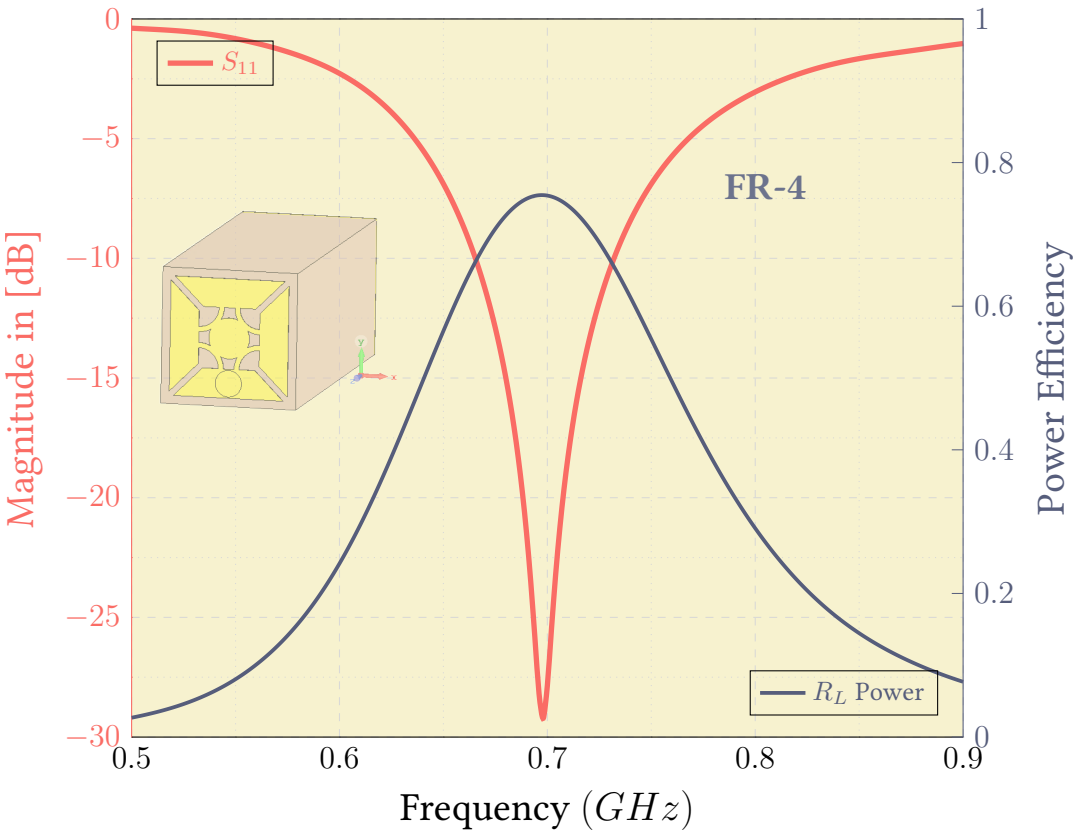


Figure 3.6: Simulation results ELC efficiency, data from 0.5 to 0.9 GHz. , case FR-4.

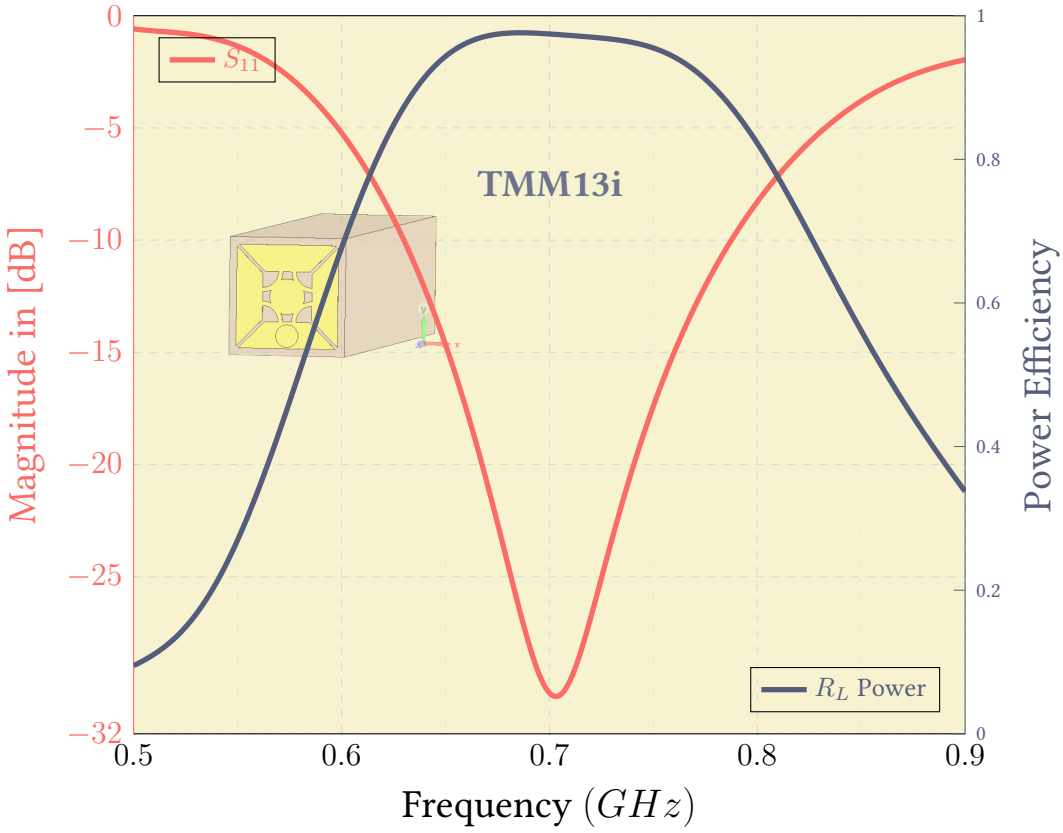


Figure 3.7: Simulation results ELC efficiency, data from 0.5 to 0.9 GHz. Case TMM13i

This study uses numerical anatomically realistic breast phantoms sourced from the repository described in [117]. The database includes nine Anatomically Realistic Breast Phantoms (ARBP), modeled according to the dielectric properties outlined in [90]. The computationally realistic phantoms were constructed using full-wave EM simulation software CST ® [95] and MATLAB ® [94]. Details of the generation process are provided in [96]. The Cole-Cole curves, derived using parameters from [145, 90], were used to create the phantoms depicted in Figure 3.8a.

The breast consists primarily of three main components: skin tissue, fibroglandular tissue, and fat tissue. The density of the breast is classified by ACR as follows: almost entirely fatty breast with fibrous and glandular tissue that constitutes 25% or less, scattered fibroglandular tissue that makes up 25% to 50%, heterogeneously dense breast with fibrous and glandular tissue

that comprises 51% to 75%, and extremely dense breast with more fibrous and glandular tissue than 75% [93]. This study specifically used a heterogeneously dense breast classified as a Class 3 phantom (ID 062204) from the reference repository [117]. This selection was made due to the challenges associated with detecting anomalies in dense breast tissue: approximately 15% of anomalies go undetected and it is estimated that 25% of women have dense breasts [7].

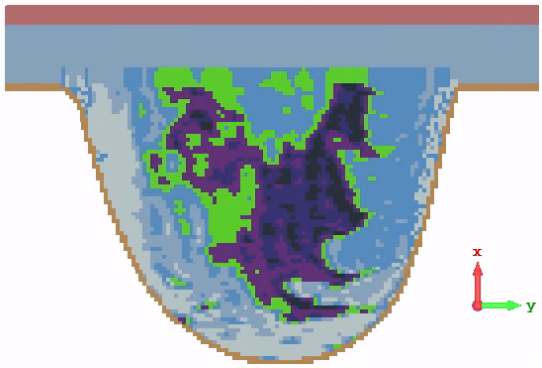
The results of simulating three scenarios using a realistic breast phantom, with and without a tumor, for two different sizes and positions are presented in Figure 3.8b, Figure 3.9b, and Figure 3.10b. Although the images depict three distinct conditions of the breast phantom, these differences are difficult to discern with naked sight. To illustrate how this technique can obtain breast information, Figure 3.8c, Figure 3.9c, and Figure 3.10c are presented using Histograms of Oriented Gradients (HOG). This technique was first introduced to detect humans [146] and has since been used in artificial vision to identify human activities in images and videos, as well as to detect animals [147]. It has also improved cancer detection through image analysis by decreasing false positives using Regions of Interest (ROI) from 54×54 pixel images. In conjunction with other techniques, the approach HOG has been proposed to aid in the detection of skin cancer [148] and stomach cancer and to assist in the diagnosis of this condition [149].

The calculation using HOG on an image of $I_m \times I_n$ pixels starts by dividing the original image into small regions using circular or rectangular blocks [146] of the size of $B_w \times B_w$, and each block is made up of $C_b \times C_b$ cells. Generally speaking, the first step is the calculation of the gradient Equation 3.5, the magnitude of the gradient Equation 3.6, where G_x is the horizontal gradient, G_y is the vertical gradient, c and r denote columns and rows, respectively, $|G|$ is the magnitude of the gradient; and the direction angle Equation 3.7. These values are calculated for each pixel (x, y) in the cell, and then the histogram is filled using the magnitude of the gradient in each bin that represents the orientation interval of each cell. The orientation cell can be divided into $n - bins$ using a scale of 0° to 180° degrees or 0° to 360° degrees; for example, from 0° to 180° degrees, 9-bins can be defined as [0° - 20°], [20° - 40°], [40° - 60°], . . . , [160° - 180°] . In this study, Figure 3.8c, Figure 3.9c, and Figure 3.10c were developed considering image size as 30×30 pixels, with cell size of 2×2 and block size 2×2. The orientation consists of 9 bins ranging from 0 to 180 degrees.

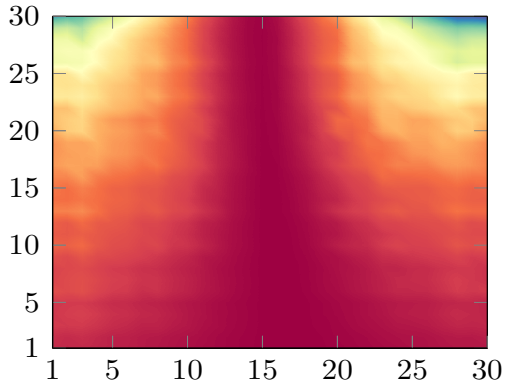
$$\begin{aligned} G_x(r,c) &= p(r,c+1) - p(r,c-1) \\ G_y(r,c) &= p(r+1,c) - p(r-1,c) \end{aligned} \tag{3.5}$$

$$|G| = \sqrt{G_x^2 + G_y^2} \tag{3.6}$$

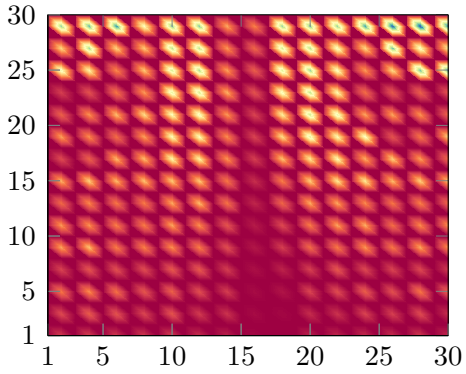
$$\theta = \tan^{-1}\left(\frac{G_y}{G_x}\right) \tag{3.7}$$



(a)

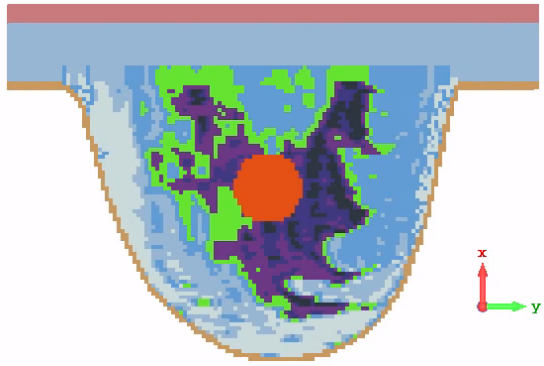


(b)

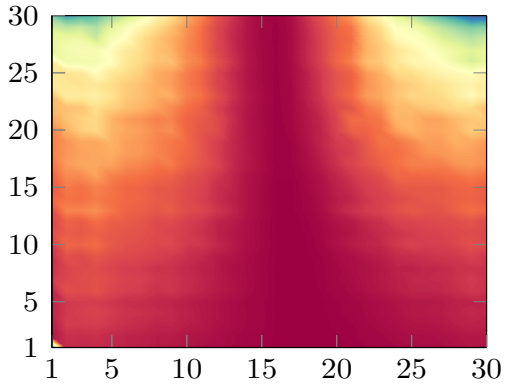


(c)

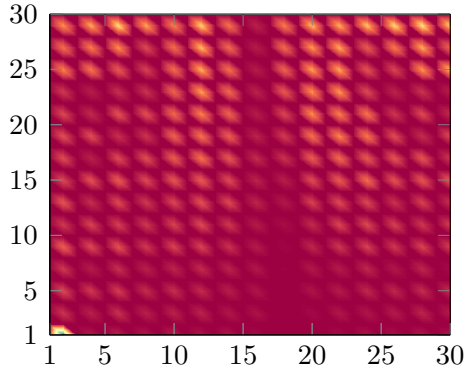
Figure 3.8: CST ® Simulation results using MW energy scanning 5x5 sensor, and heterogeneously dense breast identified as a Class 3 phantom (I.D. 062204). 3.8a XY cut of the simulated ARBP. 3.8b Simulation in CST ®, 900 samples by scanning 30×30 positions vertically and horizontally. 3.8c HOG representation of the Figure 3.8b.



(a)

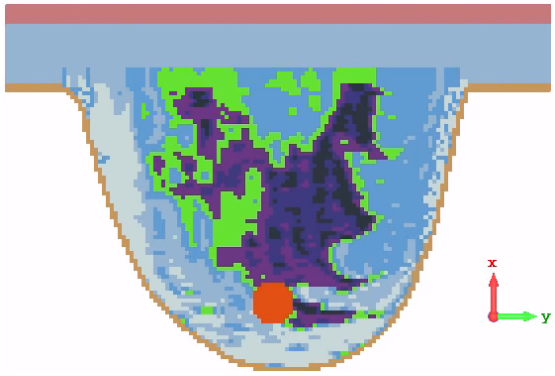


(b)

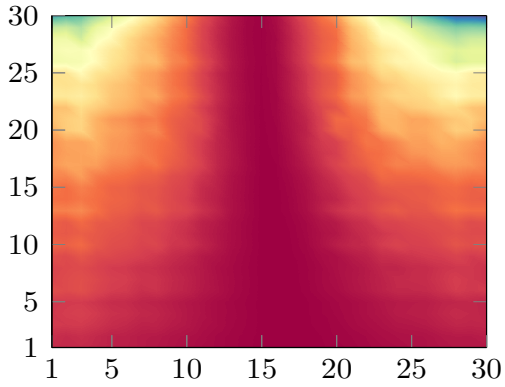


(c)

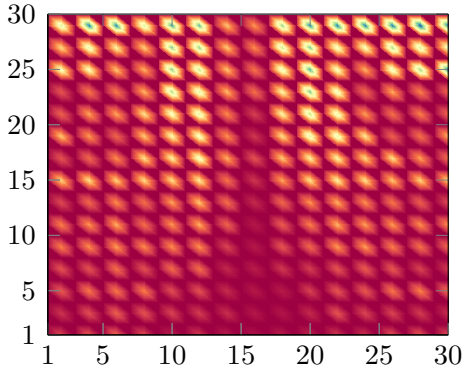
Figure 3.9: CST ® Simulation results using MW energy scanning 5x5 sensor, and heterogeneously dense breast identified as a Class 3 phantom (I.D. 062204) with 10 mm radius tumor. 3.9a XY cut of the simulated ARBP with 10 mm radius tumor. 3.9b Simulation in CST ®, 900 samples by scanning 30×30 positions vertically and horizontally with 10 mm radius tumor. 3.9c HOG representation of the Figure 3.9b.



(a)



(b)



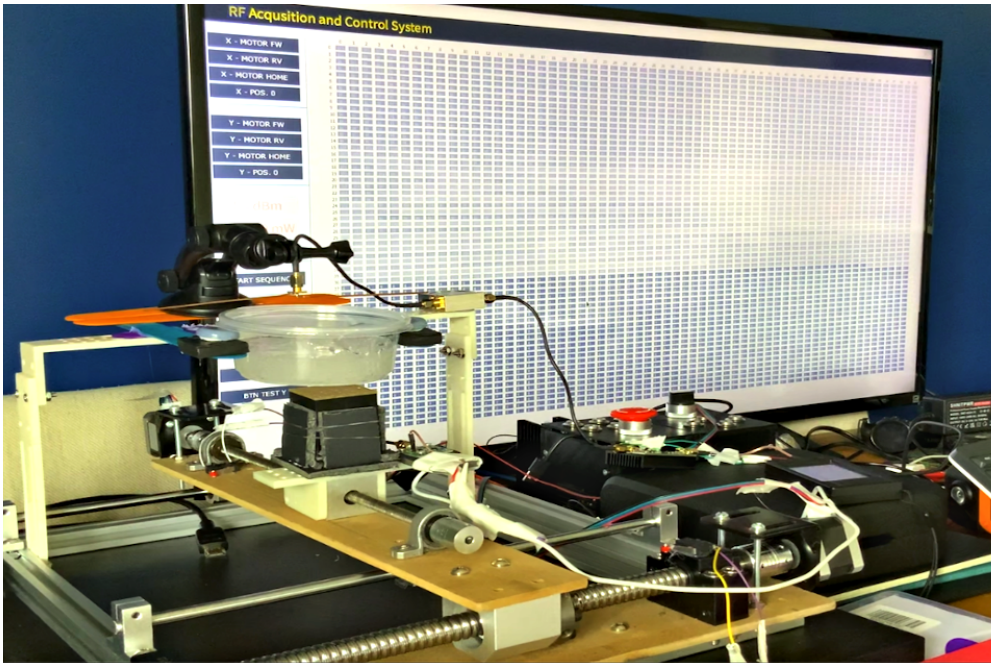
(c)

Figure 3.10: CST ® Simulation results using MW energy scanning 5x5 sensor, and heterogeneously dense breast identified as a Class 3 phantom (I.D. 062204) with 7 mm radius tumor. 3.10a XY cut of the simulated ARBP with 7 mm radius tumor. 3.10b Simulation in CST ®, 900 samples by scanning 30×30 positions vertically and horizontally with 7 mm radius tumor. 3.10c HOG representation of the Figure 3.10b.

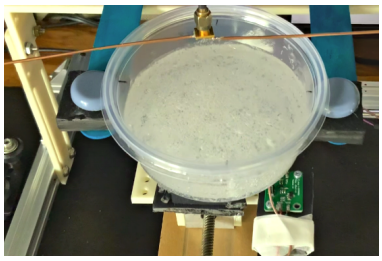
3.4 Experimental results

This section presents the experimental setup for the concept of MW energy scanning acquisition, which we presented in the previous section. Due to the high computational and time costs of implementing a large EM simulation, we have decided to proceed with an experimental validation that generates enough images to classify healthy and unhealthy breast tissue. To estimate the cost of simulation resources for this work, consider that the completion of a single EM simulation takes eight days, assuming that there are no errors. Due to this limitation, we chose to advance to an experimental stage that allows us to probe the potential of this technique for detecting anomalies. The image resolution for this work is 60×60 pixels; the image resolution is determined by the 0.2 mm accuracy of the screws depicted in the hardware in Figure 3.11g. With $60\times$ 60 samples, the information can be acquired in three minutes, which is fast enough to generate the desired data set.

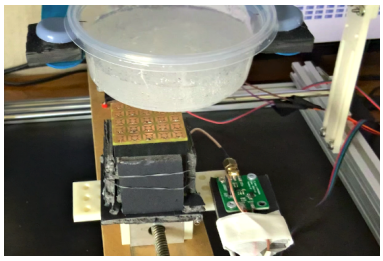
The core concept of this system is that, as the sensor moves along the XY axis to capture MW power, the collected data are transmitted to a matrix and stored in computer memory for subsequent analysis. Figure 3.11 shows the different components used for the implemented MW energy scanning and data acquisition system, consisting of one central microcontroller (to control the scanning system and data acquisition), two step motors (one for controlling the movement of the scanning sensor in the x-direction and the other for the y-direction), two motor drivers (to handle power to the stepper motors), one MW power meter (to transmit the received power from the MW sensor to the microcontroller for data aquisition), one DC power supply (to supply the MW power amplifier and the microcontroller), a MW amplifier (to boost the transmitting power radiating from the transmitter antenna), and various phantoms (for testing different types of objects under examination to make the dataset).



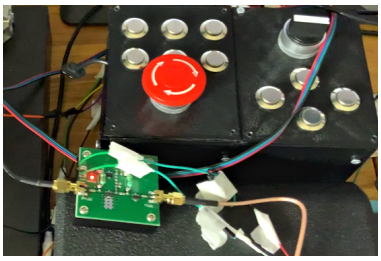
(a)



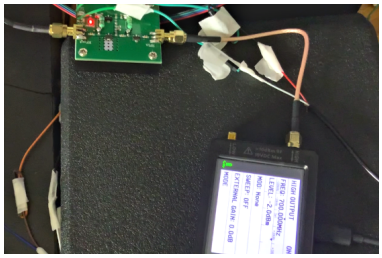
(b)



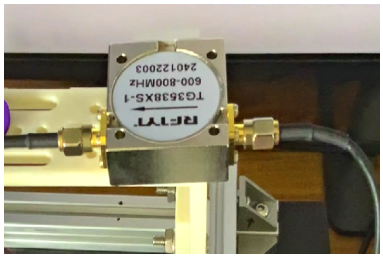
(c)



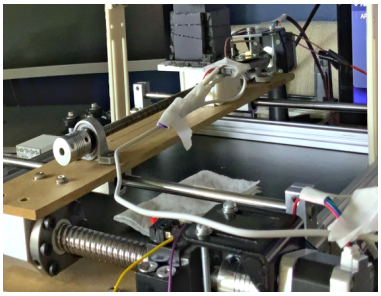
(d)



(e)



(f)

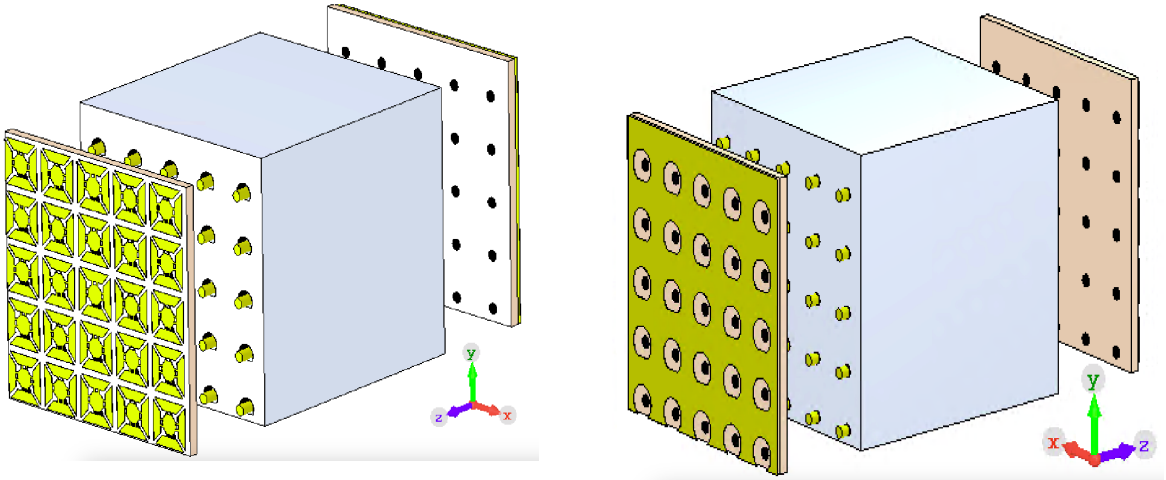


(g)

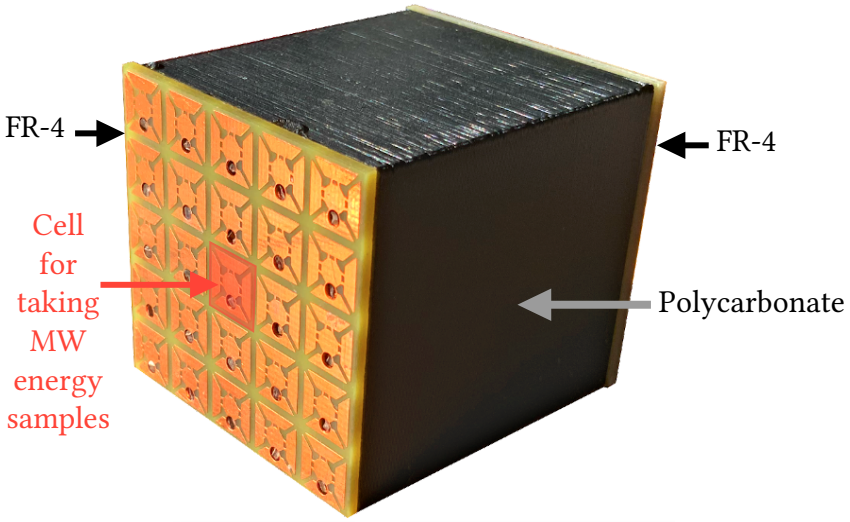
Figure 3.11: 3.11a Overview RF-Scanning system hardware Composed by: 3.11b Dipole antenna operating at 700 MHz. 3.11c Phantom make of TRITON X-100, 5×5 MS sensor, and MW power meter. 3.11d MW power amplifier, manual control, and stop emergency. 3.11e Signal generator. 3.11f MW Isolator. 3.11g Step motors & screws for XY-axis control.

The system employs an MW sensor configured in a 5× 5 matrix. This design can be modified to other configurations, such as 7×7 or 11×11 ELC cells, where an odd number maintains symmetry around the central cell that captures the energy. For this study, a 5×5 sensor is fabricated. The top and bottom layers of FR-4, along with the polycarbonate body, are connected using 25 vias, which can be soldered manually, making it a cost-effective solution. In particular, the top and bottom layers were fabricated separately and the middle substrate was drilled independently. The layers were stacked, a rod was passed through the hole in each cell of matrix 5× 5 and manually soldered. This method significantly reduced fabrication costs because excessive substrate thickness is not compatible with typical PCB fabrication technology, and consequently, the PCB fabrication cost would be significantly increased in the absence of this approach.

Figure 3.12 shows the top and bottom views of the sensor. The sensor captures the EM energy through the center cell. The scanning plane is oriented parallel to the MW source, which in this case is a dipole antenna operating at 700 MHz. The breast phantom is placed between the MW source and the sensor.



(a) (b)



(c)

Figure 3.12: MW sensor 5×5. 3.12a Top view design. 3.12b Bottom view design. 3.12c Fabricated view of MW senser of 5×5 cells. Only the center cell is designed to take the measurements from the scanning system.

Twelve phantoms were made according to [150] with different combinations of TRITON X-100 and water (see Figure 3.13). This non-ionic detergent solution simulates the dielectric property of breast tissue by mixing with distilled water. To create these twelve phantoms, we

use a series of solutions with varying concentrations: 26% TRITON X-100 with 74% water, 28% TRITON X-100 with 72% water, and so on, up to 48% TRITON X-100 with 52% distilled water. These solutions produce typical breast tissue with ϵ_r values ranging from 35 to 60 and in the classification of (0 - 30%) and (31-84%) adipose content. The tumor models were Perfect Electric Conductor (PEC) spheres with diameters of 5, 7, and 10 mm. A computer application was developed to facilitate control and data acquisition. Figure 3.14 shows the schematic diagram of the entire scanning and data acquisition system.

The experiment used a 0.5 W MW power level supplied to the transmitter dipole antenna. This input power level provided a power range of -55 dBm to 0 dBm at the sensor output. The dipole antenna was fixed and powered by an MW amplifier connected to a signal generator operating at 700 MHz, while the sensor moved in the XY plane, following a 60$\times$ 60 2D matrix, row by row, until it covered all 3,600 positions. Once the scan was completed, the collected data were stored in CSV format on the computer for later processing. Each phantom was scanned seven times: once without a PEC sphere, labeled as healthy, and six times with PEC spheres inside, labeled as unhealthy, arranged in two different positions and three different sizes.

The complete set of 84 (7$\times$12) CSV files was then converted to RGB images using Python [151, 152, 153, 154, 155, 156, 157] (see Figure 3.15 which displays the complete set of 7 images for a single phantom model), where the top image shows the phantom without tumor, simulating a healthy breast. It is important to highlight the contrast between this image and the six others, which depict the phantom with PEC spheres placed at two different locations. We emphasize that the core concept for classifying healthy and unhealthy phantoms behind our modality here is the contrast between different images.



(a) (b) (c)

(d) (e) (f)

(g) (h) (i)

(j) (k) (l)

Figure 3.13: Twelve fabricated phantoms using TRITON X-100 and distilled water. 3.13a Fabricated phantom 26% TRITON X-100 and 74% distilled water. 3.13b Fabricated phantom 28% TRITON X-100 and 72% distilled water. 3.13c Fabricated phantom 30% TRITON X-100 and 70% distilled water. 3.13d Fabricated phantom 32% TRITON X-100 and 68% distilled water. 3.13e Fabricated phantom 34% TRITON X-100 and 66% distilled water. 3.13f Fabricated phantom 36% TRITON X-100 and 64% distilled water. 3.13g Fabricated phantom 38% TRITON X-100 and 62% distilled water. 3.13h Fabricated phantom 40% TRITON X-100 and 60% distilled water. 3.13i Fabricated phantom 42% TRITON X-100 and 58% distilled water. 3.13j Fabricated phantom 44% TRITON X-100 and 56% distilled water. 3.13k Fabricated phantom 46% TRITON X-100 and 54% distilled water. 3.13l Fabricated phantom 48% TRITON X-100 and 52% distilled water

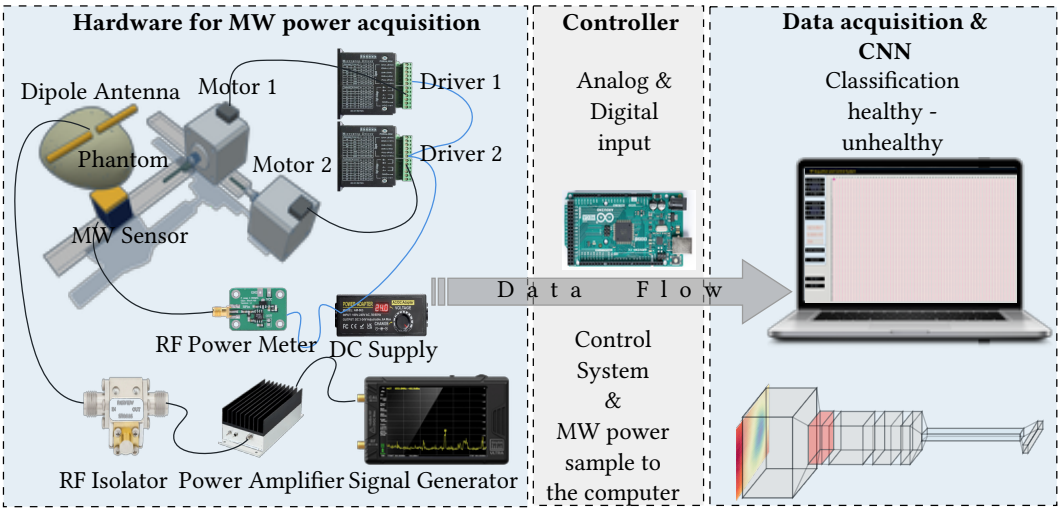


Figure 3.14: RF-Scanning energy system schematic diagram composed by: (1) Phantom fabricated with TRITON X-100 and distillate water, (2) MW MS prove 5×5, (3) Two screws, (4) Two step motors, (5) Two drivers for step motors, (6) MW power amplifier, (7) MW power meter, (8) MW isolator, (9) DC power supply, (10) Signal generator, (11) Micro–controller, and (12) A computer equipped with a detection application.

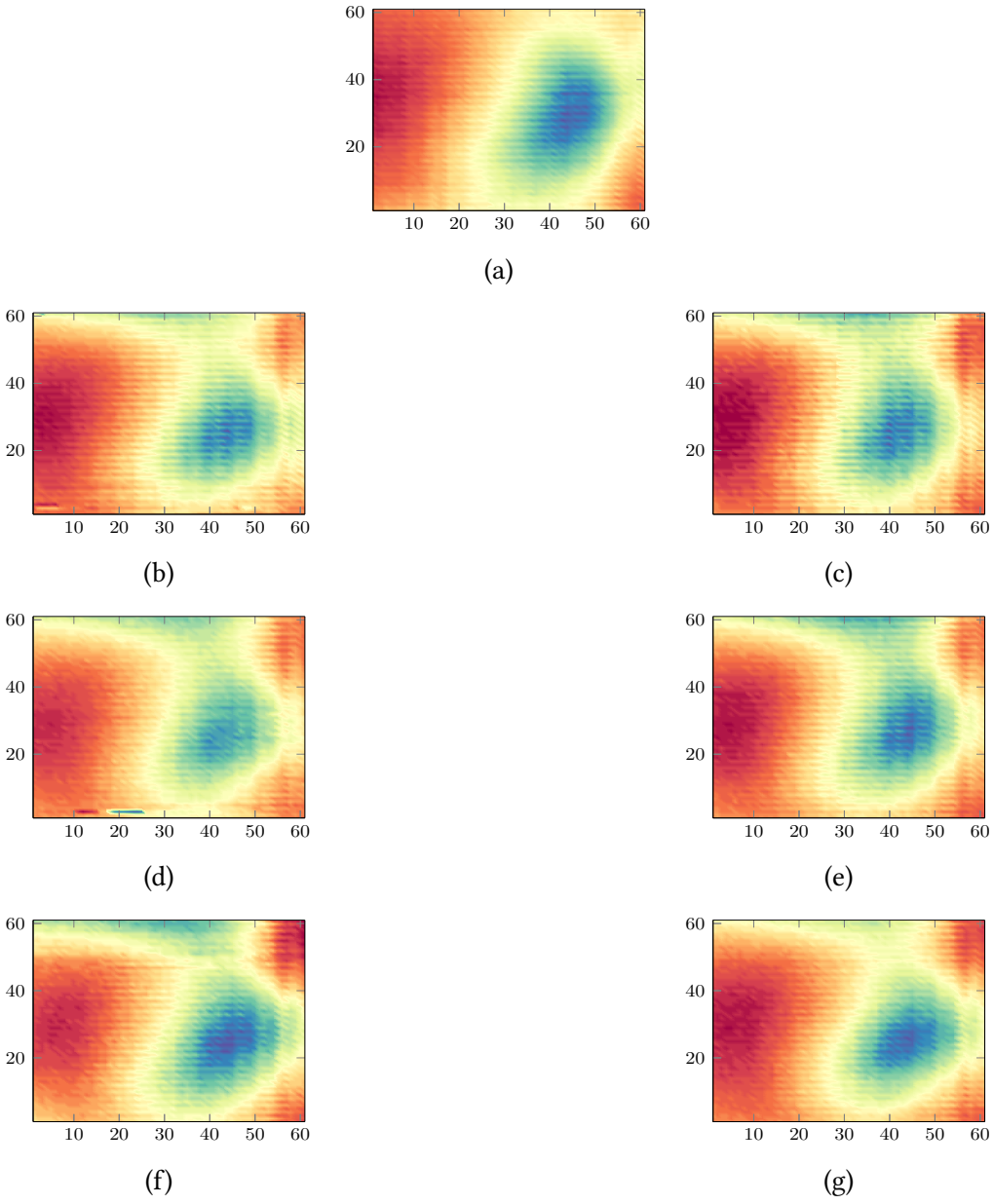


Figure 3.15: Experimental results using MW 5x5 sensor for scanning 60x60 pixels image plane over 110x100 mm^2. 3.15a Scanned healthy phantom, 3.15b Scanned of a phantom with a tumor of 5 mm diameter at the left, 3.15c Scanned of a phantom with a tumor of 5 mm diameter at the right, 3.15d Scanned of a phantom with a tumor of 7 mm diameter at the left, 3.15e Scanned of a phantom with a tumor of 7 mm diameter at the right, 3.15f Scanned of a phantom with a tumor of 10 mm diameter at the left, 3.15g Scanned of a phantom with a tumor of 10 mm diameter at the right.

The final objective relies on CNN due to their effectiveness in automated classification. Figure 3.16 shows the architecture of the CNN model used in this work. The CNN model consists of four 2D convolution blocks, each with a kernel size of 3, a stride and padding set to 1, four Rectified Linear Unit (RELU) blocks, and one max pooling block. The experiments using the trained CNN model shown in Figure 3.16 tested the healthy breast phantom against the unhealthy one, where the Accuracy of tumor detection for sizes of 3, 5, and 7 mm achieved by the trained CNN reached 88.0% (see Table 3.2 and Figure 3.17).

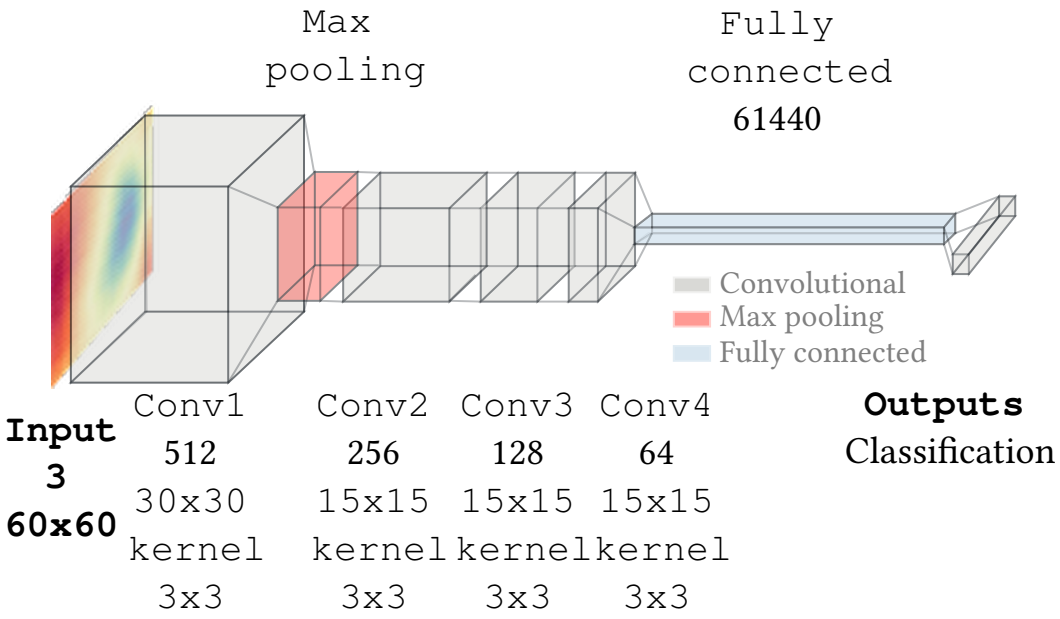


Figure 3.16: CNN model architecture composed by: (1) Input 2D image resolution 60×60×3, (2) 2D Convolution 1, 512 features, kernel size = 3, stride = 1, padding = 1 (3) RELU, (4) 2D Max poling, kernel size=2, (5) 2D Convolution 2, 256 features, kernel size = 3, stride = 1, padding = 1 (6) RELU, (7) 2D Convolution 3, 128 features, kernel size = 3, stride = 1, padding = 1 (8) RELU, (9) 2D Convolution 4, 64 features, kernel size = 3, stride = 1, padding = 1 (10) RELU, (11) Fully connected 61,440 features, (12) Number os classes 2: healthy and unhealthy,

Table 3.2: CNN Results of the experimental validation

	Accuracy	Precision	Recall	F1-score
Classification	0.88	0.90	0.88	0.87

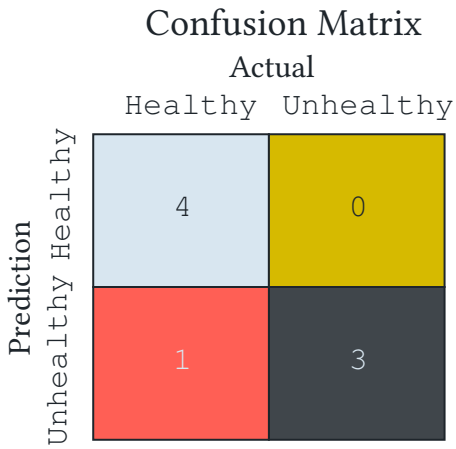


Figure 3.17: CNN Confusion matrix of the experimental validation

3.5 Future Implementation

We anticipate future work in two directions: 1. improving the scanning system and MW probe design and 2. testing the scanning technique in a more realistic setting, such as a clinical trial. This last point is a high challenge for the MW technique due to the lack of recognition in the clinical field of the comparative benefits of the MW technology in cancer detection with other techniques. However, based on experience, testing in a realistic clinical setting will be the right path to test the potential of this novel method.

We hope that a clinical trial designed for this technique, which would better fit real-world applications, will validate the potential of using MW scanning for BC detection. Such a trial would be an ideal opportunity to demonstrate the true capabilities of this scanning method. By evaluating high-quality images and collecting a substantial database from volunteers, we can effectively confirm the practicality of this innovative approach, especially when combined with AI, for detection of BC.

3.6 Conclusion

The concept of MW scanning developed in this work based its potential on the contrast between a breast without a tumor, named healthy, and a tumor, named unhealthy; and this contrast relies on the fact that the breasts of both left and right women's breasts can be considered similar. We tested this technique in two ways: 1. Electromagnetic (EM) simulation and 2. experimental

testing. Simulation using an anatomically realistic breast phantom derived from MRI demonstrates that this technique can effectively distinguish between a healthy and unhealthy breast. Unfortunately, an extensive simulation is not feasible due to the significant time required to create a decent dataset for further analysis. The experimental phase of our work enabled us to create a dataset that tests the potential of this technique, confirming our knowledge and optimistic expectations for using it to detect anomalies in women's breasts.

The principle developed in this work is to capture the energy near the object under observation. The data collected generate an image contrast that can be used to classify the condition of the breast as healthy or unhealthy. This novel concept can detect small PEC spheres of 5 mm diameter, which are smaller than the sizes documented in the survival expectation [158]. The CNN generated with an Accuracy of 88. 0%, a precision of 90. 0% and an F1 score of 87. 0%, the reported results show the potential of this technique to detect and classify small tumors.

Chapter 4

Microwave low frequency imaging in the near-field for cancer detection

4.1 Introduction

This chapter introduces a novel MS that operates at a submicrowave frequency for BC detection. The MS presented has a high miniaturization ratio, which allows to dramatically reduce the size of the unit ELC cell to 3 mm in benefit of the detection capability of this device. Although the cell can continue to be decreased by design, struggle appears when it comes to fabrication due to the space to place the surface-mount device (SMD) resistor where measurements are taken. Each cell of the MS gives rise to a voltage difference that can be measured at the back of the MS. Thus, the MS can generate an impression related to the constituents of the breast. Simulations were performed to capture and analyze a collection of images using ML methodologies. The findings of this stage of the test demonstrated the ability of the device to identify abnormalities in the breast that may or may not be cancerous.

The primary objective of this work is to utilize low-frequency EM energy to effectively differentiate between healthy and malignant breast tissue. To achieve this, it presents a novel technique for designing a MS sensor that functions in the near field and is specifically designed to detect BC. The sensor has a high miniaturization factor, as it operates at a frequency of 200 MHz and consists of tiny cells of 3 mm; each can absorb MW energy at high efficiency. The cell is placed in a 2D array of 30 by 30 cells for budget and fabrication limitations; however, the size can be easily increased. The MS detects anomalies with small radii measuring 3, 5, and 7 mm, less than the sizes documented in the survival expectation [158] and the probability of dissemination [159]. The simulation uses ARBP created from the DICOM dataset, an approach

developed especially to generate a real scenario for cancer detection and accurately evaluate the device's capacity to identify cancer under such realistic circumstances.

4.2 Theory and application methodology

We can illustrate Microwave Imaging (MI) as the image in Figure 4.1 shows when a transmitter device illuminates the breast; the microwave power travels through the breast and the receivers detect a portion of the transmitted energy. It is also possible to record the reflections by the transmitter. In this regard, when the microwave passes through the breast and encounters a tumor, it is expected that a change in the electrical properties of the material will occur. Then, the signal scatters, affecting the amount of energy the receivers and transmitter detect.

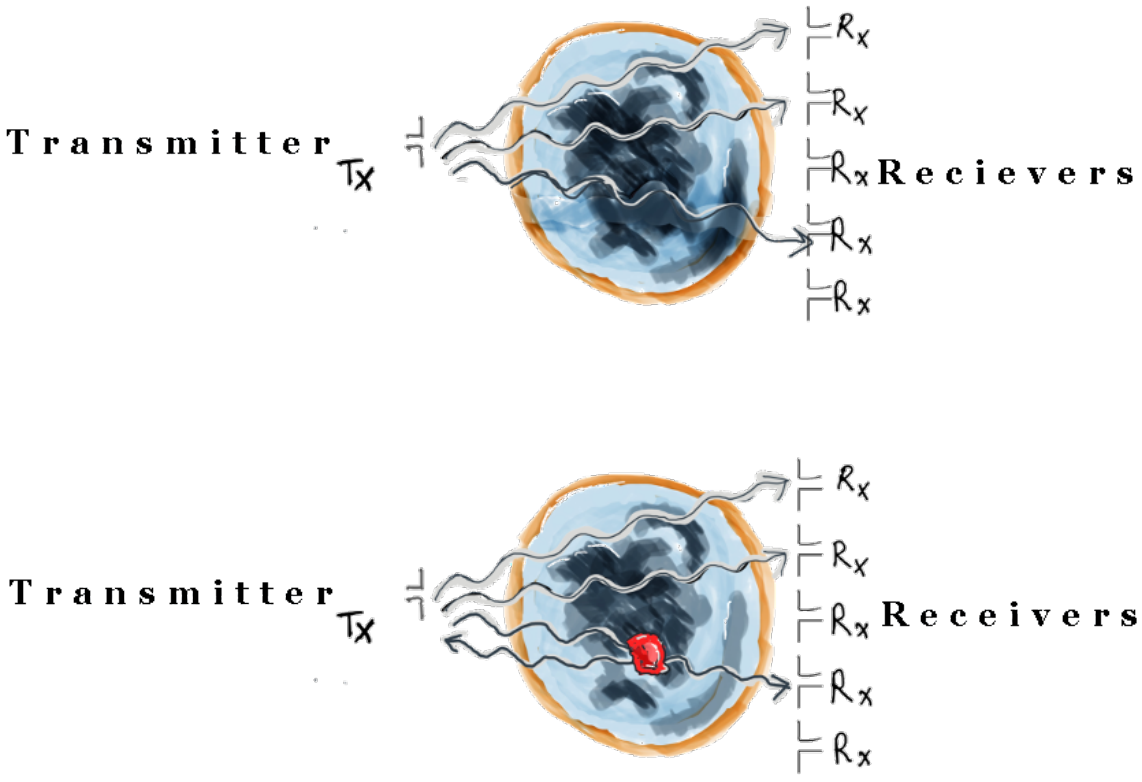


Figure 4.1: Illustrated concept of the transmitted and received MW power

When microwave power passes through breast tissue, it interacts with the material under the electrical properties of the medium. Consequently, the microwave signals that pass through the breast encode the breast components, which can be recorded to create a unique map that represents the composition of the breast. In this case, the energy recorded on the transmitter will capture the EM signature of OUT. Suppose that we introduce a perturbation in OUT, for example, a tumor with a high ϵ_r value. In that case, this will also introduce a change in the material's properties and, consequently, change the power collected by the receiver. Therefore, the contrast between these changes can reveal the presence of the anomaly in the breast, serving as a detection system with an EM sheet that maps the contrast in the dielectric composition of OUT. It is important to emphasize that this concept is based on the fact that most women have anatomically similar left and right breasts, and only a small percentage deviate from this pattern [160].

As we can maximize the collection of the MW energy in the resistors on the bottom of the MS, we can treat the UC as an EM energy absorber. Equation 3.4 is known as absorption of ELC, and is related to reflection and transmission as $R(\omega) = |S_{11}|^2$ and $T(\omega) = |S_{21}|^2$, in the case ELC, these values are calculated by software simulation CST ® [95]. Using these expressions, the respective absorption, reflection, and transmission can be calculated. It is important to emphasize that the unit cell was designed to effectively absorb the maximum possible energy by using FR-4 material. By manipulating the μ and ϵ parameters, it is possible to optimize the unit cell design in order to minimize mismatches with the surrounding medium and therefore achieve a satisfactory level of energy absorption for the application in question [103].

4.3 Numerical results

The MW sensor presented in this study is based on ELC. These cells have a specific geometric shape designed to resonate at a frequency of 200 MHz. The geometric design of the cell was chosen to be symmetric [143]. The entire design was modeled using CST ® [95], and its model and dimensions are presented in Figure 4.2. The dielectric material used as a substrate is FR-4 with $\epsilon_r = 4.3$, loss tangent $\delta = 0.025$. The UC is constructed by simulating a waveguide and employing two ports for its excitation sources. The boundary conditions are electrically and magnetically perfect conductors for the xz and yz planes in the z-direction; an open-space condition is assumed. The boundary conditions allow the incident wave to propagate in the TEM mode.

The innovative design of this MW sensor in Figure 4.2 has allowed the production of a cell with a tiny dimension of 3 mm in size with respect to the wavelength $\lambda = 1,500m$. Although the design has the potential for further size reduction, the limitation imposed by the fabrication

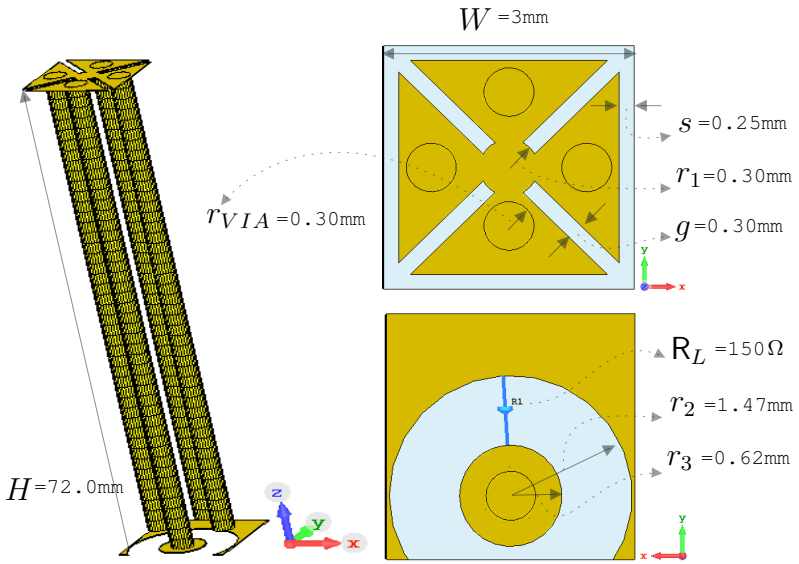


Figure 4.2: ELC UC design in CST ® software. 3D view, top and bottom layers.

process makes it challenging to achieve reduction beyond the 3 mm size. The original geometric shape of this UC is designed to resonate at a sub-microwave frequency of 200 MHz. This design is achieved using CST ® [95] software, which provides various tools to conduct EM simulations. Additionally, CST ® allows for the incorporation of voxelized phantoms, which help to create realistic scenarios, which is one of the primary goals of this work.

Figure 4.2 also shows the specific thickness of the device, which imposes certain budget constraints for its fabrication. In this context, the chosen dielectric substrate material is FR-4, a relatively low-cost material that allows us to test the capabilities of this device in an experimental phase. FR-4 is a perfect choice for fabrication purposes; this material is widely common for PCB, so in this way, the expenses associated with this project remain reasonable in light of its objectives.

Figure 4.3 illustrates the response of the ELC reflection coefficient; the respective curve shows that UC resonates at a frequency of 200 MHz, and the response produces a narrow band, which indicates the use of a similar source MW for the illumination of the system. The values of reflection, and transmission are computed by the software simulator CST ® from 100 MHz to 500 MHz, using Equation 3.4 the values of absorption are computed. These values are presented in Figure 4.4, which shows that the cell device has perfect absorption and transmission at a design frequency of 200 MHz.

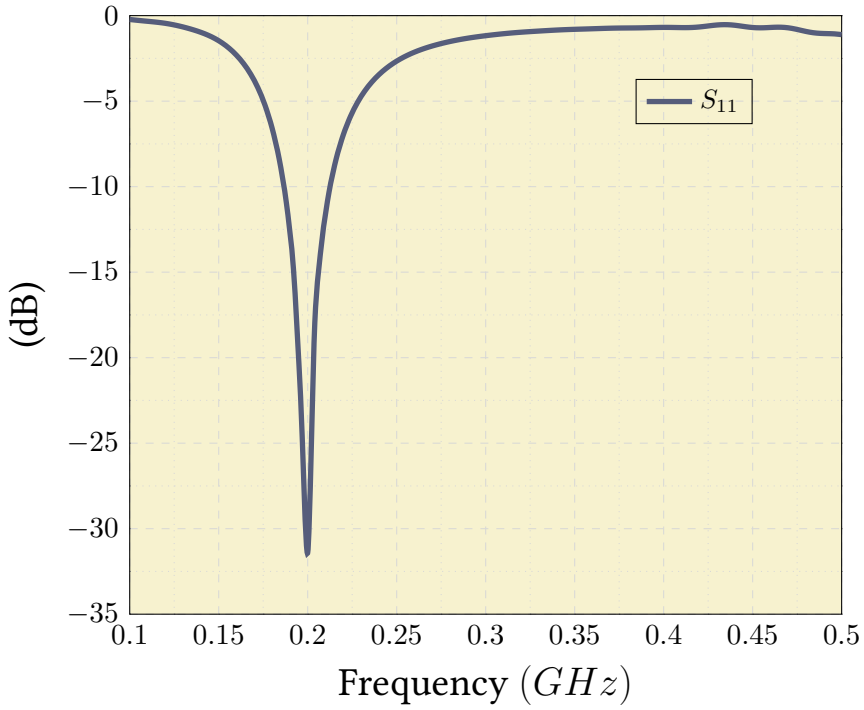


Figure 4.3: ELC UC simulation results reflection coefficient s_{11}

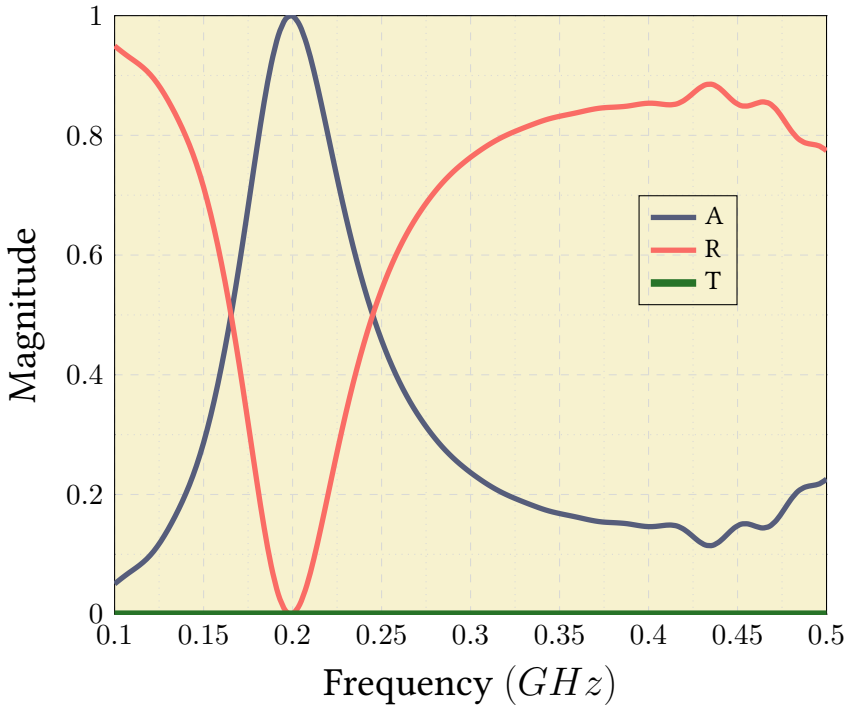


Figure 4.4: absorption, reflection, and transmission of the ELC UC. $1 - R(\omega) - T(\omega)$ where $R(\omega) = |S_{11}|^2$ and $T(\omega) = |S_{21}|^2$

The efficiency, the total power absorbed by the resistor, achieved by this design, is shown in Figure 4.5 on the left; of this graph, the efficiency is presented in Watts W; Meanwhile, on the right, the efficiency is shown as a percentage, the simulated power delivered from the source MW is 0.5 W. By manipulating the parameters relative permeability (μ_r) and ϵ_r, it is possible to optimize the design UC to minimize mismatches with the surrounding medium and therefore achieve a satisfactory level of energy absorption for the application in question [103]. Since the wavelength of these devices is far more significant than their size, the miniaturization achieved at 200 MHz depends on the values of μ_r and ϵ_r obtained by design [161] according to the expression $1/\sqrt{\epsilon_r \mu_r}$. The parameters μ_r and ϵ_r, along with the impedance of the MS, are illustrated in Figure 4.6 and Figure 4.7, respectively, showing the real and imaginary parts over the simulated frequency range of 100 MHz to 500 MHz. Figure 4.6 demonstrates that the ratio of ϵ_r to μ_r is almost equal to one, suggesting that UC is closely aligned with intrinsic impedance. In the same way, at 200 MHz, the impedance magnitude shown in Figure 4.7 is 370.2 Ω, which highlights the matching quality with the impedance of the free space.

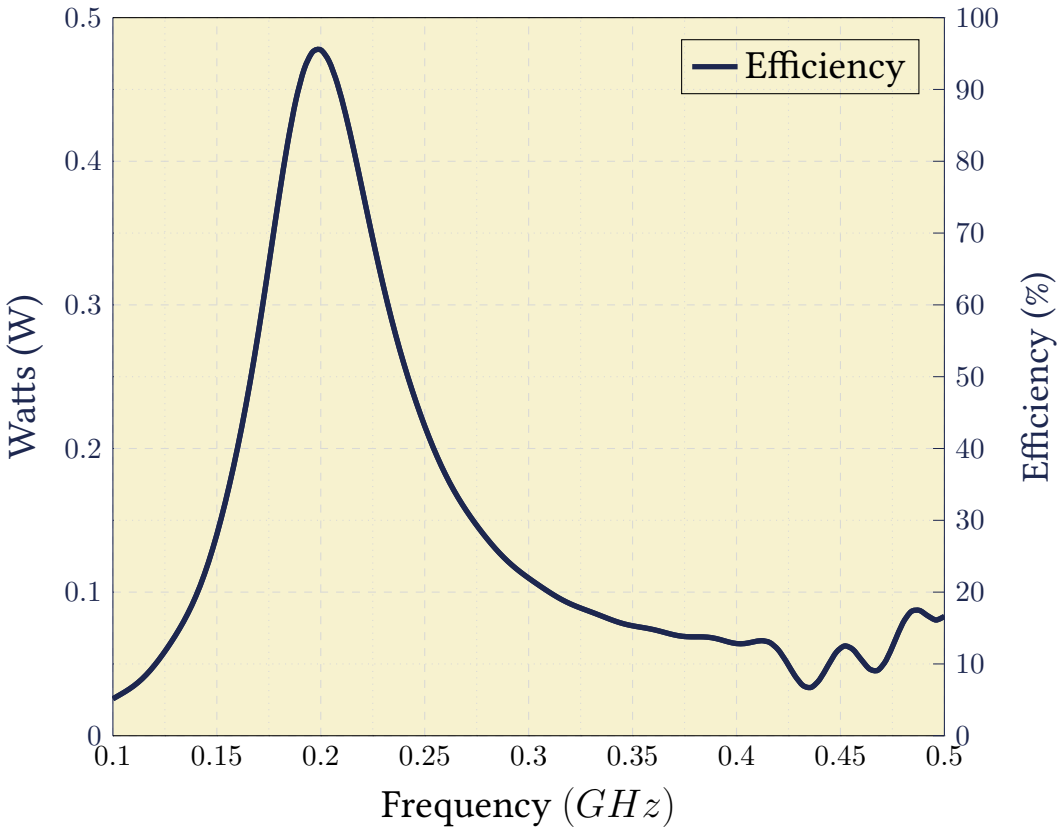


Figure 4.5: The efficiency of the ELC corresponds to the power the resistor consumes on the bottom layer. The MW power the source delivers is 0.5 W. The graph shows on the left the value in Watts and on the right in percentage %

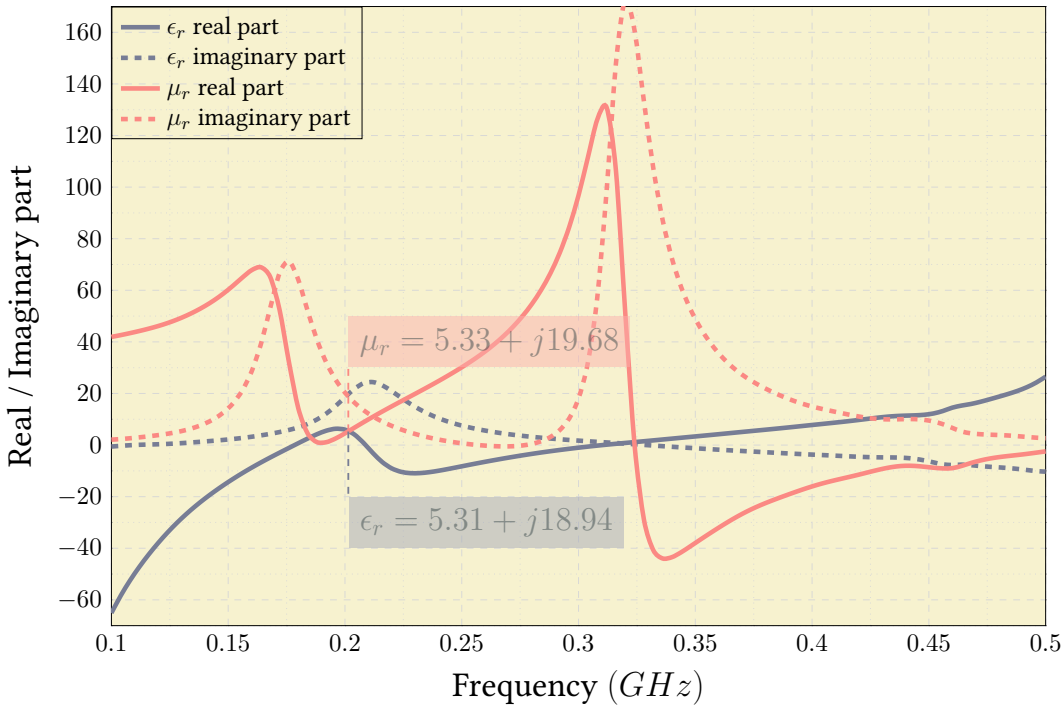


Figure 4.6: relative permittivity (ϵ_r) and relative permeability (μ_r) of the ELC cell

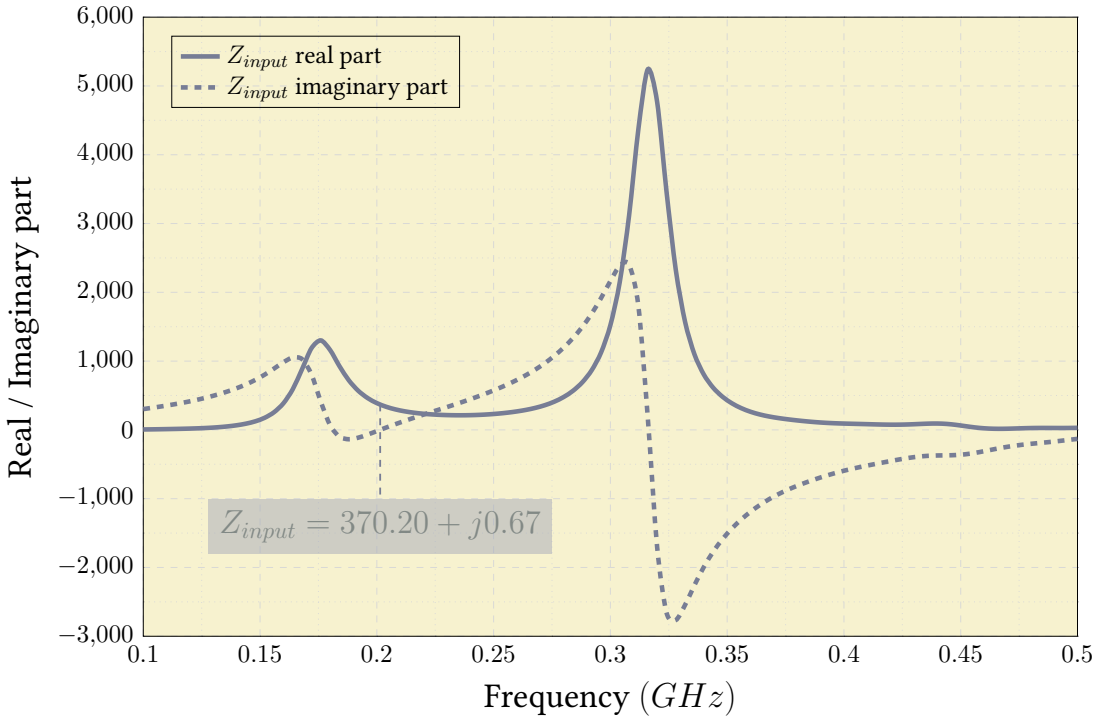


Figure 4.7: Input impedance of the ELC cell

The simulation of the power flow provides more information to understand the power dissipated on the bottom resistor of the ELC, Figure 4.8 shows the energy flows from the MW source to the MS, the image evidences the flow of the power through the MS and reaching the resistor on the bottom layer. It is important to mention that an absorber must meet two essential conditions: first, the EM wave has to penetrate the absorber deeply, and second, the entering EM wave must have high attenuation into the absorber material [162, 141] which is the case for the MS in question. The source is an electrically small loop with a resonance frequency of 200 MHz. The power is channeled through the vias from the top to the bottom layer and dissipated in the resistors. The role of the vias in the absorber, shown in Figure 4.8, is the creation of a path for the current and maximizing its flows to the resistors. The contrast image of the breast material of the technique presented in this work relies on measuring the voltages of the mentioned resistors; therefore, the power transfer becomes crucial for that purpose.

A MS comprising a 30 by 30 ELC UC has been assembled for tumor detection in EM simulations. The bottom layer of this MS contains 900 resistors that are used for voltage measurements that create an image. The top and bottom layers illustrated in Figure 4.9a and Figure 4.9b show

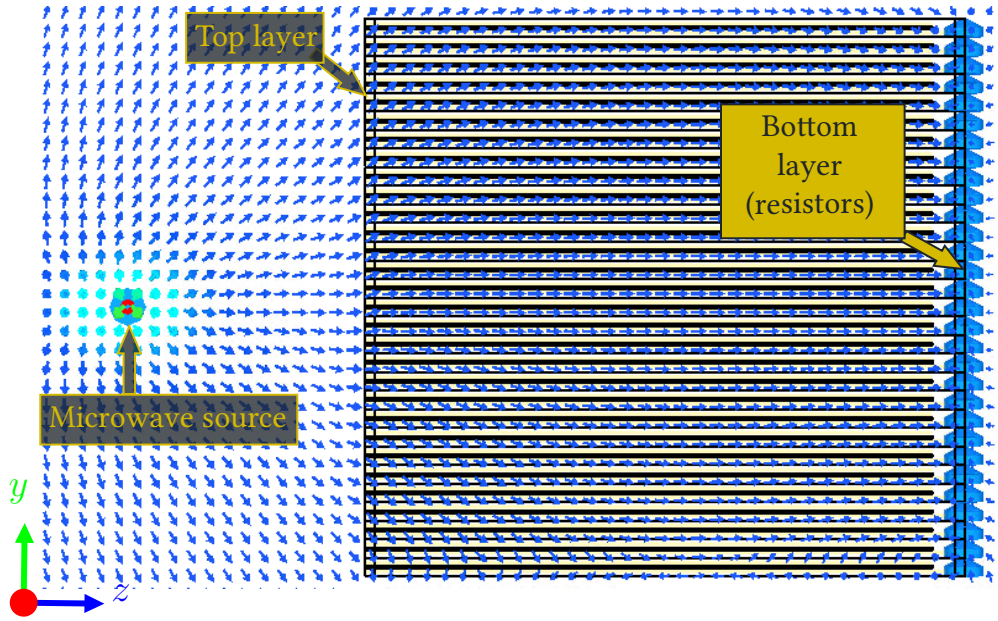
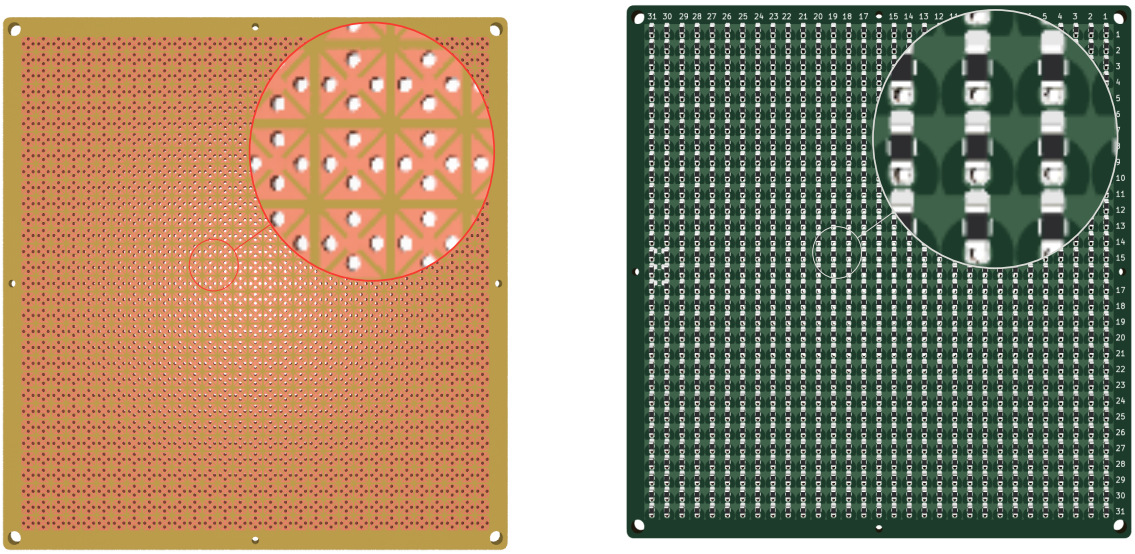


Figure 4.8: Power flow of the Metasurface (MS) of 30 by 30 ELC cell simulation in software CST ®

in detail the architecture of this MS structure. Figure 4.10a shows a 3D view of the MS, representing the whole structure; this device will be used for EM simulations to generate the images needed for tumor detection.

In this study, we conducted EM simulations using anatomically realistic breast phantom models. These models were created from two sources: (1) nine phantoms obtained from the UW, which are based on MRI images and include files for constructing the geometry and dielectric properties of breast tissue [117, 92], and (2) phantoms derived from 3D clinical breast images that are stored in DICOM files [97]. The proposed system for BC detection is based on the observation that a woman's right and left breasts are typically similar in appearance. This is supported by research, which indicates that only a small percentage of women deviate from this norm [135, 136]. Furthermore, the probability of developing BC in both breasts is very low [137, 138, 139, 140]. The complete simulation system consists of: (1) a Metasurface (MS), (2) an ARBP, and (3) a MW source, specifically an electrically small loop antenna as illustrated in Figure 4.10b. After conducting a simulation, the voltage values of the 900 resistors on the bottom layer of the MS were extracted and recorded, resulting in an image containing 30 by 30 pixels. In this setup, each pixel indicates the voltage magnitude of individual resistors at a frequency of 200 MHz.

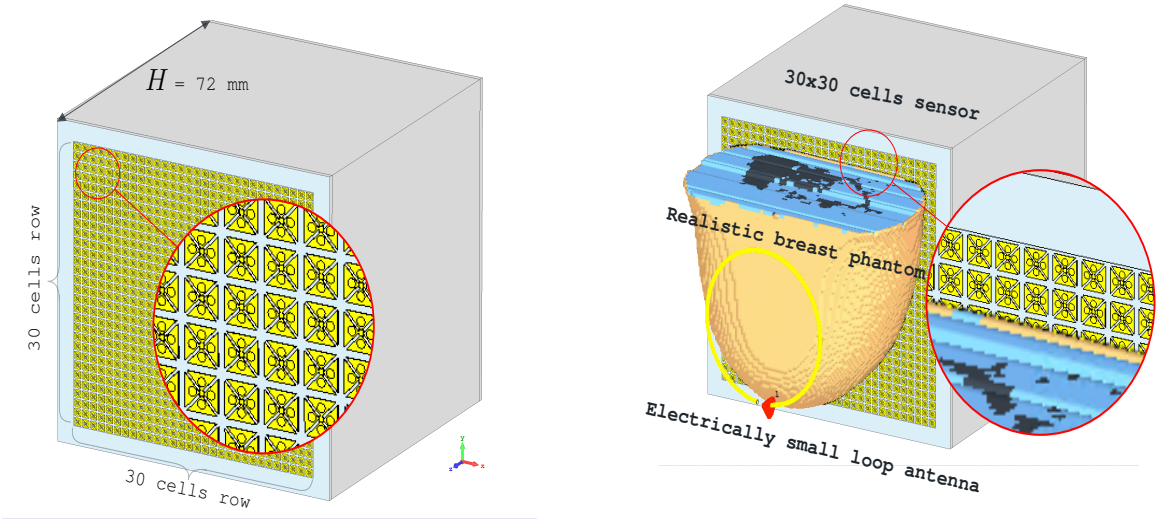


(a) (b)

Figure 4.9: MS top and bottom layers. 4.9a Top layer composed by 30x30 ELC UC of 3 mm each. 4.9b Bottom layer that holds 900 resistors in 30×30 2D array for voltage measurements

The simulations were conducted on 15 ARBP, testing both with and without a tumor, referred to as healthy and unhealthy, respectively. One unhealthy ARBP condition was simulated 12 times using three different radius: 3 mm, 5 mm, and 7 mm, these sizes are under the sizes for survival expectation and dissemination probability [158, 159]. For each tumor size, four locations within the phantom were considered, allowing us to test this technique's ability to detect tumors in various scenarios. A healthy ARBP condition was simulated once for each of the 15 phantoms considered in this experiment. A complete set of one simulation includes 3 (sizes)× 4 (locations) = 12 unhealthy ARBP and one healthy ARBP with no tumor inside. Figure 4.11 shows the tumor locations along the ARBP and the top layer of the MS; in particular, we can see the tumors located on the x-y plane in the following order: (1) center-right, (2) center-left, (3) bottom-right, and (4) bottom-left. Regarding the z-axis location, the tumors were all located 10 mm from the skin layer of the breast. The following twelve Figure 4.12, 4.13, 4.14, 4.15, 4.16, 4.17, 4.18, 4.19, 4.20, 4.21, 4.22, and 4.23 show a whole set of outcomes from the simulation on a ARBP class 3 - heterogeneously dense; we present these images as representations describing the voltages of the MS. The twelve sets of three images each include the subsequent pictures:

1. on the left ARBP without tumor designated healthy,
2. on the middle ARBP with a PEC anomaly inside designated unhealthy, and

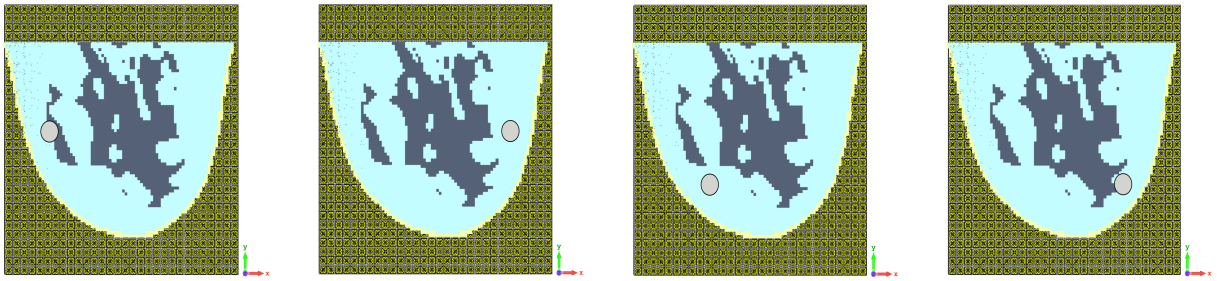


(a) (b)

Figure 4.10: MS Sensor 3D view and simulation system setup. 4.10a MS 30 by 30 cells of 3 mm size. 4.10b Representation of the CST ® simulation system with electrically small loop antenna, ARBP, and MS

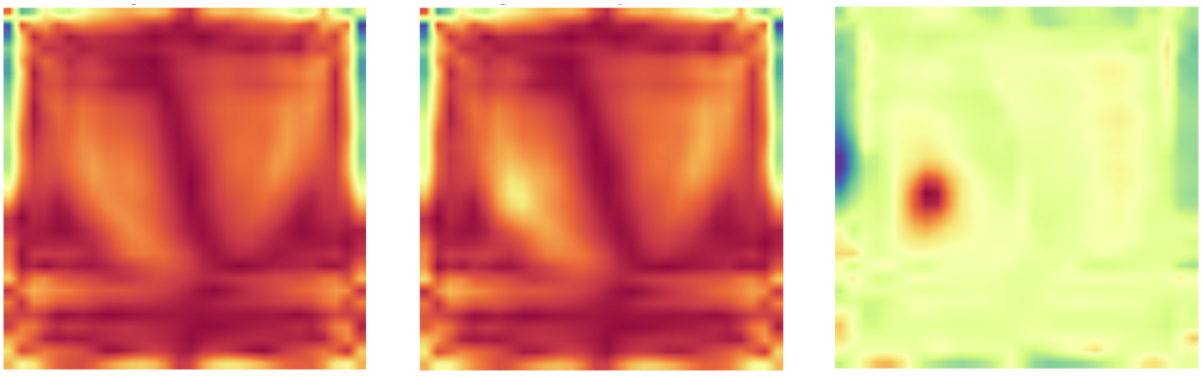
3. on the right the algebraic subtraction of the healthy and unhealthy image

Having established that, the first image on the left in the next Figures 4.12a, 4.13a, 4.14a, 4.15a, 4.16a, 4.17a, 4.18a, 4.19a, 4.20a, 4.21a, 4.22a, and 4.23a, represent the healthy condition of the ARBP class 3 heterogeneously dense. In the middle image among the twelve examples, which depicts the ARBP containing a tumor, it is noteworthy that the tumor is easily identifiable when its size radius is 7 mm, as shown in Figures 4.12b, 4.13b, and 4.14b. However, the other images labelled as 4.15b, 4.16b, 4.17b, 4.18b, 4.19b, 4.20b, 4.21b, 4.22b, and 4.23b, make it challenging to see the tumors using only the naked eye. The importance of the third image, which contains the difference between the voltage magnitudes of the healthy and unhealthy images, gains relevance in detecting the presence of an anomaly and probes the potential of this technique in detecting BC. Each of the following Figures 4.12c, 4.13c, 4.14c, 4.15c, 4.16c, 4.17c, 4.18c, 4.19c, 4.20c, 4.21c, 4.22c, and 4.23c, show circular spots that represent anomalies inside the breast.



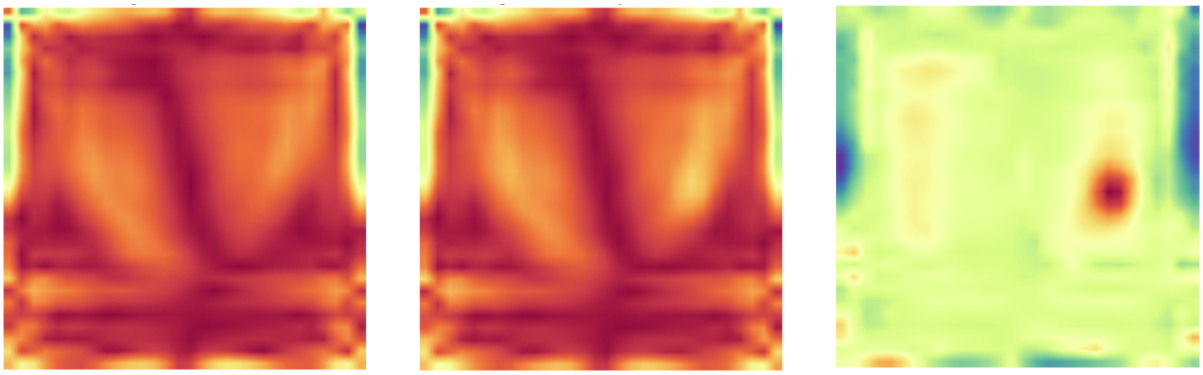
(a) (b) (c) (d)

Figure 4.11: CST ® Setup of the Simulation of ACR Class 3- Heterogeneously Dense Phantom 3 Breast ID: 062204 showing the four simulated location of the PEC tumor. 4.11a location center right, 4.11b location center left, 4.11c location bottom right, 4.11d location bottom left. The z-axis position of the tumor was set for all the simulation 10 mm from the skin of the ARBP



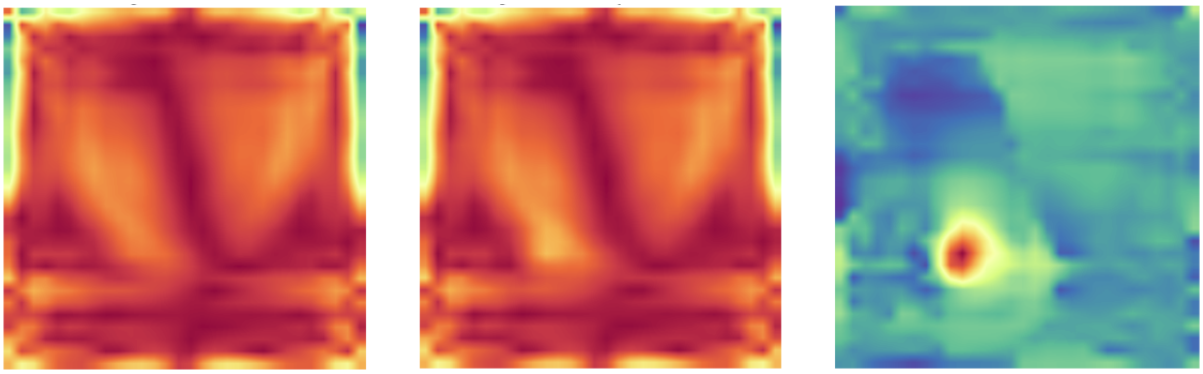
(a) (b) (c)

Figure 4.12: Plane representations of the voltage magnitudes of the 30 by 30 resistors at the bottom of the MS using CST ® Simulation of ACR Class 3- Heterogeneously Dense Phantom 3 Breast ID: 062204. 4.12a healthy. 4.12b unhealthy with 7 mm radius PEC tumor at center right. 4.12c Representation of the algebraic difference between the voltages magnitudes of the healthy 4.12a and unhealthy 4.12b



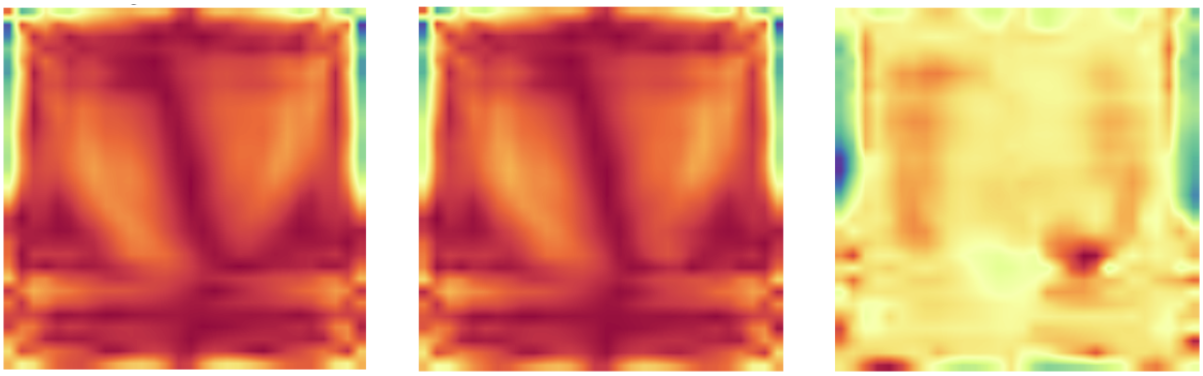
(a) (b) (c)

Figure 4.13: Plane representations of the voltage magnitudes of the 30 by 30 resistors at the bottom of the MS using CST ® Simulation of ACR Class 3- Heterogeneously Dense Phantom 3 Breast ID: 062204. 4.13a healthy. 4.13b unhealthy with 7 mm radius PEC tumor at center left. 4.13c Representation of the algebraic difference between the voltages magnitudes of the healthy 4.13a and unhealthy 4.13b



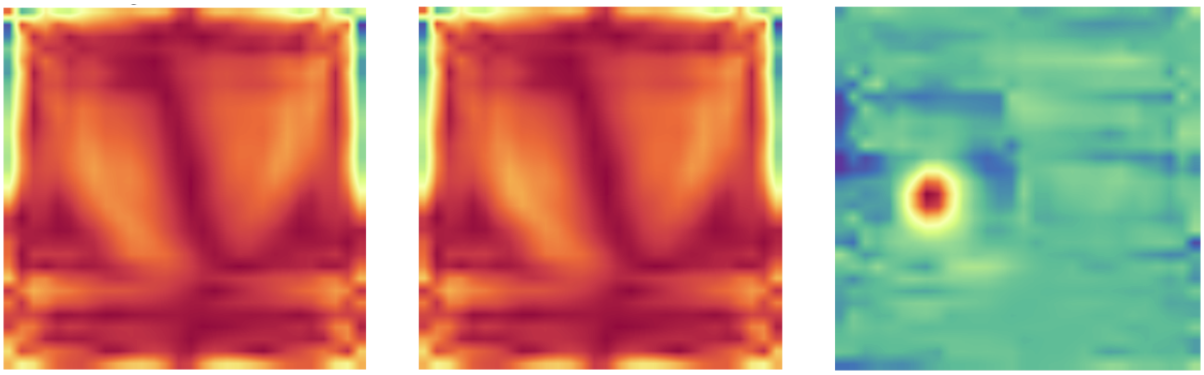
(a) (b) (c)

Figure 4.14: Plane representations of the voltage magnitudes of the 30 by 30 resistors at the bottom of the MS using CST ® Simulation of ACR Class 3- Heterogeneously Dense Phantom 3 Breast ID: 062204. 4.14a healthy. 4.14b unhealthy with 7 mm radius PEC tumor at bottom right. 4.14c Representation of the algebraic difference between the voltages magnitudes of the healthy 4.14a and unhealthy 4.14b



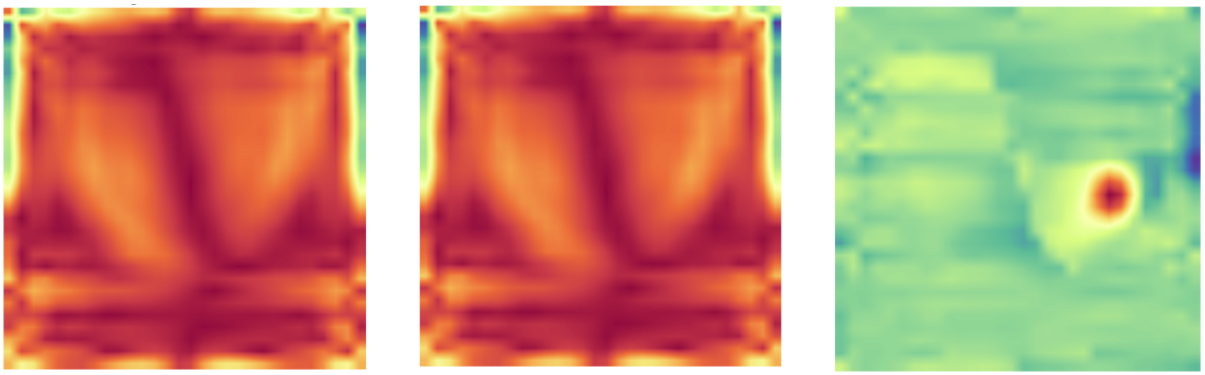
(a) (b) (c)

Figure 4.15: Plane representations of the voltage magnitudes of the 30 by 30 resistors at the bottom of the MS using CST ® Simulation of ACR Class 3- Heterogeneously Dense Phantom 3 Breast ID: 062204. 4.15a healthy. 4.15b unhealthy with 7 mm radius PEC tumor at bottom left. 4.15c Representation of the algebraic difference between the voltages magnitudes of the healthy 4.15a and unhealthy 4.15b



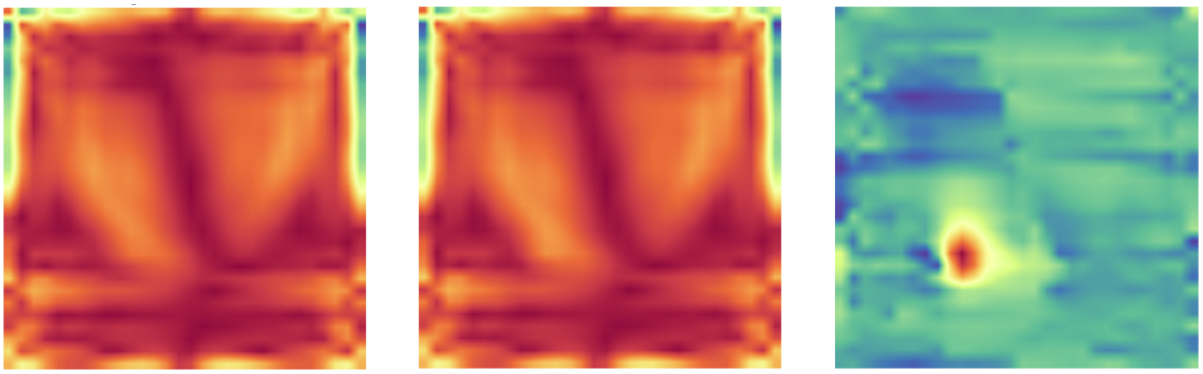
(a) (b) (c)

Figure 4.16: Plane representations of the voltage magnitudes of the 30 by 30 resistors at the bottom of the MS using CST ® Simulation of ACR Class 3- Heterogeneously Dense Phantom 3 Breast ID: 062204. 4.16a healthy. 4.16b unhealthy with 5 mm radius PEC tumor at center right. 4.16c Representation of the algebraic difference between the voltages magnitudes of the healthy 4.16a and unhealthy 4.16b



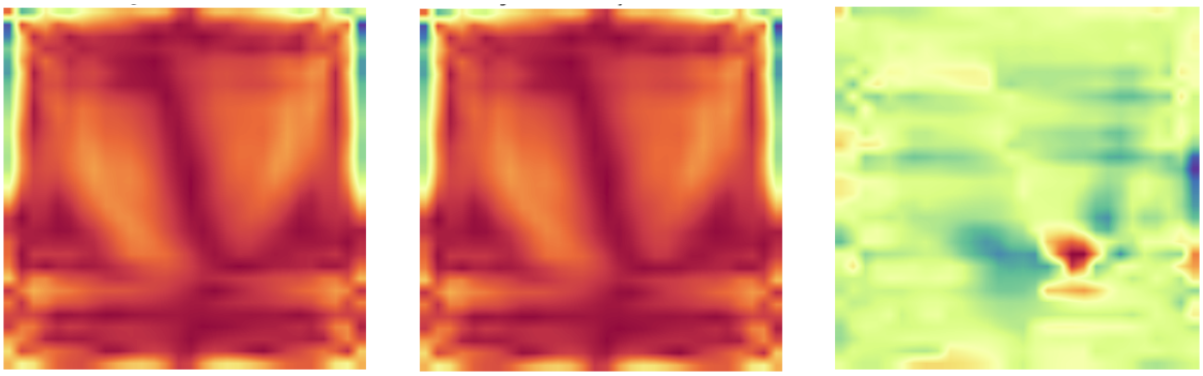
(a) (b) (c)

Figure 4.17: Plane representations of the voltage magnitudes of the 30 by 30 resistors at the bottom of the MS using CST ® Simulation of ACR Class 3- Heterogeneously Dense Phantom 3 Breast ID: 062204. 4.17a healthy. 4.17b unhealthy with 5 mm radius PEC tumor at center left. 4.17c Representation of the algebraic difference between the voltages magnitudes of the healthy 4.17a and unhealthy 4.17b



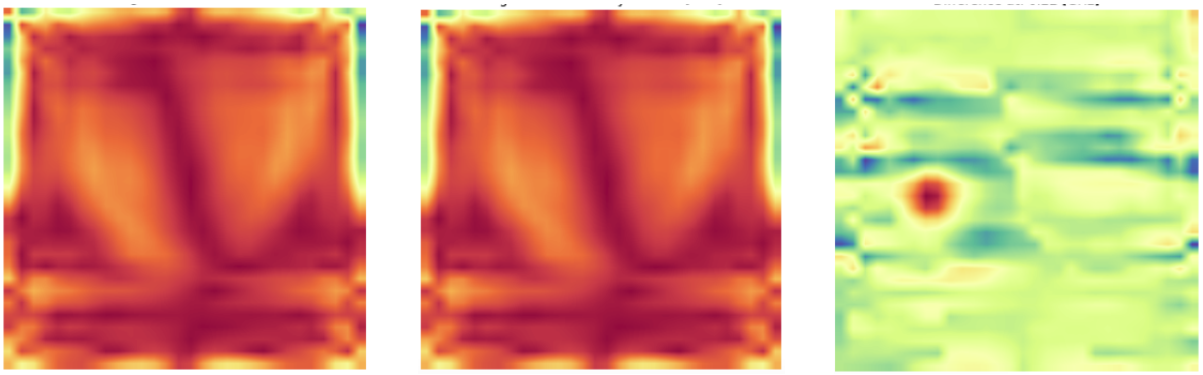
(a) (b) (c)

Figure 4.18: Plane representations of the voltage magnitudes of the 30 by 30 resistors at the bottom of the MS using CST ® Simulation of ACR Class 3- Heterogeneously Dense Phantom 3 Breast ID: 062204. 4.18a healthy. 4.18b unhealthy with 5 mm radius PEC tumor at center right. 4.18c Representation of the algebraic difference between the voltages magnitudes of the healthy 4.18a and unhealthy 4.18b



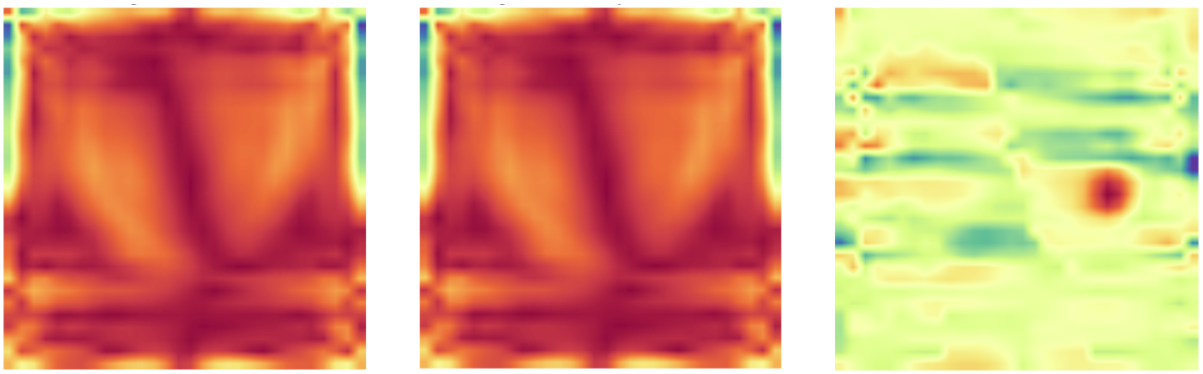
(a) (b) (c)

Figure 4.19: Plane representations of the voltage magnitudes of the 30 by 30 resistors at the bottom of the MS using CST ® Simulation of ACR Class 3- Heterogeneously Dense Phantom 3 Breast ID: 062204. 4.19a healthy. 4.19b unhealthy with 5 mm radius PEC tumor at center right. 4.19c Representation of the algebraic difference between the voltages magnitudes of the healthy 4.19a and unhealthy 4.19b



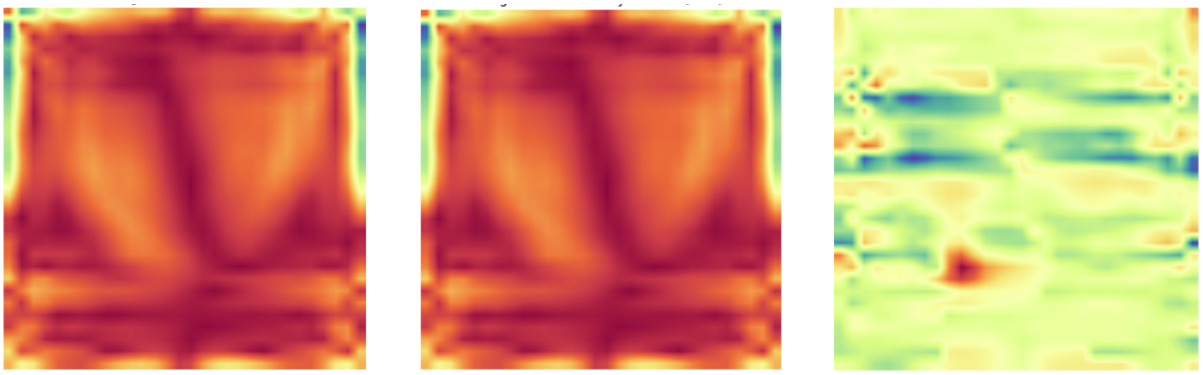
(a) (b) (c)

Figure 4.20: Plane representations of the voltage magnitudes of the 30 by 30 resistors at the bottom of the MS using CST ® Simulation of ACR Class 3- Heterogeneously Dense Phantom 3 Breast ID: 062204. 4.20a healthy. 4.20b unhealthy with 3 mm radius PEC tumor at center right. 4.20c Representation of the algebraic difference between the voltages magnitudes of the healthy 4.20a and unhealthy 4.20b



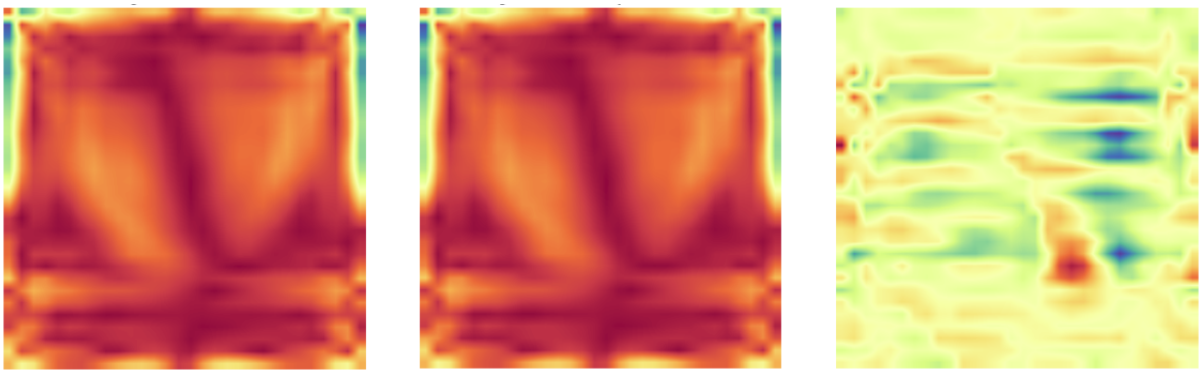
(a) (b) (c)

Figure 4.21: Plane representations of the voltage magnitudes of the 30 by 30 resistors at the bottom of the MS using CST ® Simulation of ACR Class 3- Heterogeneously Dense Phantom 3 Breast ID: 062204. 4.21a healthy. 4.21b unhealthy with 3 mm radius PEC tumor at center left. 4.21c Representation of the algebraic difference between the voltages magnitudes of the healthy 4.21a and unhealthy 4.21b



(a) (b) (c)

Figure 4.22: Plane representations of the voltage magnitudes of the 30 by 30 resistors at the bottom of the MS using CST ® Simulation of ACR Class 3- Heterogeneously Dense Phantom 3 Breast ID: 062204. 4.22a healthy. 4.22b unhealthy with 3 mm radius PEC tumor at bottom right. 4.22c Representation of the algebraic difference between the voltages magnitudes of the healthy 4.22a and unhealthy 4.22b



(a) (b) (c)

Figure 4.23: Plane representations of the voltage magnitudes of the 30 by 30 resistors at the bottom of the MS using CST ® Simulation of ACR Class 3- Heterogeneously Dense Phantom 3 Breast ID: 062204. 4.23a healthy. 4.23b unhealthy with 3 mm radius PEC tumor at bottom right. 4.23c Representation of the algebraic difference between the voltages magnitudes of the healthy 4.23a and unhealthy 4.23b

4.4 Application of the Convolutional Neural Network

The implementation of AI in the analysis of biomedical images has significantly improved anomaly detection. This advancement can be particularly beneficial for detecting BC using AI techniques. The realistic scenarios presented in this work highlight the challenges of identifying tumors within the breast tissue. However, with the aid of AI, we can enhance the classification process for:

1. healthy and unhealthy breast classification
2. tumor location identification, and
3. tumor size category

This study implemented a CNN system for classifying the detection of BC. The effectiveness of this method was discussed in Section 1.3. This technique was implemented in 15 dense ARBP as described in Subsection 1.4. These ARBP comprised three fundamental tissue layers:

1. skin,
2. fibro-glandular, and
3. fat layers

The first input of CNN is two sets of 15 images each, labeled healthy and unhealthy; this task will determine the presence or absence of a tumor inside the breast. The second task for the designed CNN is to obtain the tumor location from the 180 unhealthy images that were evenly divided and labeled location1, location2, location3 and location4 to be processed. Similarly, the tumor size is acquired from the data set that, in this case, is divided into groups of 60 images labeled size1, size2, and size3.

Since the format of data collected from EM simulation comes in voltage magnitude values, we arranged them into a 2D matrix of 30 by 30 and translated them into an image of RGB using Python [151, 152, 153, 154, 155, 156, 157]. These images are the input of the CNN illustrated in Figure 4.24 composed from left to right: (1) the input image in RGB format with 30 x 30 pixels, (2) one 2D convolutional block, (3) followed by a max-pooling block that reduces the image size, (4) the CNN architecture continues with three additional 2D convolutional blocks and (5) a fully connected block. Four activation blocks RELU are included, with the stride and padding values set to 1.

One challenge in using ARBP for EM simulations in this work was the high demand for computational resources, which extended the simulation time required to obtain the voltage magnitudes necessary to create a single image. As a result of this lengthy simulation process for image generation, the dataset used to train CNN is moderate in size. With the purpose of running the CNN model, the data set was divided into 70% for training and 30% for testing; the training data set allows the model to learn classification between the defined results. On the other hand, the portion of the data set used for the testing will help to evaluate the power of the CNN model to perform the classification work.

After training the CNN model and evaluating its performance, the ability to discern between healthy and unhealthy on the complete test data set is 83%. The ability to classify the unhealthy condition on all cancerous tissue in the test data set is 88%, and the recall that measures the correctly predicted quantity as unhealthy is 83%. Table 4.1 contains these results and the results in classifying location and size. In determining the location of the tumor within the ARBP, the CNN model exhibits 62% in Accuracy and 72% in precision. There is a decrease in Accuracy when determining tumor size due to the relatively small dataset; increasing the dataset is expected to improve Accuracy in tumor size classification.

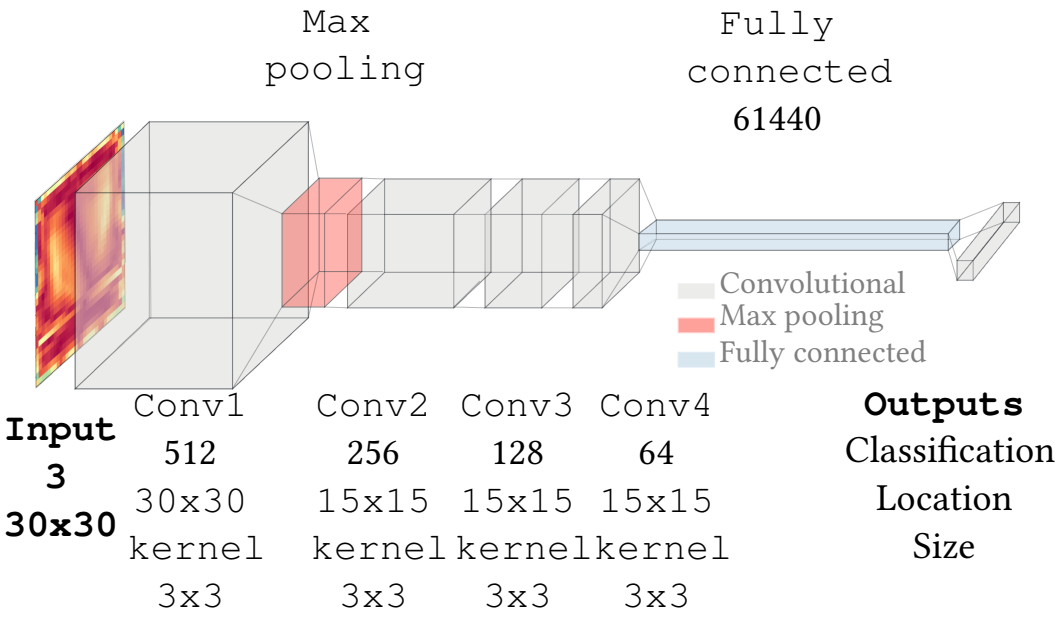


Figure 4.24: illustration of the CNN indicating Convoluiton layers (CL), Pooling layers (PL), filters, and Fully connected layers (FCL)

Table 4.1: Results of the CNN

	Accuracy	Precision	Recall	F1-score
Classification	0.83	0.88	0.83	0.83
Location	0.62	0.71	0.62	0.64
Size	0.50	0.61	0.50	0.52

4.5 Experimental verification

This section describes the experimental setup designed to evaluate the performance of the fabricated MS. The system developed for experimental verification includes several devices to achieve a complete set of measurements. In this experiment, we used a dipole antenna that is $\lambda/10$ wavelengths long powered by a MW amplifier. The amplifier increases the power to 0.5 W after the signal generator provides a sinusoidal signal at a frequency of 200 MHz. Between the electrically small dipole and the MS placed OUT, in this case, we used a piece of meat that has a ϵ_r around 50 to 70 [163, 164].

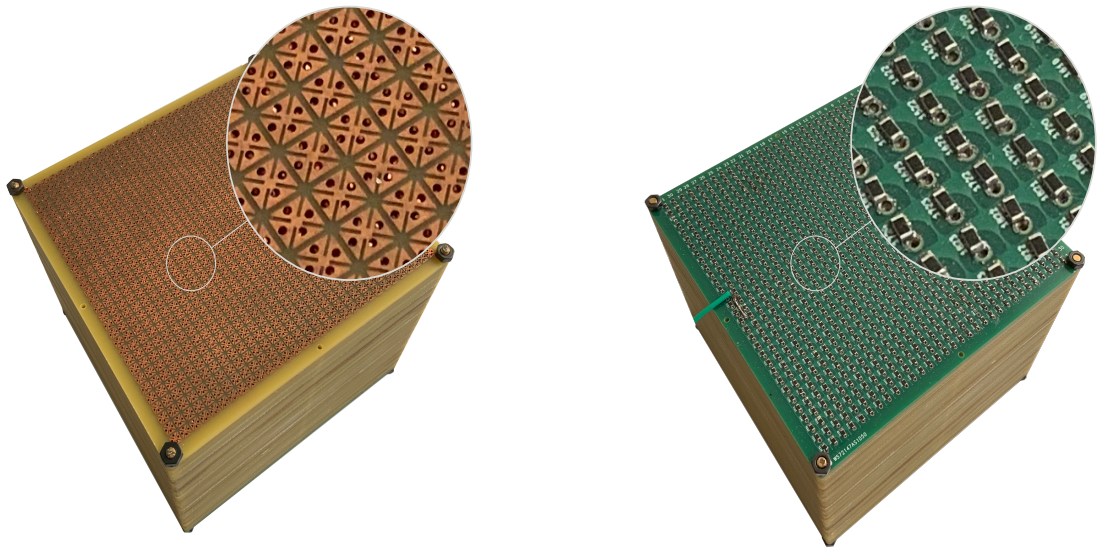
Throughout the entire experimental stage, the dipole antenna and the MS are positioned 5 mm away from the meat. Figure 4.25 illustrates the structure of the MS, displaying both the top and bottom layers. It is important to emphasize the challenge of manually welding the 900 resistors in a tiny spot on the bottom layer; this was necessary to maintain the low cost of the fabricated MS. The setup of the experiment is shown in Figure 4.26; this picture illustrates the entire set of devices needed to complete the voltage measurements on the bottom layer of the MS. In more detail, the system encompasses the following devices and instruments:

1. Siglent Technologies SDS1202X-E 200 MHz Digital Oscilloscope 2 Channels
2. MAX2870 Signal source High stability Low Noise Frequency Generator Module
3. Shnitpwr 3V to 24VDC 72W Power Supply Adjustable
4. Power Amplifier 10 to 1000 MHz Medium Power 30 dBm ZHL-2-8-S+
5. Isolator 200 MHz
6. Metasurface (MS) of 30×30 UC ELC
7. Electrically small dipole lengh $\lambda/10$
8. Meat ϵ_r 50-70 [163, 164].

The electrically small dipole illuminated the meat, and the power transmitted received by the top layer of the MS raises currents on the UC geometry; the vias transport these small currents to the bottom layer of the MS where the resistors hold, each of this resistor generates a voltage, at that point, we measured the voltages of the whole 900 array resistors. We measured each of the 900 resistors one by one using a proper probe at a frequency of 200 MHz; after establishing a set of voltages, we recorded the magnitudes in a spreadsheet for further analysis. The entire measurement process needed to be performed at least twice:

1. Measurements with OUT without PEC sphere,
2. Measurements with OUT with PEC sphere of 10 mm diameter inside

This process ensured that the required data was collected to create images with and without the tumor using the Python programming language.



(a) (b)

Figure 4.25: Fabricated Metasurface (MS). 4.25a MS top layer and 3D view of the 30×30 UC ELC 3 mm size. 4.25b MS bottom holding 30×30 resistors for amplitude voltage measurements

Due to the significant amount of time involved in manually measuring voltage magnitudes, the sensor was encased in a frame that serves two purposes: (1) It protects the sensor during the measurement process, (2) It holds the sensor in a fixed position throughout the entire measurement procedure. The antenna provided continuous illumination to the system throughout

the measurement process. The results of this process are shown in Figure 4.27; specifically, Figure 4.27a illustrates the voltage magnitudes of the meat without the PEC sphere. Figure 4.27b shows an image of the meat with a 10 mm diameter PEC sphere placed inside. Interestingly, the presence of the anomaly is not easily noticeable to the naked eye in this image. However, we can reveal the anomaly more clearly by performing algebraic subtraction between the images taken with and without the PEC sphere.

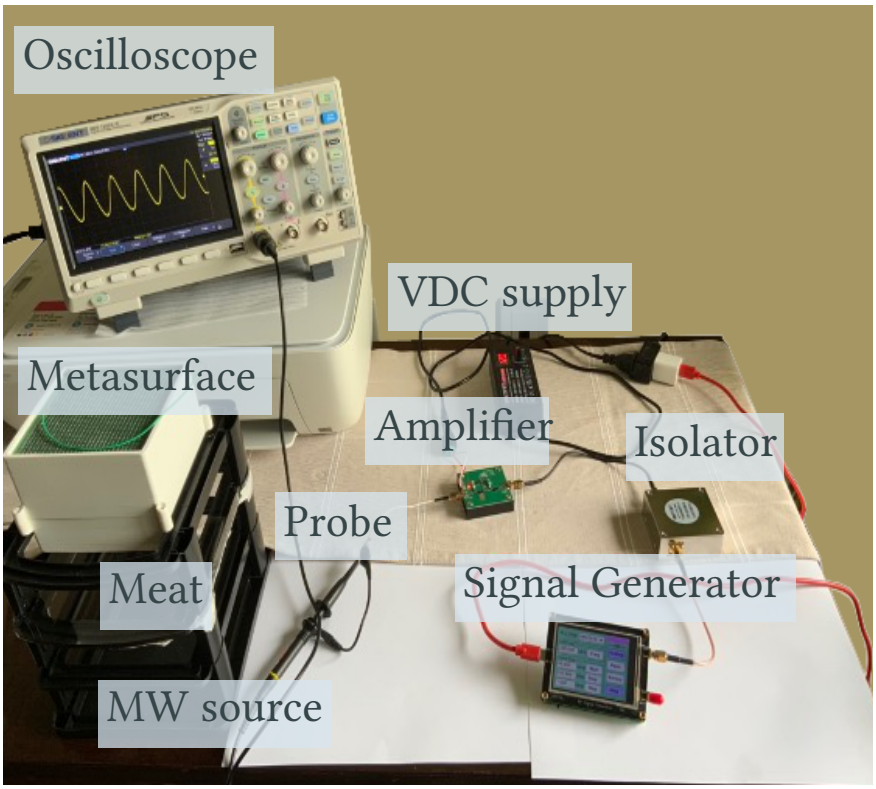
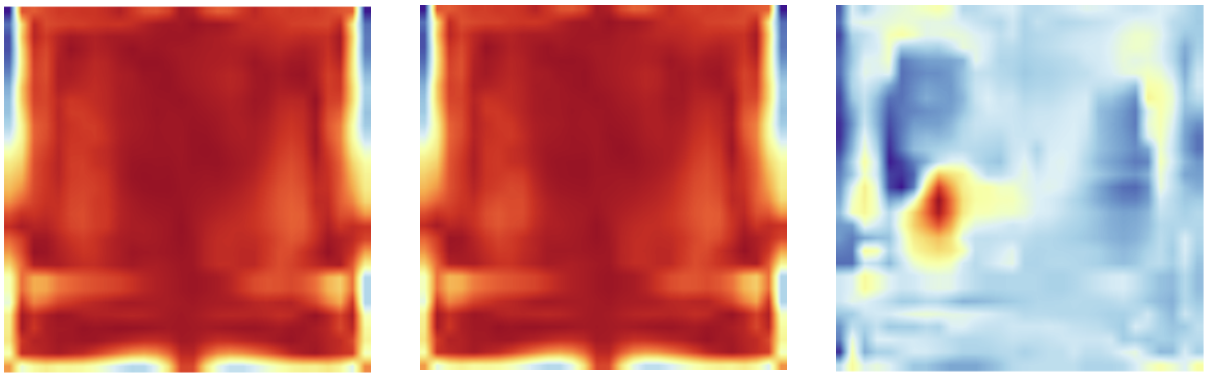


Figure 4.26: Experimental setup devices: 1. Oscilloscope, 2. Signal generator, 3. MW amplifier, 4. isolator, 5. VDC power supply, 6. Electrically small dipole lenght $\lambda/10$, and 7. Metasurface (MS) 30 by 30 UC ELC



(a) (b) (c)

Figure 4.27: Experiment result using the fabricated MS of 30 by 30 UC ELC. 4.27a Original image without PEC sphere. 4.27b Image with a PEC sphere of 10 mm diameter inside. 4.27c Image with the algebraic difference between the voltage magnitudes of images 4.27a and 4.27b

4.6 Conclusion

This study presents a novel MS sensor that uses a 30x30 (3 mm) cell grid that operates at 200 MHz to detect BC tumors. The sensor can identify tumors with a resolution of 3 mm in radius. The MS absorbs energy transmitted from the MW source, passing through the OUT. The MW energy penetrates deeply into the MS structure and is channeled through the vias to the resistor located in the bottom layer. The voltages measured across the resistors are used to create an image that maps the constituents of the OUT. This technique allows for the detection of perturbations in material properties; in some cases, these anomalies are easily identifiable; however, in other instances, the algebraic subtraction of the healthy and unhealthy images reveals the presence of an anomaly. With the help of AI, the system improved the detection modality not only in the case of classified healthy or unhealthy, but also in identifying the size and location of the anomaly. The EM simulations were conducted in a realistic scenario, as the ARBP used for this purpose was derived from anatomically realistic breast models created from the images of MRI. In this work, we specifically utilized compressed versions of the phantoms. To achieve this, we simulated the physical compression of these phantoms using Finite Element Analysis (FEA) software. The combination of these elements makes this work unique, including a microwave system for BC detection under a realistically simulated scenario. The classification Accuracy to distinguish between healthy and unhealthy breasts achieved a rate of 83%. Although the system achieved an Accuracy of 62% in classifying the location of the tumor and 50% in determining its size, these results are attributed to the limited size of the data set. Increasing the simulation and obtaining more samples would consequently improve the Accuracy of these values.

Although several challenges arose in designing, particularly in fabricating the MS, the experimental trial of this technique became achievable. This phase confirmed, in some grades, the results obtained in the simulation phase, which generated a positive impact on the potential of this technique in the field of detection of BC. From the start to the end, this technique maintained safe and low-cost development that probes the incommensurable application of the MW technique in the biomedical field.

Chapter 5

Breast cancer detection using a microwave probe and self-organized algorithm

5.1 Introduction

This chapter proposes a low-frequency MW probe combined with Artificial Life (AL) self-organized algorithm for Celular automata (CA) in conjunction with Genetic Algorithm (GA) to classify and detect BC. The related concept involved in this technique trusts the backscatter signal recorded by the MW probe. We expect that the probe will successfully detect changes in dielectric properties in breast tissue material; for example, the measurement of the magnitude of the reflection coefficient will change when OUT is measured with and without a material perturbation. This phenomenon allows us to use these changes in the response of the MW probe to build the anomaly classification and refine it by implementing computational assistance. The detection system operates under the assumption that both women's breasts exhibit similar shapes and compositions, with a low likelihood of tumor development in both breasts simultaneously.

The first part of this work deals with the design of a miniaturized probe; the second part deals with the method of building the self-organized 2D CA algorithm for binary classification; the next part is the creation of a simulation environment using EM software; and finally, an experimental stage is run to corroborate the performance of this system. The proposed system consists of three major components: (1) sensing using the MW probe, (2) the self-organized 2D CA classifier, and (3) the detection of anomalies. Figure 5.1 illustrates the three stages and the

flow of data. After collecting data with the MW probe, the system utilized a GA to identify the optimal rule for the CA classifier. Subsequently, the system effectively distinguished between healthy and unhealthy samples.

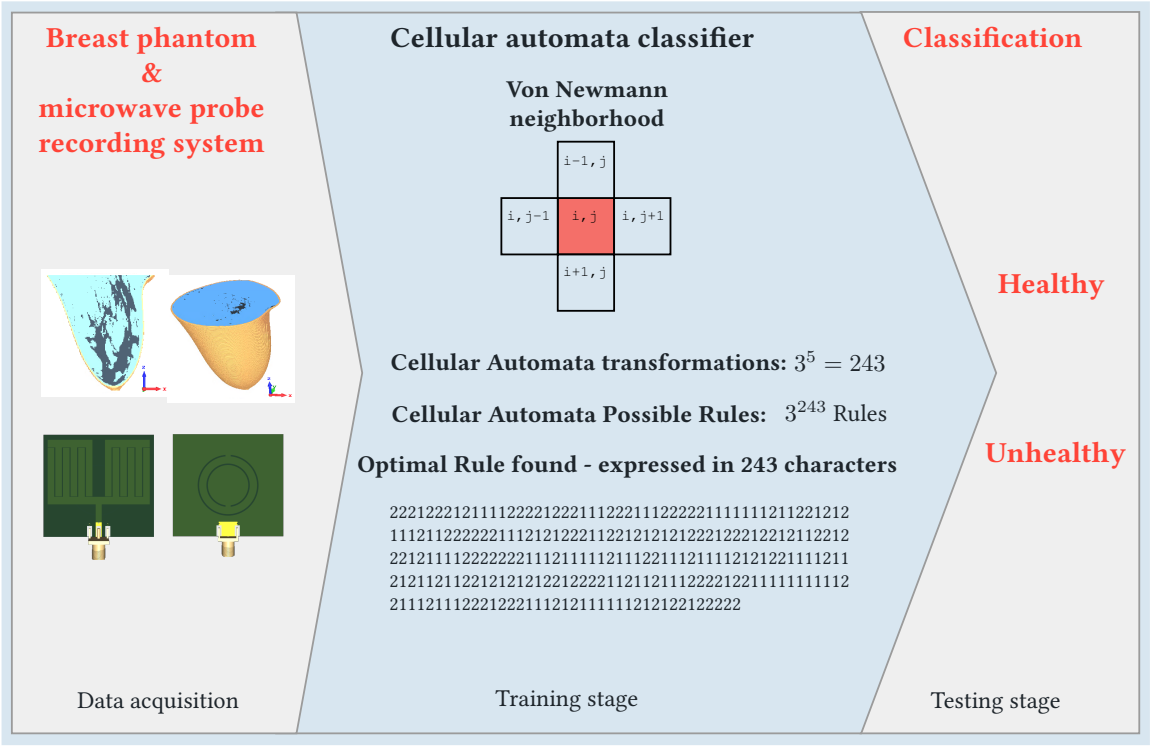


Figure 5.1: Block diagram of the proposed system integrating three major components: 1. sensing using the MW probe, 2. the CA classifier, 3. and the detection of anomalies.

5.2 Theory and application methodology

The underlying principle of this concept is that when an antenna illuminates an object, the reflected EM wave indicates the degree of mismatch with the surrounding medium. Since the reflection coefficient relates the amplitude of the reflected wave to the transmitted wave, a modification in the medium will change this relationship; the following Figure 5.2 illustrates this property: When an obstacle interacts with EM radiation from an antenna, the relationship between the magnitudes of the reflected and transmitted waves will change. The reflection coefficient will modify accordingly if a perturbation occurs inside the obstacle. Assume that we

record all the changes in the reflection coefficient using a device suitable for making this work. Now, with the assistance of computational aids such as AI, the system will be able to determine instances where the obstacle has or has no anomalies inside, and correspondingly, this becomes the root of our detection system.

This work proposes to undertake the challenge of studying the use of self-organized 2D CA in classification problems. The self-organized 2D CA is a spatial grid composed of cells, where each cell is updated according to the status of its neighborhood and using a transition function based on predetermined local rules. CA is a representation of the physical reality where time and space exist as discrete expressions. It is usually represented by an infinite space or a dimensional array that holds cells with a certain discrete status at a certain discrete time.[165]. To accomplish this purpose, this work will develop a computational code to test at least two rules, one of which is selected from the literature review and the other obtained using GA. In order to test the performance of the developed CA classifier, it is estimated that it is compared to the ML techniques used in tumor cancer detection.

The primary objective of this research is to evaluate the self-organized CA binary classifier developed in this study using data obtained from an EM simulation and experimental validation. For EM simulation, we will use realistic anatomically breast phantoms, and for the experimental stage, we will use breast phantoms fabricated with TRITON X-100. Both systems, simulated and experimental, will be illuminated by a dipole antenna with a resonance frequency of 640 MHz.

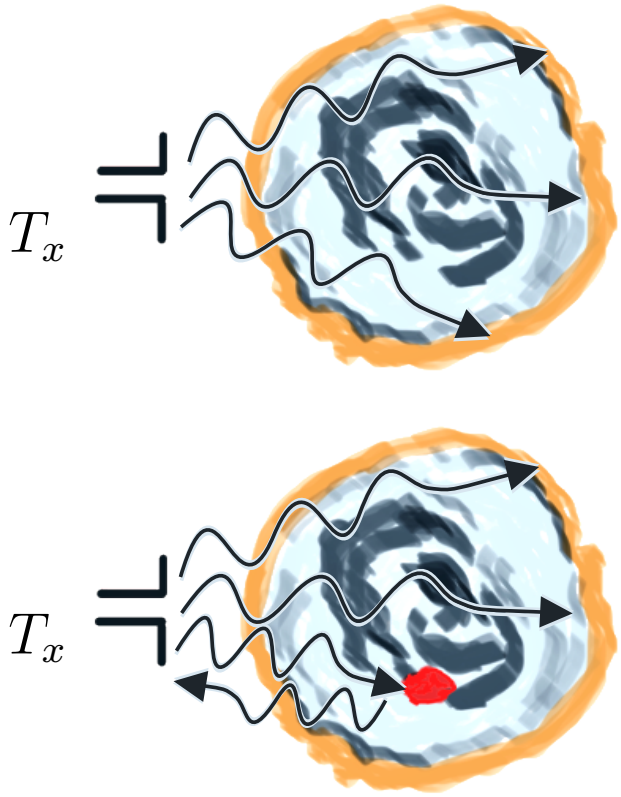


Figure 5.2: Concept of detection using reflection coefficient

5.3 Probe design

The concept that governs the miniaturization antenna approach relies on manipulating the material's refractive index to decrease the velocity of the EM wave. The reduction in the size of the electrical antenna is a consequence of the reduction in the propagation of the wavelength, which is triggered by the reduction in the velocity of the wave [161]. Several techniques have been developed to reduce the size of microwave antennas, such as manipulating the shape of the antenna, using lumped elements, and using metamaterial cells. In previous chapters, we have used metamaterials as a powerful and effective approach to reducing the electrical size of microwave devices; we can take advantage of this previous work by using metamaterial to

develop a sensitivity probe antenna. The reduction in antenna size can be approximately represented by the expression $1/\sqrt{\epsilon_r \mu_r}$, where ϵ_r and μ_r represent the material and can be used to reduce antenna size. Although the reduction in antenna size conveys a decrease in performance [166], in this work the antenna is pretended to be used to detect the disturbance in the electrical field due to a change in the electrical material constitution; therefore, the sensibility of the antenna is the main objective in this study.

The breast tumor detection system measures the backscattered reflection coefficient, while the antenna illuminates the breast [167]. This antenna, which works in the sensing mode, is the more relevant part of this technique that relies on the antenna's ability to detect small changes in the breast tissue material.

The sensor presented in this chapter is rectangular, with interfinger capacitors on the top layer and two rings on the bottom layer. The substrate used is an FR-4 with a thickness of 1.6 mm, which is widely available among PCB companies; therefore, its fabrication is straightforward and low cost. Figure 5.3 shows the reflection coefficient of each design illustrated in Figures 5.4a,5.4b, 5.4c, 5.4d, 5.5a, 5.5b, 5.5c, and 5.5d, in the process of miniaturization of the antenna. The initial design has a square bottom layer measuring 49 mm $\times$ 53 mm, while the top layer is a rectangle measuring 31 mm $\times$ 49.3 mm. The reflection coefficient, shown by the pink dotted line in Figure 5.3, resonates at a frequency of 2.2 GHz. In the second simulation, we extracted a rectangular piece on the top layer of 27.5 mm $\times$ 6 mm Figure 5.4c, showing no changes in the frequency of resonance; this is shown in blue color in Figure 5.3. In the next step of miniaturization, we integrated an Interdigital Ccapacitor (IDC) with a finger thickness of 3.19 mm, a finger length of 24.31 mm, and a finger separation of 0.5 mm, as shown in Figure 5.5a. The introduction of the IDC reduced the resonance frequency to 1.1 GHz. So far, there have been no changes in the bottom layer of the antenna design. We extracted two split rings from the ground plate, as shown in Figure 5.5d. This adjustment decreased the resonance frequency to 0.64 GHz, illustrated in green in Figure 5.3. We can also see in black in this graphic the S_{11} of the fabricated antenna that results in the resonance frequency desired for this device. Figure 5.6 displays the top and bottom layers of the fabricated probe.

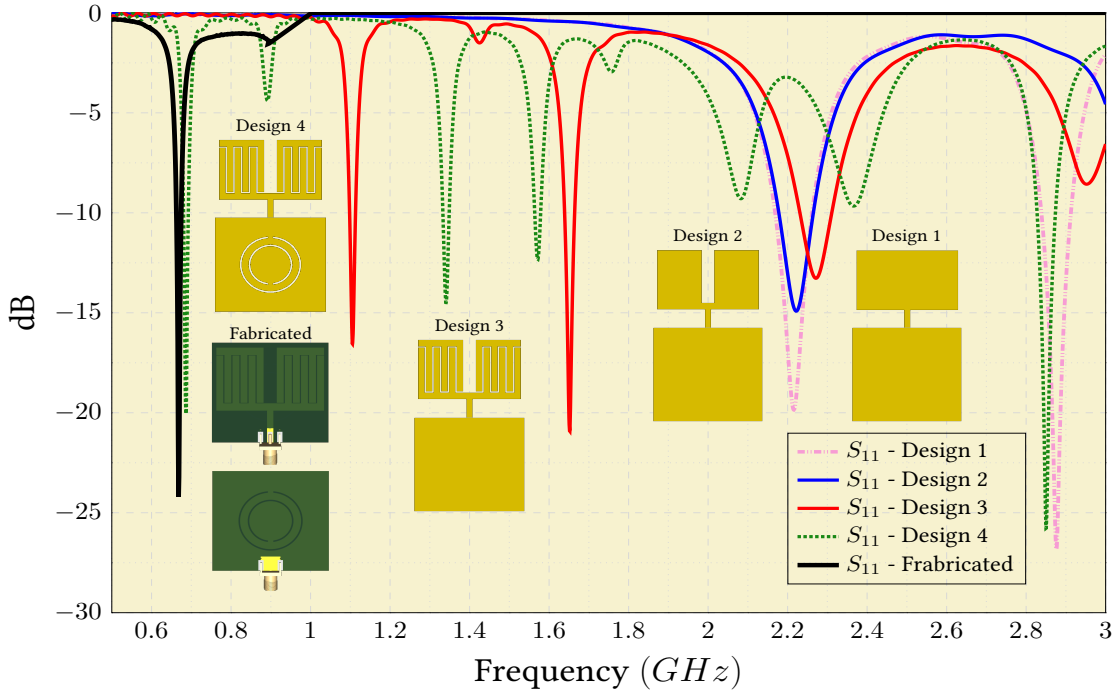


Figure 5.3: Reflection coefficients S_{11} of the simulated designs, and fabricated MW probe.

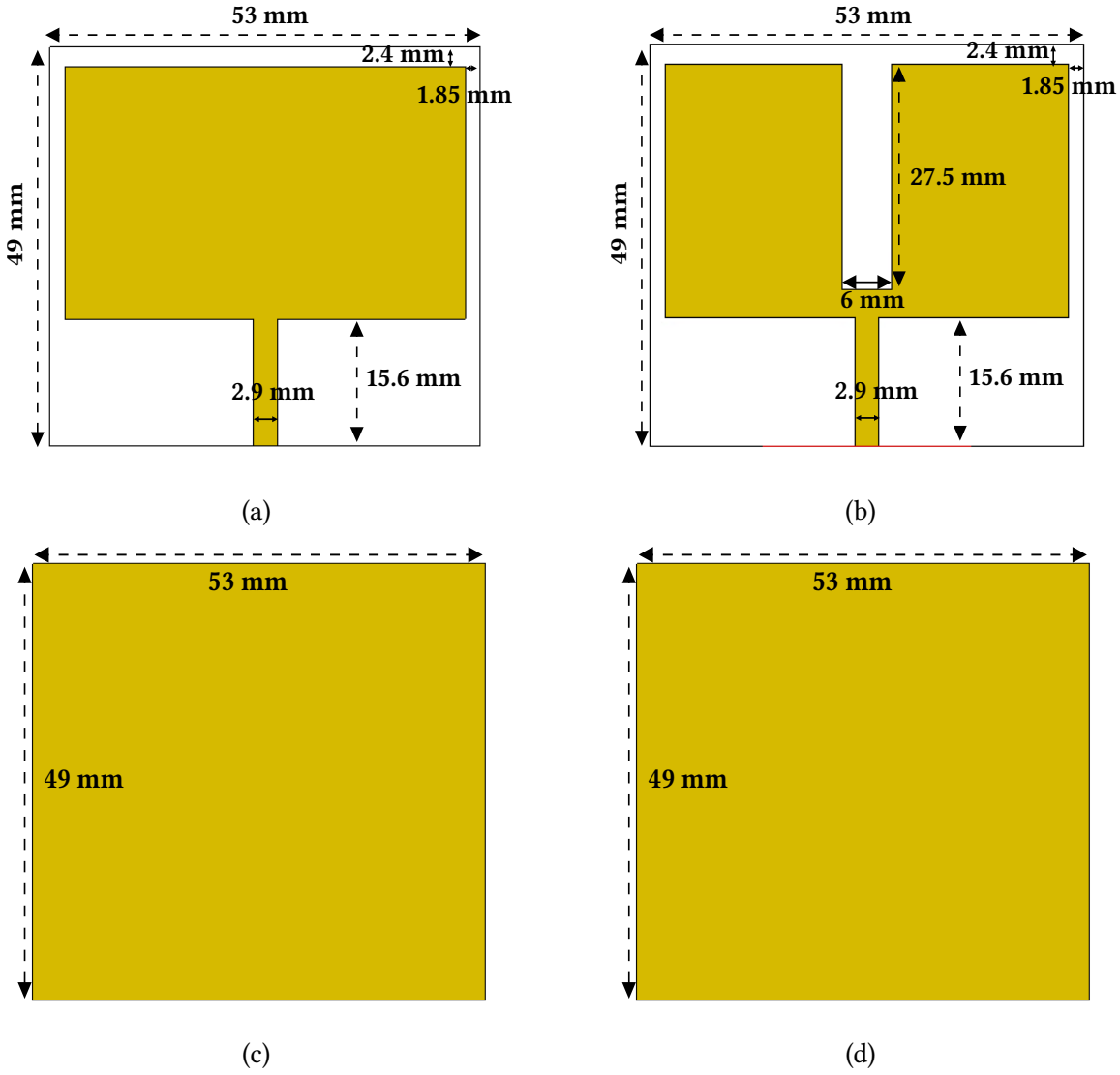


Figure 5.4: Top and bottom layer of the probe design. 5.4a Top layer optimization 1. 5.4b Bottom layer optimization 1. 5.4c Top layer optimization 2. 5.4d Bottom layer optimization 2.

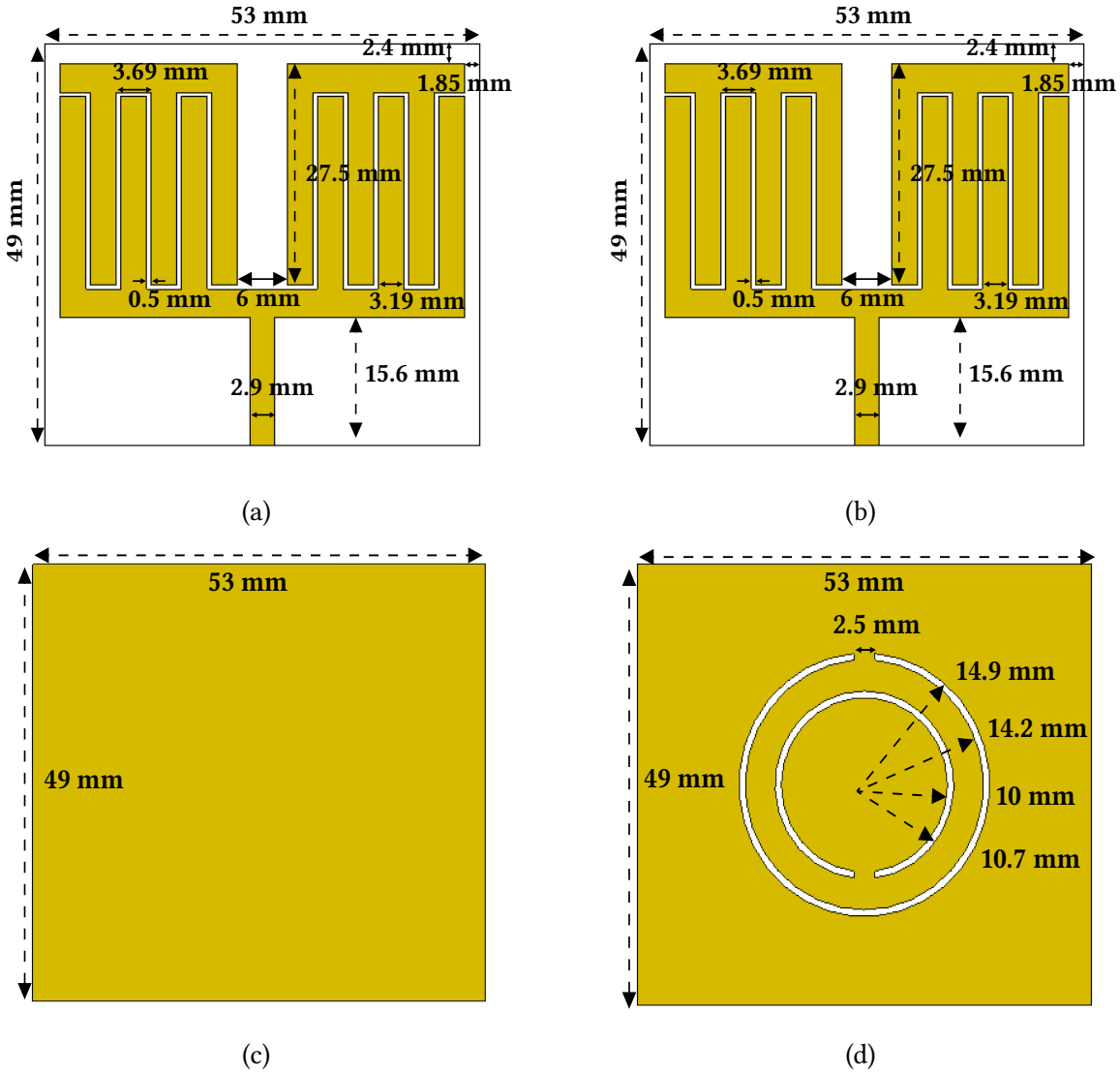
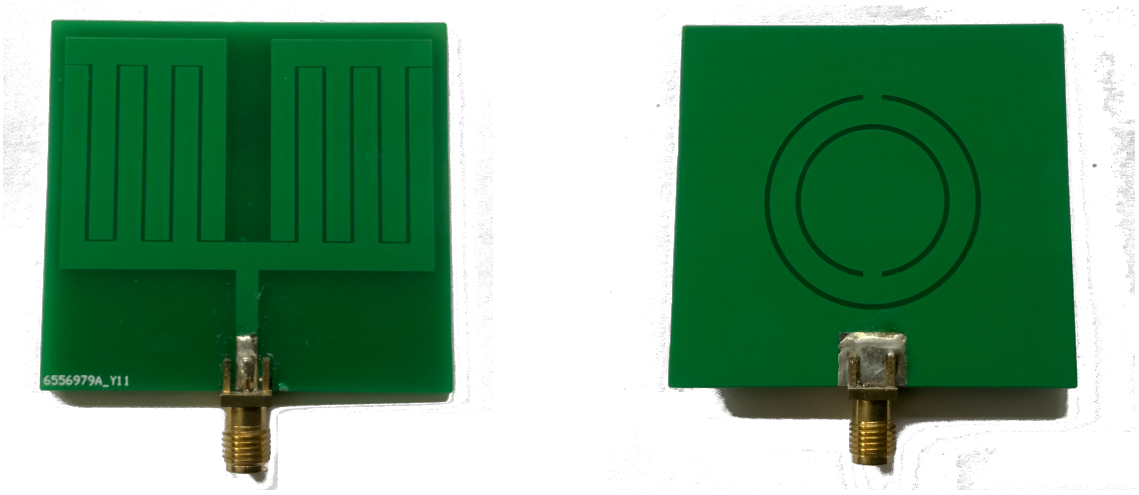


Figure 5.5: Top and bottom layer of the probe design. 5.5a Top layer optimization 1. 5.5b Bottom layer optimization 1. 5.5c Top layer optimization 2. 5.5d Bottom layer optimization 2.



(a) (b)

Figure 5.6: Design and fabricated - top and bottom layer antenna. 5.6a Fabricated antenna - FR-4 material - top layer view. 5.6b Fabricated antenna - FR-4 material - bottom layer view.

5.4 Self-organized Cellular automata classifier with genetic algorithm

A classifier based on computer machines uses several statistical techniques to decide if an unseen observation is within a specific class. In recent years, several studies have used binary classification to detect malignant cancer [168], for example. They have been shown to be a useful tool in discriminating between benign and malignant tumors. In [169] and [170], for example, Support Vector Machine (SVM) are applied as tools for BC detection. Another study [171] used an SVM classifier in detection BC using two features of the microwave tomography data. In particular, SVM has become popular for its ability to manage nonlinear relations between features and classes [172, 173]. The object of the SVM algorithm is to find the optimal hyperplane that separates the classes involved. In this work, for example, we deal with binary classification, then we can define a data set as $X = \left\{\bar{X}_1, \bar{X}_1, , \cdots, \bar{X}_n\right\}$ where $\bar{X}_i \in \mathbb{R}^m$, and we labeled the classes as 1, and 2, then $y = y_1, y_2, \cdots, y_n$ where $y_n \in \{1, 2\}$, then the hyperplane can be written as: $\bar{w}^T \bar{x} + b = 0$.

In [174], Decision Tree (DT) are used as a classifier for binary classification of BC. The researchers utilized a dataset with 699 instances, 10 attributes, and 2 classes, finding that DT performed more accurately than other machine learning methods. DT processes a collection

of input vector data associated with a class and produces a map that connects the attribute values of the mentioned vector data to classes [175]. Similarly, a tree in shape nodes represents features; from each of these features, a decision is made and defined by branches, and the process continues until the classification is performed, which is represented by leaves [176, 177]. This method has a lower complexity and its effectiveness is based on the characteristic of the data set [178].

We hope to find a solution to classify healthy and unhealthy according to the data collected from the MW probe, using a self-organized algorithm that can adapt to the complexities and changes in the data in the same way an artificial living organism behaves. For that purpose, we will implement self-organized CA for classification of healthy and tumorous breast tissue and compare its performance with SVM and DT.

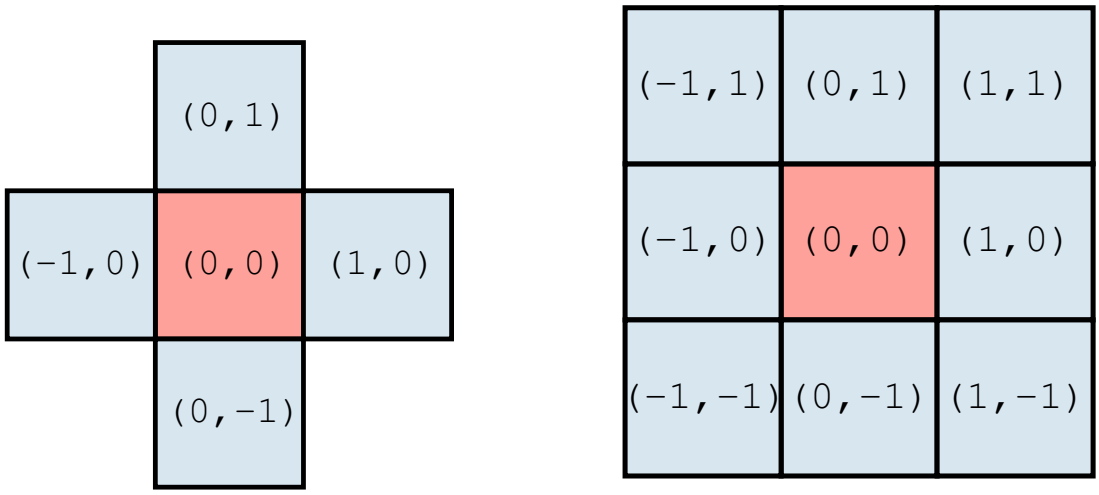
5.4.1 Self-Organized Cellular Automata

In a self-organized system, we can determine the current status of its organization within the cumulative local interactions that its individuals have performed in the past [179]; in other words, the interactions between individuals in a system will determine the global outcome or pattern. For example, the organization of thousands of cells into living organisms or the indirect collaboration or Stigmergy that some individuals created with the environment to build large patterns, such as buildings or nests [180]. Although there is no universally accepted definition of life [181], AL study of patterns in self-organized living systems and describe how individuals in a population can arrange themselves into patterns [182]. Several techniques have been developed to emulate self-organization, and one of these approaches is CA, which relies on local rules to end global patterns that cannot be predicted. We expect finding the optimal rule to adapt the behavior of the CA pattern to the complexity of the data generated for our BC detection system to discriminate between healthy and cancerous breast tissue. We also expected that the implementation of GA that encounters the rule to resolve the binary classification problem might not be the fastest option but the optimal, as several examples show in [183]

CA, presented by von Neumann in 1950, is a computational dynamical system, rooted in a discrete space, capable of representing many different behaviors [184]. Mathematically can be expressed as (n, S, N, f), where n is the space dimension of the cell grid (usually $n = 1, 2\ o\ 3$), S is the spaces of the possible cell estates of each cell $S = \{s_1, s_1, \cdots, s_k\}$, $N = (x_1, \cdots, x_v)$ represents the neighbourhood as tuple in $\mathbb{N}$, and x_i represents the neighbor's position with respect of the center cell of this neighborhood, and f represents the transition function. The status of each cell is the result of a calculation based on certain rules as a function of the status of its neighbors [185]. The idea in using CA rooted in the capability of this cell space to represent highly complex systems under discrete time, space, and states of the cells [186], we can find

several CA application examples such as simulation of pedestrian behavior at an intersection [187], how to model tumor growth [188], antenna design and performance [189], detection of anomalies in mammograms [190], classifying the presence of tumors in breast images [191], in cancer therapy simulation [192] to name a few.

Self-organized cellular automata operate based on local rules that determine the state of a single cell depending on the status of its neighbour. The neighborhood refers to a spatial area surrounding a central cell (0, 0), which updates its state according to its neighbouring states. This study utilizes a 2D cell space, offering several neighbourhood types. For example, Figure 5.7a illustrates the von Neumann neighborhood in 2D: four neighbors and the central cell. In contrast, Figure 5.7b depicts the Moore neighborhood, which includes eight cells, accounting for the corner cells.



(a) (b)

Figure 5.7: Representation of von Neuman and Moore neigh- borhoods. 5.7a von Neuman space. 5.7b Moore space.

There are various approaches to defining rules for classification problems using CA, ranging from simple to more complex methods. For example, the rule n4_v1 updates the central cell based on the highest value of the class in its neighboring cells. This rule is considered stable because the updated cell will not change in subsequent iterations [193]. The rule known as n4_V1_nonatable is defined as non-stable because the updated cell may change if the density of the class in its neighborhood changes. Table 5.1 illustrates this rule.

Table 5.1: The rule n4_v1_nonstable

0	if class 1 neighbors + class 2 neighbors = 0
1	if class 1 neighbors $>$ class 2 neighbors
2	if class 1 neighbors $<$ class 2 neighbors
rand[1,2]	if class 1 neighbors = class 2 neighbors

The "Game of Life" is a typical example of self-organized 2D CA; it was presented by John Horton Conway in 1970, and this work produced the interest of researchers and programmers in CA, particularly in the generation of oscillators and gliders [194]. The rules of the "Game of Life" were explained in this article [195], and we illustrate them in the following Figure 5.8. In this game, a cell births, death, or survives based on particular guidelines. We used the von Neumann neighborhood to demonstrate the rules.

1. If the center cell has one neighbor, it dies in the next generation (isolation) Figure 5.8b.
2. If the center cell has two or three neighbors, it survives for the next generation Figure 5.8c.
3. If the center cell has four or more neighbors, it dies in the next generation (overpopulation) Figure 5.8d.
4. If the center cell is empty and has exactly three neighbors it births in the next generation Figure 5.8e.

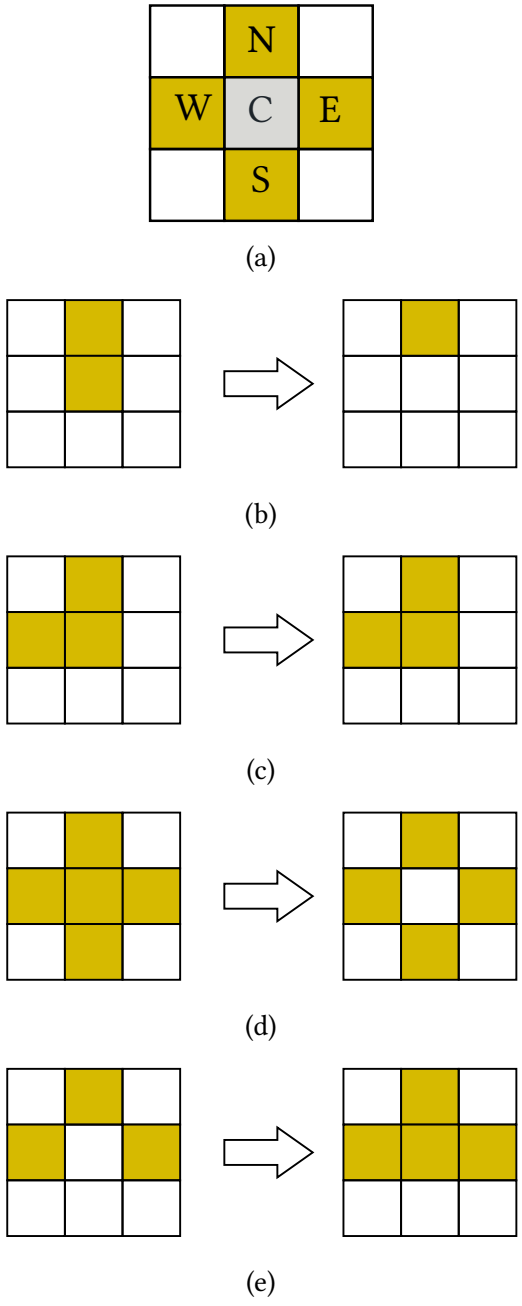


Figure 5.8: Game of Life rules: 1. 5.8a von Neuman neighborhood. 2. 5.8b If the center cell has one neighbor it dies in the next generation (isolation). 3. 5.8c If the center cell has two or three neighbors, it survives for the next generation. 4. 5.8d If the center cell has four or more neighbors, it dies in the next generation (overpopulation). 5. 5.8e If the center cell is empty and has exactly three neighbors it births in the next generation.

5.4.2 Genetic algorithm

The primary goal of using GA in this study is to identify the optimal rule among all possibilities within a defined space. In this case, we have four neighboring cells as in the von Neuman space. Each of these cells space can be in one of three states:

1. healthy,
2. unhealthy,
3. and Quiescent.

These three states produce 3^{3^5} possible rules. The objective of GA is to discover the most optimal rule within this vast space of possibilities.

The genetic algorithm (GA) is a heuristic technique that can solve different optimization problems. The basic algorithm [196], to apply this technique is shown in the following Table 5.2.

Table 5.2: The basic Genetic Algorithm (GA)

Algorithm: Basic Genetic Algorithm
initialize population
repeat
repeat
crossover
mutation
mapping
fitness
until population complete
selection
until accomplish condition

A technique based on a (GA) is used to find the rule for one-dimensional cellular automata in the experiment presented in [197], for this work, the number of possible rules is 2^{128}, and the bite that represents these rules has a length of 128 bits. In [198] GA is also used in detecting the 2D CA rules, in this case for three examples on a grid of 20x20 and 30x30. In the present work, the von Neumann neighborhood and three cell status (0, 1, 2) are used; the number of entries in the input table is $k^n = 3^5 = 243$, where k is the number of cell status, n is the number of cells in the neighborhood. The number of possible rules is given by $3^{k^n} = 3^{243}$, and the length of the bite that represents these rules is 243 bits.

5.5 Simulation results

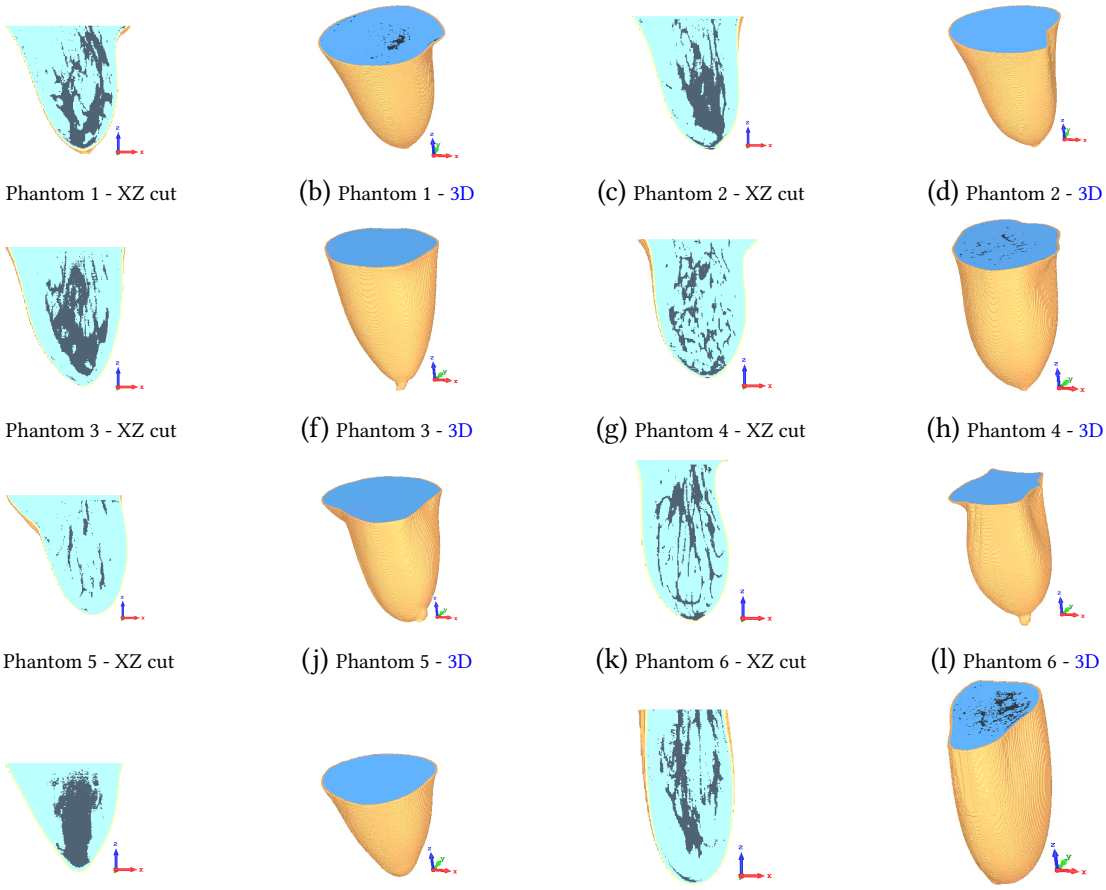
This section presents the results of the simulation of the BC detection system using EM software CST ®. We conducted 60 simulations with 3D realistic breast phantoms, categorized as follows:

(1) 30 simulations used healthy breast phantoms without any anomalies, and

(2) 30 simulations used realistic breast phantoms containing anomalies, referred to as unhealthy

We developed realistic voxelized phantoms using the software packages 3D Slicer, MATLAB ®, and CST ®, based on the data set presented in [199]. This data set contains 150 uncompressed breast phantoms, each with an average glandular fraction by mass of 12.3% and a diameter of 105 mm. The complex permittivity of fatty tissue, fibro-glandular tissue, and skin was calculated using the Debye parameters presented in [145]. Eight of the 30 realistic phantoms used in this study are shown in Figure 5.9. The image illustrates the variations in the geometry of these phantoms, which emphasizes that differences in physical compositions will aid in evaluating the antenna's ability to detect tumors within these phantoms.

The CST ® simulation setup consists of: (1) the designed probe, (2) an uncompressed realistic breast phantom, and (3) a 10 mm diameter PEC sphere nominated as a tumor. Figure 5.10 shows the CST ® simulation setup and defines that the distance between the antenna and the breast phantom is 10 mm. This setup was designed to accommodate 60 simulations involving 30 phantoms, with and without PEC tumors. Each phantom was tested in two scenarios: first, without any anomalies and then with an anomaly present. In both situations, we recorded the reflection coefficient S_{11} from the designed antenna. Figure 5.11 displays eight measurements taken from four different phantoms. Solid lines represent the reflection coefficients obtained from healthy breast samples, while dashed lines indicate the S_{11} values of unhealthy breast phantoms. In particular, the difference in the reflection coefficients between the healthy and unhealthy samples shows a clear separation, which will aid in detecting tumors within the breast.



(a) Phantom 1 - XZ cut (b) Phantom 1 - 3D (c) Phantom 2 - XZ cut (d) Phantom 2 - 3D

(e) Phantom 3 - XZ cut (f) Phantom 3 - 3D (g) Phantom 4 - XZ cut (h) Phantom 4 - 3D

(i) Phantom 5 - XZ cut (j) Phantom 5 - 3D (k) Phantom 6 - XZ cut (l) Phantom 6 - 3D

(m) Phantom 7 - XZ cut (n) Phantom 7 - 3D (o) Phantom 8 - XZ cut (p) Phantom 8 - 3D

Figure 5.9: Eight of the 30 Simulated Phantoms in CST ® - XZ cutting plane and 3D view

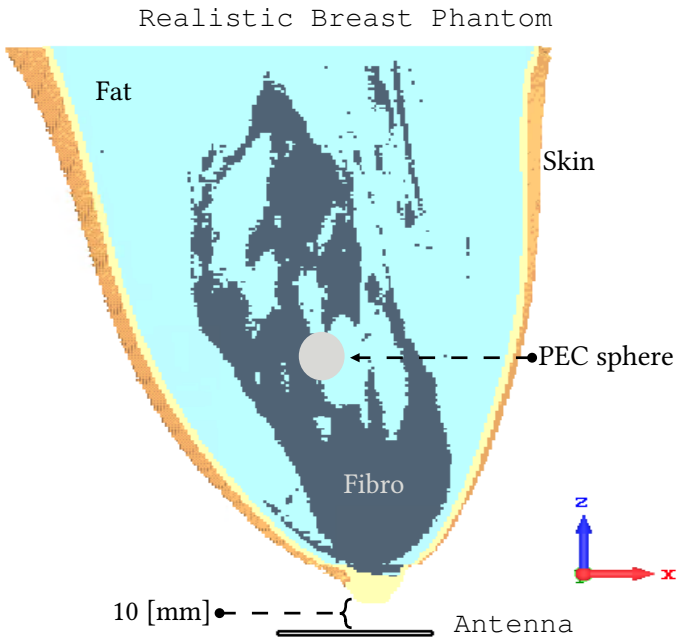


Figure 5.10: Simulated realistic phantom in CST ® X-Z cut

We extracted data from the reflection coefficient samples collected during the simulation to feed the self-organizing algorithm. This involved gathering the minimum S_{11} value and its corresponding frequency. The data set is divided into 70% for training and 30% for testing. The training data set serves as the seed for the self-organized CA grid depicted in Figure 5.12. In this study, a 30×30 grid space is utilized, where each cell can represent a healthy state (class 1), an unhealthy state (class 2), or an unclassified Quiescent state (class 0). The next step involves applying a rule to each cell in the grid, which helps update the cell's status based on the states of its von Neumann neighbors. The algorithm continues to run until no unclassified cells remain, resulting in variable iterations. Once all cells on the grid are updated, a self-organized pattern emerges, allowing the classification of healthy and unhealthy breast tissue.

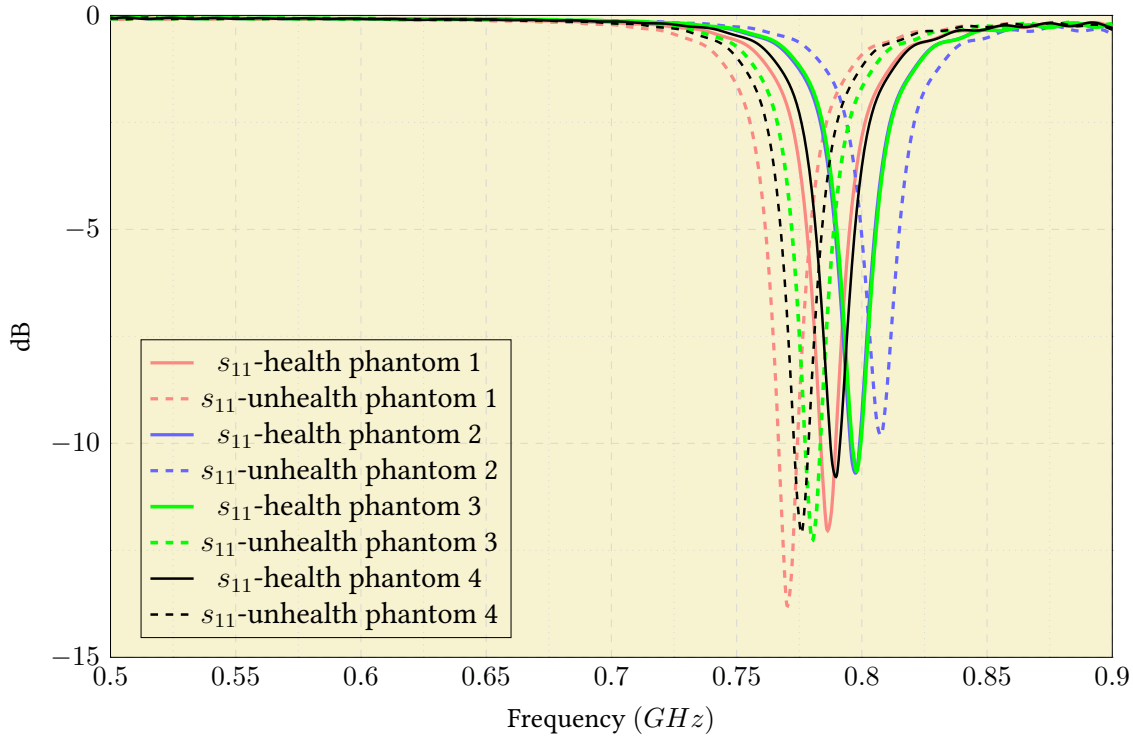


Figure 5.11: Eight S_{11} measurements taken from four different phantoms (with and without tumor) using the designed antenna CST ®

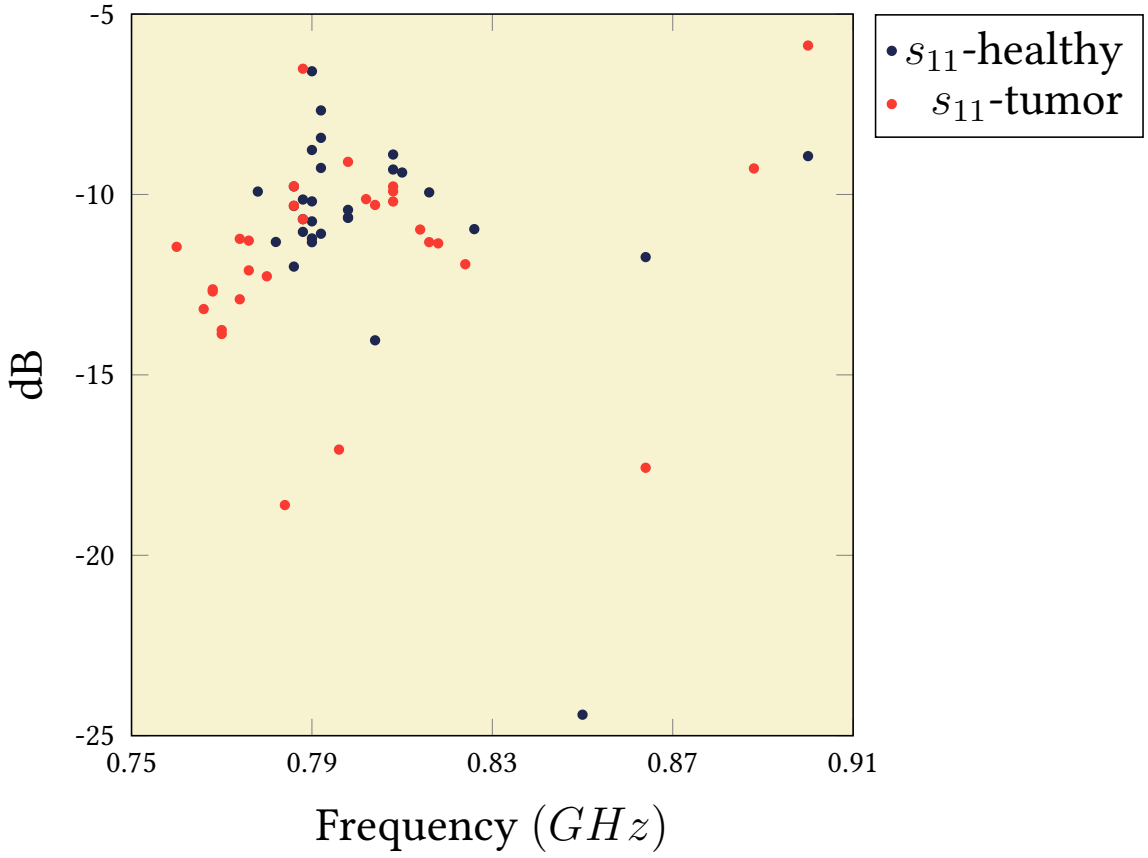


Figure 5.12: Training data sample S_{11} for seeding the self-organizing algorithm was measured from the designed antenna using CST ® during numerical simulation, mimicking healthy and tumor breast tissue with a tumor diameter of 10 mm.

We present the results of the self-organized CA classifier in Table 5.3, along with the results of the SVM and DT techniques. This Table 5.3 has two columns dedicated to the CA classifier. The first column, designated as "$n4_v1_nonstable$", presents the results obtained by applying the CA classifier, using the corresponding constant rule of the same name and presented in Table 5.1. The second column, "CA-GA" presents the results of the self-organized CA classifier using the rule identified through GA, which we proposed to process the data set generated by the MW probe in this study. Furthermore, the column labeled "DT" shows the results of the DT

classifier, while the column "SVM" presents the results of the SVM classifier.

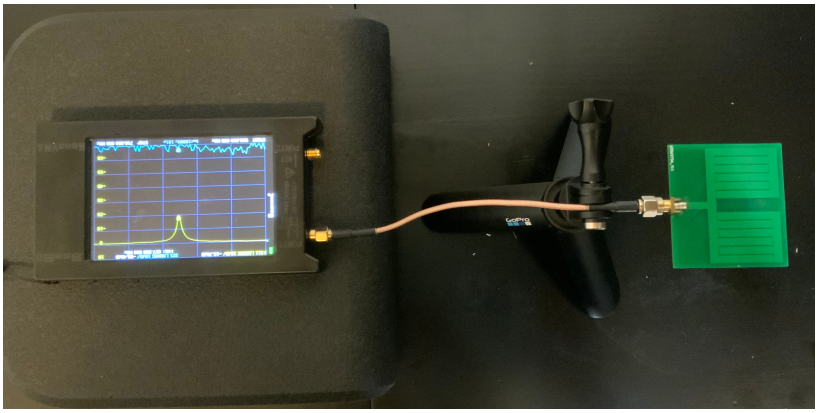
Our self-organized CA classifier performed better compared to the other classifiers shown in Table 5.3 in Sensitivity, Specificity, NPV, and Accuracy. The probability of detecting unhealthy breast tissue reached 0.8333, the highest among all classifiers. The self-organized CA classifier that uses the GA rules is particularly effective in identifying cases where a tumor is present. It is a better classifier to predict when the tumor is absent, with a probability of 0.6333. The probability of correct classification reached 0.6875, the highest value among the classifiers tested. It is important to note that the data set shown in Figure 5.12 contains several opposing values (healthy and unhealthy) that are very close to each other. This proximity makes data classification more challenging. It also highlights the ability of self-organized CA combined with GA to manage complex data sets effectively.

Table 5.3: Classifier performance on data from the tumor detection system phantom-antenna

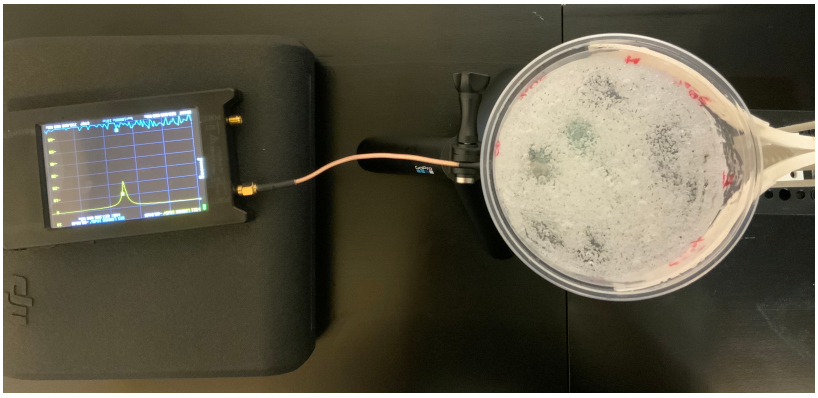
Metric	$n4_v1_nonstable$	$CA-GA$	DT	SVM
Sens	50.00	**83.33**	61.43	50.00
Spec	50.00	**63.33**	50.00	50.00
NPV	37.50	**87.50**	37.50	37.50
PPV	62.50	50.00	**87.50**	62.50
Acc	50.00	**68.75**	62.50	50.00

5.6 Experimental results

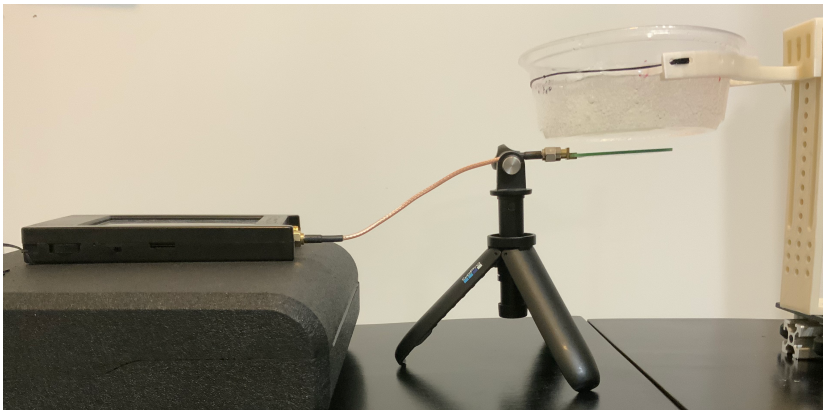
The setup for the experiment includes the probe MW and the Nano Vector Network Analyzer (VNA)-H4 [200], as illustrated in Figure 5.13a. The Nano VNA-H4 is a portable vector network analyzer that operates in a frequency range of 50 kHz to 1.5 GHz. The Nano VNA can be connected directly to a computer to capture S_{11} data points. Figures 5.13b and 5.13c demonstrate the procedure for conducting experimental measurements; a total of 24 S_{11} readings were obtained using the Nano VNA. Every measurement is composed of 201 data points arranged in two columns: one represents the frequency, and the other indicating the reflection coefficient. There are two methods to obtain data from the device: (1) utilize a flash drive or (2) link the Nano VNA to the computer through the C-USB port. We used the C-USB connection together with the NanoVNA-App [201] to operate the device and record data points via this interface.



(a)



(b)



(c)

Figure 5.13: Experiment Setup. 5.13a Antenna experiment setup NanoVNA H4 and antenna - top view. 5.13b Antenna experiment setup NanoVNA H4 and antenna and phantom - top view. 5.13c Antenna experiment setup NanoVNA H4 and antenna and phantom - side view

The experimental validation for this study utilized the same breast phantoms created in the previous Chapter 3, depicted in Figure 3.13. These phantoms mimic breast tissue in a wide range of frequencies [150]. The system evaluated twelve ARBP in two ways: (1) twelve phantoms without tumor inside labeled as healthy, (2) twelve ARBP with a PEC sphere inside labeled as unhealthy. The tumor size for this experiment is 10 mm in diameter, which is smaller than the sizes reported in the survival expectation [158]. In order to measure the reflection coefficient, the MW probe was connected to the H4 Nano VNA, and lastly to the computer where we store the whole set of measurements. An illustration of 4 of the 12 phantom measurements is shown in Figure 5.14, this picture shows the reflection coefficient recorded; the solid line represents the ARBP without a tumor inside, i.e. healthy, the dashed line indicates the ARBP with a tumor inside named unhealthy. According to the information displayed in this picture, the sensor can sense the difference in the mimic breast tissue.

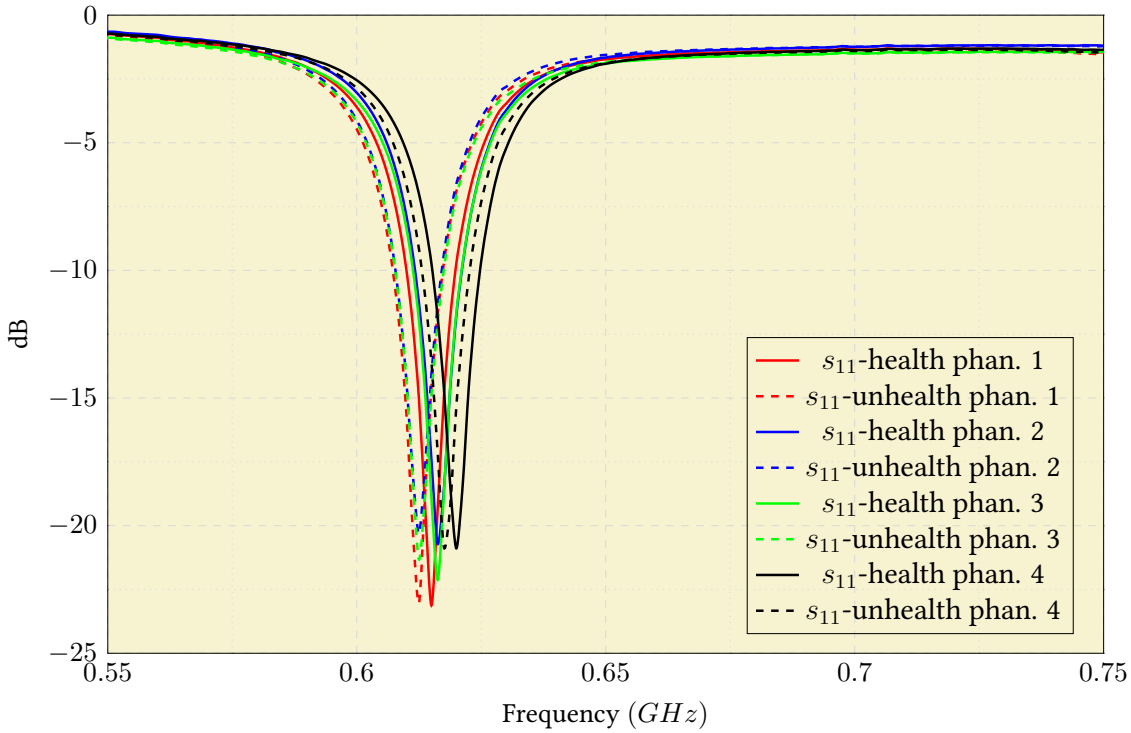


Figure 5.14: Eight S_{11} measurements taken from four different phantoms (with and without tumor) using the designed antenna and Nano VNA H4

Once we collected the complete set of 24 data points for the reflection coefficient, we iden-

tified the lowest values for the different frequencies to analyze using the self-organized classifiers implemented in this investigation. The data points are depicted in a 2D view in Figure 5.15 and will serve as the data set for binary classification; to facilitate this, we divided the dataset into 70% for training and 30% for testing. The information does not indicate a distinct pattern; it is spread throughout the grid. All recorded data points were processed using Python [151, 152, 153, 154, 155, 156, 157], where the algorithms were implemented. The experiment was carried out in one continuous session, from start to finish; This was feasible because VNA remained powered by C-USB throughout; this choice allowed us to maintain consistent conditions for all measurement outcomes in the experiment. Although the measurement process may seem simple because of the handling capability of the system, measurements were conducted three times to avoid any possible issues with the setup, connection cables, and equipment. The gap between the phantom and the MW probe was established at 10 mm, while the PEC sphere that served as a tumor within the phantom measured 10 mm in diameter.

Table 5.4 shows the effectiveness of the self-organized algorithms CA, DT, and SVM. Although the data set is limited, the metrics presented in the Table 5.4 show that our self-organized classifier CA using the GA rule, scored the best. The likelihood of correctly identifying healthy (phantom without tumor) and unhealthy (phantom with tumor) samples is 0.6861. The correct classification when a phantom contains a tumor by the CA with the GA rule has a probability of 0.6663. At the same time, the probability that this technique classifies correctly when no tumor is present in the phantom reaches 0.8056.

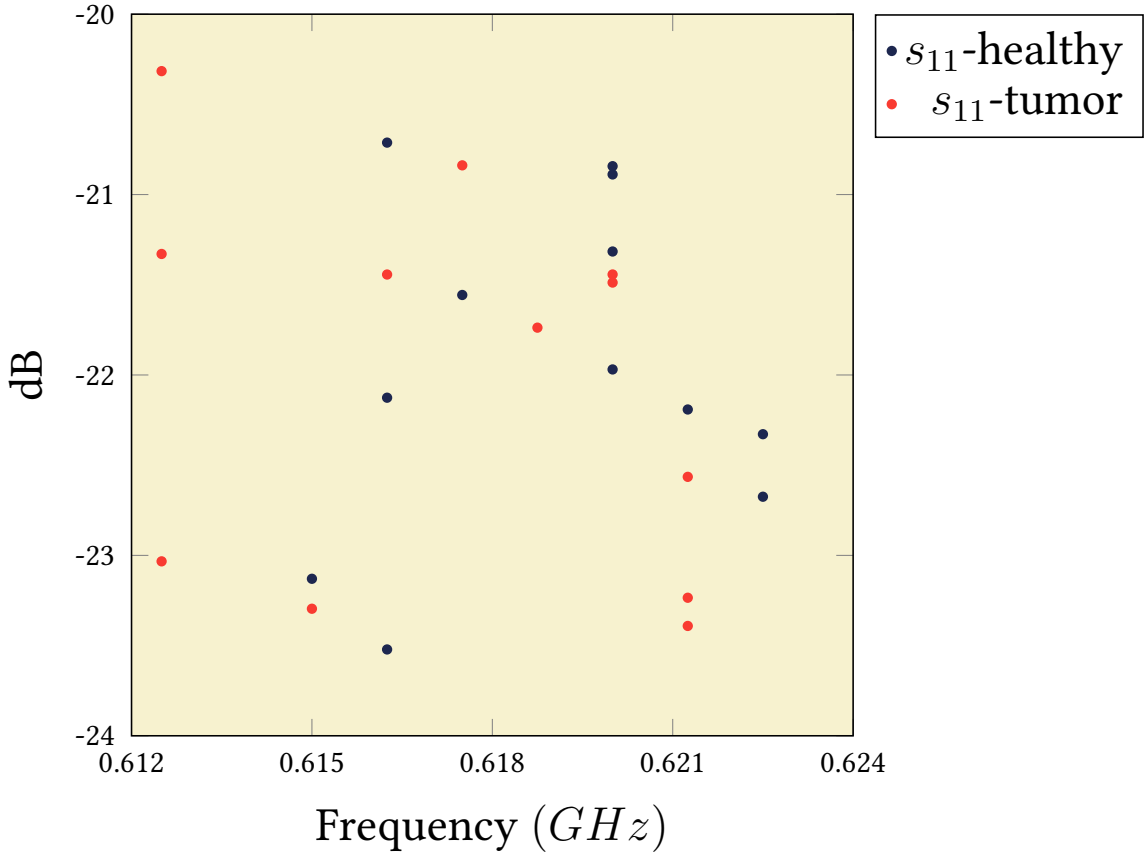


Figure 5.15: Training data sample S_{11} for seeding the self-organizing algorithm was measured from the designed antenna using the Nano VNA during experimental validation, mimicking healthy and tumor breast tissue with a tumor diameter of 10 mm.

Table 5.4: Classifier performance on data from the tumor detection system phantom-antenna

Metric	$CA\ n4_v1$	$CA - GA$	DT	SVM
Sens	61.43	**66.63**	59.22	64.29
Spec	57.50	**80.56**	52.32	55.87
NPV	62.22	51.11	51.11	**80.37**
PPV	56.88	**89.63**	59.26	42.13
Acc	59.50	**68.61**	55.56	57.41

5.7 Conclusion

The primary concept focuses on how variations in the material lead to alterations in the reflection coefficient. We utilized realistic breast phantoms as our base material and introduced perturbations within them using a PEC sphere to emulate tumors. We recorded the reflection coefficients of the phantoms, analyzing situations with and without tumors. The data obtained indicate that the probe MW presented in this work can detect variations in tissue composition during both simulations and experimental trials. We implemented the concept of self-organization from AL through programming CA to distinguish between healthy and unhealthy individuals. This approach demonstrated a robust ability to handle complex information and surpassed the conventional machine learning methods tested in this study. Instead of employing a fixed rule, we used a genetic algorithm to discover the optimal solution to this problem.

The probability of the system accurately identifying healthy and unhealthy breast phantoms was about 0.68 in both the simulations and the experimental tests. In the simulation case, we observed that the complexities of the data impacted the results. Furthermore, the system dealt with limited data points during the experimental validation, significantly affecting the final outcome. We estimated that by increasing the data set in both cases, the result of this classifier would produce better results. It should be emphasized that the antenna was stimulated during the experimental test with a Nano VNA H4 device. The reflection coefficient data points were collected using a standard computer, which offers various benefits, such as its relevance for clinical trials and its cost-effective nature. The antenna was constructed from commonly accessible material FR-4, which contributed to reduced production expenses.

Chapter 6

Conclusion and Future Work

The purpose of this chapter is to present a summary of the accomplished work led by this thesis and to provide suggestions for future work.

6.1 Accomplished Work

This thesis presents a comprehensive simulation of the physical compression of an anatomically realistic breast phantom through biomechanical finite element analysis. Subsequent chapters utilize the compressed phantom for electromagnetic simulations to meet the thesis objectives. The uncompressed and realistic model was sourced from the UWCEM repository and generated from 3D MRI images (**Chapter 2**).

Introduction of a novel concept involving electromagnetic energy, specifically applied to the detection of breast cancer. The proposed technique utilizes a field detector probe inspired by the concept of a metasurface made up of electrically small elements. The probe can scan the field generated by a specific structure, such as a human female breast, achieving a resolution in the millimeter range while operating within the low-microwave-frequency spectrum. The scanning system has been tested numerically and a prototype was fabricated to validate its effectiveness experimentally (**Chapter 3**).

A novel metasurface sensor designed to operate at sub-microwave frequencies for cancer detection has been introduced. This microwave sensor has demonstrated its ability to identify anomalies in the breast that may or may not be cancerous. The technique was analyzed through simulations using realistic phantoms and validated through experimental verification (**Chapter 4**).

Develop a breast cancer detection system that uses a low-frequency microwave probe combined with a self-organizing algorithm. This method has shown effectiveness in classifying breast tissues, determining whether they contain tumor cells, and has outperformed traditional machine learning techniques. The system has been tested through electromagnetic simulations and has undergone experimental validation (**Chapter 5**).

6.2 List of Publications

1. Mauricio Hernandez, Omar M. Ramahi. Microwave Near-Field Breast Cancer Detection Using a Metasurface of 3mm Cell at 200 MHz. 2024 IEEE Microwaves, Antennas, and Propagation Conference (MAPCON) - RF technologies for medical, space, defence, 5G/6G communications (Accepted)

2. Mauricio Hernandez, Hamid Akbari-Chelaresi, Ghazaleh Tashtarian, and Omar M. Ramahi. Microwave energy scanning: An Application in Breast Cancer Detection. 2024 IEEE Journal of Electromagnetics, RF, and Microwaves in Medicine and Biology (Under review)

3. Mauricio Hernandez, Hamid Akbari-Chelaresi, Ghazaleh Tashtarian, and Omar M. Ramahi. Radio Frequency Mammography using Subtractive Imaging with Histogram of Oriented Gradients. IEEE AP-S/URSI 2025 Antenna Applications and Emerging Technologies, Biomedical applications. Antenna Enhancements, Metasurface and metamaterial antennas (Accepted)

4. Hamid Akbari-Chelaresi, Ghazaleh Tashtarian, Mauricio Hernandez, and Omar M. Ramahi. Low-Frequency Subwavelength Metasurface-Based System for Breast Cancer Detection. IEEE AP-S/URSI 2025 Antenna Applications and Emerging Technologies, Biomedical applications. Electromagnetics: Theory, Materials, and Education, Metamaterials and metasurfaces (Accepted)

5. Ghazaleh Tashtarian, Hamid Akbari-Chelaresi, Mauricio Hernandez, Farzan Mirshekari, Abdolali Abdipour, Ahad Tavakoli, Omar M. Ramahi. Mitigating Misalignment of Excitation Sources in Low-Frequency Mammography. IEEE AP-S/URSI 2025 Antenna Applications and Emerging Technologies, Biomedical applications. Electromagnetics: Theory, Materials, and Education, Metamaterials and metasurfaces (Accepted)

6. Ghazaleh Tashtarian, Hamid Akbari-Chelaresi and Mauricio Hernandez (University of Waterloo, Canada); Abdolali Abdipour and Ahad Tavakoli (Amirkabir University of Technology, Iran); Omar Ramahi (University of Waterloo, Canada). Magnetic Field Imaging for

Enhanced Breast Cancer Detection. 2024 IEEE MTT-S International Microwave Biomedical Conference (IMBioC) - Antennas and propagation for biomedical applications (Accepted)

7. Omar M. Ramahi, Hamid Akbari-Chelaresi, Mauricio Hernandez and Ghazaleh Tashtarian. Effect of Source Polarization on Computed Tomography Using Low Frequency Electromagnetic Energy. 2024 IEEE Conference on Antenna Measurements and Applications (CAMA) (Accepted)

8. Ghazaleh Tashtarian, Hamid Akbari-Chelaresi, Mauricio Hernandez, Abdolali Abdipour, Ahad Tavakoli, Omar M. Ramahi, "Using Electrically Small Electromagnetic Sources for Breast Cancer Detection in Low Frequencies," 2024 IEEE International Symposium on Antennas and Propagation and INC/USNC-URSI Radio Science Meeting (AP-S/INC-USNC-URSI), Firenze, Italy, 2024, pp. 273-274, doi: 10.1109/AP-S/INC-USNC-URSI52054.2024.10686716 (Accepted)

9. Ghazaleh Tashtarian, Hamid Akbari-Chelaresi, Mauricio Hernandez, Abdolali Abdipour, Ahad Tavakoli, Omar M. Ramahi, "A Low-Frequency Electromagnetic Field Mammography Setup: Experimental Study", IEEE Transactions on Antennas and Propagation. (Submitted)

10. Ghazaleh Tashtarian, Ahad Tavakoli, Abdolali Abdipour, Hamid Akbari-Chelaresi, Mauricio Hernandez, Ali M. Almuhlafi, Omar M. Ramahi, "Mitigating Source and Breast Misalignment in Low-Frequency Breast Tumor Detection", Signal Processing. (Submitted)

6.3 Future Work

1. **Design** an automated system to transfer data from the metasurface to a computer. This phase involves developing an electronic implementation to read voltages at the operational frequency, which supports clinical testing. Once this automated system is fully developed, clinical tests can begin.

2. **Improve** the design of the mechanical scanning system to facilitate clinical testing. A clinical trial tailored for this technique would be more aligned with real-world applications and help validate the potential of microwave scanning for breast cancer detection. This trial would provide an excellent opportunity to showcase the true capabilities of the scanning method. By obtaining high-quality images and collecting a substantial database from volunteers, we can effectively confirm the practicality of this innovative approach, particularly when integrated with artificial intelligence, for detecting breast cancer.

3. **Implement** a clinical trial to test the microwave detection system with a self-organized algorithm. We anticipate that a clinical trial will help confirm the proposed concept.

4. **Conduct** a study on the simulation of the physical compression of the realistic breast phantom that incorporates a flexible paddle to evaluate its effect on women's breasts and suggest improvements in the screening process.

References

[1] Globocan. All cancers fact sheet. Technical report, International Agency for Research on Cancer, 2022.

[2] Darren R. Brenner, Abbey Poirier, Ryan R. Woods, Larry F. Ellison, Jean-Michel Billette, Alain A. Demers, Shary Xinyu Zhang, Chunhe Yao, Christian Finley, Natalie Fitzgerald, Nathalie Saint-Jacques, Lorraine Shack, Donna Turner, and Elizabeth Holmes. Projected estimates of cancer in canada in 2022. *CMAJ*, 194(17):E601–E607, 2022.

[3] Canadian Cancer Society. Snapshot of incidence, mortality and survival estimates by cancer type. Technical report, Canadian Cancer Society, 2022.

[4] Sara Dorri, Farkhondeh Asadi, Asiie Olfatbakhsh, and Alireza Kazemi. A systematic review of electronic health (ehealth) interventions to improve physical activity in patients with breast cancer. *Breast Cancer*, 27(1):25–46, 2020.

[5] Kathryn E. Post and Jane Flanagan. Web based survivorship interventions for women with breast cancer: An integrative review. *European Journal of Oncology Nursing*, 25(Complete):90–99, 2016.

[6] Trevor S Mafu, Alison V September, and Delva Shamley. The potential role of angiogenesis in the development of shoulder pain, shoulder dysfunction, and lymphedema after breast cancer treatment. *Cancer management and research*, 10:81–90, 2018.

[7] E.C. Fear, P.M. Meaney, and M.A. Stuchly. Microwaves for breast cancer detection? *IEEE Potentials*, 22(1):12–18, 2003.

[8] Ophira Ginsburg, Cheng-Har Yip, Ari Brooks, Anna Cabanes, Maira Caleffi, Jorge Antonio Dunstan Yataco, Bishal Gyawali, Valerie McCormack, Myrna McLaughlin de Anderson, Ravi Mehrotra, Alejandro Mohar, Raul Murillo, Lydia E. Pace, Electra D. Paskett, Anya Romanoff, Anne F. Rositch, John R. Scheel, Miriam Schneidman, Karla Unger-Saldaña, Verna Vanderpuye, Tsu-Yin Wu, Safina Yuma, Allison Dvaladze, Catherine Dug-

gan, and Benjamin O. Anderson. Breast cancer early detection: A phased approach to implementation. *Cancer*, 126(S10):2379–2393, 2020.

[9] Akhlesh. Lakhtakia and Cynthia M. Furse. *The World of Applied Electromagnetics : In Appreciation of Magdy Fahmy Iskander*. Springer International Publishing, Cham, 1st ed. 2018. edition, 2018.

[10] Rohit Chandra, Huiyuan Zhou, Ilangko Balasingham, and Ram M. Narayanan. On the opportunities and challenges in microwave medical sensing and imaging. *IEEE Transactions on Biomedical Engineering*, 62(7):1667–1682, 2015.

[11] Sverre Brovoll, Tor Berger, Yoann Paichard, Oyvind Aardal, Tor Sverre Lande, and Svein-Erik Hamran. Time-lapse imaging of human heart motion with switched array uwb radar. *IEEE transactions on biomedical circuits and systems*, 8(5):704–715, 2014.

[12] S. Y. Semenov, V. G. Posukh, A. E. Bulyshev, T. C. Williams, Y. E. Sizov, P. N. Repin, A. Souvorov, and A. Nazarov. Microwave tomographic imaging of the heart in intact swine. *Journal of electromagnetic waves and applications*, 20(7):873–890, 2006.

[13] S M Salvador, E C Fear, M Okoniewski, and J R Matyas. Exploring joint tissues with microwave imaging. *IEEE transactions on microwave theory and techniques*, 58(8):2307–2313, 2010.

[14] J D Shea, P Kosmas, B D Van Veen, and S C Hagness. Contrast-enhanced microwave imaging of breast tumors: a computational study using 3d realistic numerical phantoms. *Inverse problems*, 26(7):074009–074009, 2010.

[15] Haosheng Fu, Fengzhou Dai, and Ling Hong. Metasurface aperture design for far-field computational microwave imaging beyond rayleigh diffraction limitations. *IEEE transactions on microwave theory and techniques*, 72(1):1–19, 2024.

[16] Shanwen Luo, Zhong Ji, Sihua Yang, and Da Xing. Near-field transmission-type microwave imaging for noninvasive evaluation of electromagnetic characteristics: Toward early breast tumor detection. *IEEE photonics journal*, 9(6):1–10, 2017.

[17] Lulu Wang. Microwave imaging and sensing techniques for breast cancer detection. *Micromachines (Basel)*, 14(7):1462–, 2023.

[18] Md Zulfiker Mahmud, Mohammad Tariqul Islam, Norbahiah Misran, Ali F Almutairi, and Mengu Cho. Ultra-wideband (uwb) antenna sensor based microwave breast imaging: A review. *Sensors (Basel, Switzerland)*, 18(9):2951–, 2018.

[19] M. Slaney, A.C. Kak, and L.E. Larsen. Limitations of imaging with first-order diffraction tomography. *IEEE transactions on microwave theory and techniques*, 32(8):860–874, 1984.

[20] Jiale Zhang, Chenzhe Li, Weichao Jiang, Zhicheng Wang, Lejia Zhang, and Xiong Wang. Deep-learning-enabled microwave-induced thermoacoustic tomography based on sparse data for breast cancer detection. *IEEE transactions on antennas and propagation*, 70(8):6336–6348, 2022.

[21] Martina T. Bevacqua and Rosa Scapaticci. A compressive sensing approach for 3d breast cancer microwave imaging with magnetic nanoparticles as contrast agent. *IEEE transactions on medical imaging*, 35(2):665–673, 2016.

[22] Ümit İrgin, Can Bariş Top, Damla Alptekin Soydan, and Nevzat G. Gençer. Enhancing the sensitivity of harmonic motion microwave doppler imaging using main signal cancellation circuit. In *12th European Conference on Antennas and Propagation (EuCAP 2018)*, pages 1–5, 2018.

[23] Aleksandar Jeremic and Elham Khoshrowshahli. Detecting breast cancer using microwave imaging and stochastic optimization. In *2015 37th Annual International Conference of the IEEE Engineering in Medicine and Biology Society (EMBC)*, pages 89–92, 2015.

[24] Maged A Aldhaeebi, Khawla Alzoubi, Thamer S Almoneef, Saeed M Bamatraf, Hussein Attia, and Omar M Ramahi. Review of microwaves techniques for breast cancer detection. *Sensors (Basel, Switzerland)*, 20(8):2390–, 2020.

[25] David M. Witten. Mammography: Advantages and limitations. *Postgraduate medicine*, 36(3):242–246, 1964.

[26] Emine Devolli-Disha, Suzana Manxhuka-Kerliu, Halit Ymeri, and Arben Kutllovci. Comparative accuracy of mammography and ultrasound in women with breast symptoms according to age and breast density. *Bosnian journal of basic medical sciences*, 9:131–6, May 2009.

[27] Yingjiao Wang, Yuechong Li, Yu Song, Chang Chen, Zhe Wang, Linrong Li, Mohan Liu, Guanmo Liu, Yali Xu, Yidong Zhou, Qiang Sun, and Songjie Shen. Comparison of ultrasound and mammography for early diagnosis of breast cancer among Chinese women with suspected breast lesions: A prospective trial. *Thoracic cancer*, 13(22):3145–3151, 2022. Place: Melbourne Publisher: John Wiley & Sons Australia, Ltd.

[28] Maria C. Calomarde, Javier De Santiago, Ignacio Zapardiel, and Debmalya Barh. Metabolomics in Breast Cancer. In *Metabolomics in Breast Cancer*, pages 211–224. Springer India, New Delhi, 2014.

[29] Cécile M. Ronckers, Christine A. Erdmann, and Charles E. Land. Radiation and breast cancer: a review of current evidence. *Breast Cancer Research*, 7(1):21, November 2004.

[30] Amy Berrington de González and Sarah Darby. Risk of cancer from diagnostic X-rays: estimates for the UK and 14 other countries. *The Lancet*, 363(9406):345–351, January 2004.

[31] Norman F. Boyd, Helen Guo, Lisa J. Martin, Limei Sun, Jennifer Stone, Eve Fishell, Roberta A. Jong, Greg Hislop, Anna Chiarelli, Salomon Minkin, and Martin J. Yaffe. Mammographic density and the risk and detection of breast cancer. *New England Journal of Medicine*, 356(3):227–236, 2007.

[32] P. Skaane. Studies Comparing Screen-Film Mammography and Full-Field Digital Mammography in Breast Cancer Screening: Updated Review. *Acta Radiologica*, 50(1):3–14, 2009. Place: London, England Publisher: Informa UK Ltd.

[33] Jessica Fitzjohn, Cong Zhou, and J. Geoffrey Chase. Critical Assessment of Mammography Accuracy. *22nd IFAC World Congress*, 56(2):5620–5625, January 2023.

[34] Lesley D. (Lesley Deanne) Dunfield, Melissa. Severn, and Canadian Agency for Drugs and Technology in Health. *Effectiveness of magnetic resonance imaging (MRI) screening for women at high risk of breast cancer*. Technology report HTA ; issue 93. Canadian Agency for Drugs and Technology in Health, Ottawa, Ont, 2007.

[35] Luca Nicosia, Anna Carla Bozzini, Simone Palma, Filippo Pesapane, Lorenza Meneghetti, Maria Pizzamiglio, Francesca Abbate, Antuono Latronico, Vincenzo Bagnardi, Samuele Frassoni, Claudia Sangalli, and Enrico Cassano. Breast imaging reporting and data system and contrast enhancement mammography: Lesion conspicuity likelihood of malignancy and relationship with breast tumor receptor status. *Academic Radiology*, 30(10):2243–2251, 2023.

[36] Norman F Boyd, Helen Guo, Lisa J Martin, Limei Sun, Jennifer Stone, Eve Fishell, Roberta A Jong, Greg Hislop, Anna Chiarelli, Salomon Minkin, and Martin J Yaffe. Mammographic density and the risk and detection of breast cancer. *The New England journal of medicine*, 356(3):227–236, 2007.

[37] Donella Puliti, Stephen W. Duffy, Guido Miccinesi, Harry De Koning, Elsebeth Lynge, Marco Zappa, and Eugenio Paci. Overdiagnosis in mammographic screening for breast cancer in europe: A literature review. *J Med Screen*, 19(1 suppl):42–56, sep 2012.

[38] W. Tania Rahman and Mark A. Helvie. Breast cancer screening in average and high-risk women. *Best Practice & Research Clinical Obstetrics & Gynaecology*, 83:3–14, 2022. Breast Cancer Screening, Breastfeeding & Benign Breast Disease.

[39] Aashna Anand, Seungho Jung, and Sukhan Lee. Breast Lesion Detection for Ultrasound Images Using MaskFormer. *Sensors (Basel, Switzerland)*, 24(21):6890, 2024. Place: Basel Publisher: MDPI AG.

[40] Jaime Geisel, Madhavi Raghu, and Regina Hooley. The role of ultrasound in breast cancer screening: The case for and against ultrasound. *Seminars in ultrasound, CT, and MRI*, 39(1):25–34, 2018.

[41] S. Shen, Y. Zhou, Y. Xu, B. Zhang, X. Duan, R. Huang, B. Li, Y. Shi, Z. Shao, H. Liao, J. Jiang, N. Shen, J. Zhang, C. Yu, H. Jiang, S. Li, S. Han, J. Ma, and Q. Sun. A multi-centre randomised trial comparing ultrasound vs mammography for screening breast cancer in high-risk Chinese women. *British Journal of Cancer*, 112(6):998–1004, March 2015.

[42] Christiane K. Kuhl, Simone Schrading, Claudia C. Leutner, Nuschin Morakkabati-Spitz, Eva Wardelmann, Rolf Fimmers, Walther Kuhn, and Hans H. Schild. Mammography, breast ultrasound, and magnetic resonance imaging for surveillance of women at high familial risk for breast cancer. *Journal of Clinical Oncology*, 23(33):8469–8476, 2005. PMID: 16293877.

[43] Mieke Kriege, Cecile T.M. Brekelmans, Carla Boetes, Peter E. Besnard, Harmine M. Zonderland, Inge Marie Obdeijn, Radu A. Manoliu, Theo Kok, Hans Peterse, Madeleine M.A. Tilanus-Linthorst, Sara H. Muller, Sybren Meijer, Jan C. Oosterwijk, Louk V.A.M. Beex, Rob A.E.M. Tollenaar, Harry J. de Koning, Emiel J.T. Rutgers, and Jan G.M. Klijn. Efficacy of mri and mammography for breast-cancer screening in women with a familial or genetic predisposition. *New England Journal of Medicine*, 351(5):427–437, 2004. PMID: 15282350.

[44] Brian M Moloney, Declan O'Loughlin, Sami Abd Elwahab, and Michael J Kerin. Breast Cancer Detection-A Synopsis of Conventional Modalities and the Potential Role of Microwave Imaging. *Diagnostics (Basel)*, 10(2):103, 2020. Place: Switzerland Publisher: MDPI.

[45] Arezoo Modiri, Sally Goudreau, Asal Rahimi, and Kamran Kiasaleh. Review of breast screening: Toward clinical realization of microwave imaging. *Medical physics (Lancaster)*, 44(12):e446–e458, 2017. Place: United States.

[46] Andrea Martellosio, Massimo Bellomi, Marco Pasian, Maurizio Bozzi, Luca Perregrini, Andrea Mazzanti, Francesco Svelto, Paul Eugene Summers, Giuseppe Renne, and Lorenzo Preda. Dielectric Properties Characterization From 0.5 to 50 GHz of Breast Cancer Tissues. *IEEE transactions on microwave theory and techniques*, 65(3):998–1011, 2017. Place: New York Publisher: IEEE.

[47] Earl Zastrow, Shakti K. Davis, and Susan C. Hagness. Safety assessment of breast cancer detection via ultrawideband microwave radar operating in pulsed-radiation mode. *Microwave and optical technology letters*, 49(1):221–225, 2007. Place: Hoboken Publisher: Wiley Subscription Services, Inc., A Wiley Company.

[48] Andrea Martellosio, Marco Pasian, Maurizio Bozzi, Luca Perregrini, Andrea Mazzanti, Francesco Svelto, Paul Eugene Summers, Giuseppe Renne, Lorenzo Preda, and Massimo Bellomi. Dielectric properties characterization from 0.5 to 50 ghz of breast cancer tissues. *IEEE Transactions on Microwave Theory and Techniques*, 65(3):998–1011, 2017.

[49] Ritse M. Mann, Christiane K. Kuhl, and Linda Moy. Contrast-enhanced MRI for breast cancer screening. *Journal of magnetic resonance imaging*, 50(2):377–390, 2019. Place: Hoboken, USA Publisher: John Wiley & Sons, Inc.

[50] Lulu Wang. Microwave sensors for breast cancer detection. *Sensors*, 18(2), 2018.

[51] Atefeh Naghibi and Amir Reza Attari. Near-field radar-based microwave imaging for breast cancer detection: A study on resolution and image quality. *IEEE Transactions on Antennas and Propagation*, 69(3):1670–1680, 2021.

[52] Lulu Wang. Microwave imaging and sensing techniques for breast cancer detection. *Micromachines (Basel)*, 14(7):1462–, 2023.

[53] V. ZHURBENKO. Challenges in the design of microwave imaging systems for breast cancer detection. *Advances in electrical and computer engineering*, 11(1):91–96, 2011.

[54] Manisha Ghosh, Banani Basu, Naga Mallikarjuna Rao Dasari, V. Sivakumar Reddy, V. Kamakshi Prasad, and Jiacun Wang. Machine learning approach towards the breast cancer detection with microwave imaging. In *Intelligent Systems and Sustainable Computing*, volume 363 of *Smart Innovation, Systems and Technologies*, pages 169–177. Springer, Singapore, 2023.

[55] Mohammad Amir Mansoori and Mario R. Casu. *Hardware Acceleration of Microwave Imaging Algorithms*, pages 33–67. Springer International Publishing, Cham, 2023.

[56] L. Wang. *Basic Principles and Potential Applications of Holographic Microwave Imaging*. ASME Press, 07 2016.

[57] Raquel Cruz. Conceição, Johan Jacob. Mohr, and Martin. O'Halloran. *An Introduction to Microwave Imaging for Breast Cancer Detection*. Biological and Medical Physics, Biomedical Engineering. Springer International Publishing, Cham, 1st ed. 2016. edition, 2016.

[58] E.C. Fear, S.C. Hagness, P.M. Meaney, M. Okoniewski, and M.A. Stuchly. Enhancing breast tumor detection with near-field imaging, 2002.

[59] Seong-Ho Son, Nikolai Simonov, Hyuk-Je Kim, Jong-Moon Lee, and Soon-Ik Jeon. Preclinical prototype development of a microwave tomography system for breast cancer detection. *ETRI Journal*, 32(6):901–910, 2010.

[60] Soon-Ik Jeon, Bo-Ra Kim, and Seong-Ho Son. Clinical trial of microwave tomography imaging. In *2016 URSI Asia-Pacific Radio Science Conference (URSI AP-RASC)*, pages 1–2. IEEE, 2016.

[61] Maciej Klemm, Ian Craddock, Jack Leendertz, Alan Preece, and Ralph Benjamin. Experimental and clinical results of breast cancer detection using uwb microwave radar. In *2008 IEEE Antennas and Propagation Society International Symposium*, pages 1–4, 2008.

[62] M. Klemm, I. J. Craddock, A. Preece, J. Leendertz, and R. Benjamin. Evaluation of a hemispherical wideband antenna array for breast cancer imaging. *Radio Science*, 43(6), 2008.

[63] V ZHURBENKO, T RUBÆK, V KROZER, and P MEINCKE. Design and realisation of a microwave three-dimensional imaging system with application to breast-cancer detection. *IET microwaves, antennas & propagation*, 4(12):2200–2211, 2010.

[64] Xu Li, S.K. Davis, S.C. Hagness, D.W. van der Weide, and B.D. Van Veen. Microwave imaging via space-time beamforming: experimental investigation of tumor detection in multilayer breast phantoms. *IEEE transactions on microwave theory and techniques*, 52(8):1856–1865, 2004.

[65] E. C. Fear, J. Bourqui, C. Curtis, D. Mew, B. Docktor, and C. Romano. Microwave breast imaging with a monostatic radar-based system: A study of application to patients. *IEEE Transactions on Microwave Theory and Techniques*, 61(5):2119–2128, 2013.

[66] D. Smith, M. Leach, and A.J. Sambell. Microwave indirect holographic imaging using an adaptation of optical techniques. *IEEE Microwave and Wireless Components Letters*, 13(9):379–381, 2003.

[67] Dun Li, Paul M. Meaney, Timothy Raynolds, Sarah A. Pendergrass, Margaret W. Fanning, and Keith D. Paulsen. Parallel-detection microwave spectroscopy system for breast imaging. *Review of Scientific Instruments*, 75(7):2305–2313, 07 2004.

[68] P.M. Meaney, M.W. Fanning, Dun Li, S.P. Poplack, and K.D. Paulsen. A clinical prototype for active microwave imaging of the breast. *IEEE Transactions on Microwave Theory and Techniques*, 48(11):1841–1853, 2000.

[69] Emily Porter, Mark Coates, and Milica Popović. An early clinical study of time-domain microwave radar for breast health monitoring. *IEEE Transactions on Biomedical Engineering*, 63(3):530–539, 2016.

[70] Alan W Preece, Ian Craddock, Mike Shere, Lyn Jones, and Helen L Winton. Maria m4: clinical evaluation of a prototype ultrawideband radar scanner for breast cancer detection. *Journal of medical imaging (Bellingham, Wash.)*, 3(3):033502–033502, 2016.

[71] Yoshihiko Kuwahara, Saori Miura, Yusuke Nishina, Kaishi Mukumoto, Hiroyuki Ogura, and Harumi Sakahara. Clinical test of microwave mammography. In *2013 IEEE Antennas and Propagation Society International Symposium (APSURSI)*, pages 2028–2029, 2013.

[72] Fan Yang, Lin Sun, Zhenhua Hu, Huihai Wang, Dan Pan, Rui Wu, Xiaofeng Zhang, Yifan Chen, and Qingfeng Zhang. A large-scale clinical trial of radar-based microwave breast imaging for asian women: Phase i. In *2017 IEEE International Symposium on Antennas and Propagation & USNC/URSI National Radio Science Meeting*, pages 781–783, 2017.

[73] Hang Song, Shinsuke Sasada, Takayuki Kadoya, Morihito Okada, Koji Arihiro, Xia Xiao, and Takamaro Kikkawa. Detectability of breast tumor by a hand-held impulse-radar detector: Performance evaluation and pilot clinical study. *Scientific reports*, 7(1):16353–11, 2017.

[74] Ossama Abdel-Hamid, Abdel-rahman Mohamed, Hui Jiang, Li Deng, Gerald Penn, and Dong Yu. Convolutional neural networks for speech recognition. *IEEE/ACM Transactions on Audio, Speech, and Language Processing*, 22(10):1533–1545, 2014.

[75] Pawel Swietojanski, Arnab Ghoshal, and Steve Renals. Convolutional neural networks for distant speech recognition. *IEEE Signal Processing Letters*, 21(9):1120–1124, 2014.

[76] Leandro D. Medus, Mohamed Saban, Jose V. Francés-Víllora, Manuel Bataller-Mompeán, and Alfredo Rosado-Muñoz. Hyperspectral image classification using cnn: Application to industrial food packaging. *Food Control*, 125:107962, 2021.

[77] M. Shamim Hossain, Muneer Al-Hammadi, and Ghulam Muhammad. Automatic fruit classification using deep learning for industrial applications. *IEEE Transactions on Industrial Informatics*, 15(2):1027–1034, 2019.

[78] Ibrahim Halil Ozcan, Ozer Can Devecioglu, Turker Ince, Levent Eren, and Murat Askar. Enhanced bearing fault detection using multichannel, multilevel 1d cnn classifier. *Electrical engineering*, 104(2):435–447, 2022.

[79] Jeong Jun Lee, Deok Young Cheong, Tae Hong Min, Dong Hee Park, and Byeong Keun Choi. Cnn-based fault classification considered fault location of vibration signals. *Journal of mechanical science and technology*, 37(10):5021–5029, 2023.

[80] Mahesh Gour, Sweta Jain, and T. Sunil Kumar. Residual learning based cnn for breast cancer histopathological image classification. *International journal of imaging systems and technology*, 30(3):621–635, 2020.

[81] Yahya Alqahtani, Umakant Mandawkar, Aditi Sharma, Mohammad Najmus Saquib Hasan, Mrunalini Harish Kulkarni, and R. Sugumar. Breast cancer pathological image classification based on the multiscale cnn squeeze model. *Computational Intelligence and Neuroscience*, 2022(1):7075408, 2022.

[82] Ella Mahoro and Moulay A. Akhloufi. Breast cancer classification on thermograms using deep cnn and transformers. *Quantitative infrared thermography*, 21(1):30–49, 2024.

[83] Ling Lei, Yuwei She, Xiaoli Feng, Rui Xiong, and Shan Liu. Aircraft detection of remote sensing images based on faster r-cnn and yolov3. In *2020 International Conference on Culture-oriented Science & Technology (ICCST)*, pages 166–170, 2020.

[84] Juan M. Górriz, Javier Ramírez, Andrés Ortíz, Francisco J. Martínez-Murcia, Fermin Segovia, John Suckling, Matthew Leming, Yu-Dong Zhang, Jose Ramón Álvarez Sánchez, Guido Bologna, Paula Bonomini, Fernando E. Casado, David Charte, Francisco Charte, Ricardo Contreras, Alfredo Cuesta-Infante, Richard J. Duro, Antonio Fernández-Caballero, Eduardo Fernández-Jover, Pedro Gómez-Vilda, Manuel Graña, Francisco Herrera, Roberto Iglesias, Anna Lekova, Javier de Lope, Ezequiel López-Rubio, Rafael Martínez-Tomás, Miguel A. Molina-Cabello, Antonio S. Montemayor, Paulo Novais, Daniel Palacios-Alonso, Juan J. Pantrigo, Bryson R. Payne, Félix de la Paz López, María Angélica Pinninghoff, Mariano Rincón, José Santos, Karl Thurnhofer-Hemsi, Athanasios Tsanas, Ramiro Varela, and Jose M. Ferrández. Artificial intelligence within the interplay between natural and artificial computation: Advances in data science, trends and applications. *Neurocomputing*, 410:237–270, 2020.

[85] Mohseena Thaseen, S.K. UmaMaheswaran, Darshana A Naik, Mrunal Swapnil Aware, Prachi Pundhir, and Bhasker Pant. A review of using cnn approach for lung cancer detection through machine learning. In *2022 2nd International Conference on Advance Computing and Innovative Technologies in Engineering (ICACITE)*, pages 1236–1239, 2022.

[86] Md. Rajaul Karim, Ashifur Rahman, and Rafiqul Islam. A multi-cancer detection and localization system utilizing x-ai and ensemble technique using cnn. In *2024 6th Interna-*

tional Conference on Electrical Engineering and Information & Communication Technology (ICEEICT), pages 475–480, 2024.

[87] Nazish Khalid, Muhammad Hashir, Nasir Mahmood, Muhammad Asad, Muhammad A. Rehman, Muhammad Q. Mehmood, Muhammad Zubair, and Yehia Massoud. Efficient deep learning approaches for automated tumor detection, classification, and localization in experimental microwave breast imaging data. In *2023 IEEE International Symposium on Circuits and Systems (ISCAS)*, pages 1–4, 2023.

[88] Dawood Alsaedi, Alexander Melniko, Khalid Muzaffar, Andreas Mandelis, and Omar M. Ramahi. A microwave-thermography-convolution neural network technique for breast cancer detection. In *2021 IEEE Asia-Pacific Conference on Applied Electromagnetics (APACE)*, pages 1–2, 2021.

[89] Mariya Lazebnik, Leah McCartney, Dijana Popovic, Cynthia B Watkins, Mary J Lindstrom, Josephine Harter, Sarah Sewall, Anthony Magliocco, John H Booske, Michal Okoniewski, and Susan C Hagness. A large-scale study of the ultrawideband microwave dielectric properties of normal breast tissue obtained from reduction surgeries. *Physics in medicine & biology*, 52(10):2637–2656, 2007.

[90] Mariya Lazebnik, Dijana Popovic, Leah McCartney, Cynthia B Watkins, Mary J Lindstrom, Josephine Harter, Sarah Sewall, Travis Ogilvie, Anthony Magliocco, Tara M Breslin, Walley Temple, Daphne Mew, John H Booske, Michal Okoniewski, and Susan C Hagness. A large-scale study of the ultrawideband microwave dielectric properties of normal, benign and malignant breast tissues obtained from cancer surgeries. *Physics in Medicine & Biology*, 52(20):6093, oct 2007.

[91] C. Gabriel. *The Dielectric Properties of Tissues*, pages 75–84. Springer Netherlands, Dordrecht, 2000.

[92] E Zastrow, S K Davis, M Lazebnik, F Kelcz, B D Van Veen, and S C Hagness. *Database of 3D Grid-Based Numerical Breast Phantoms for use inComputational Electromagnetics Simulations.*

[93] Martin Sonnenschein. Atlas of breast tomosynthesis : imaging findings and image-guided interventions, 2017.

[94] The MathWorks Inc. Matlab® version: 9.12.0.2009381 (r2022a) update 4, 2022.

[95] CST Studio Suite®. Cst® copyright 1998-2019 dassault systemes deutschland gmbh. all rights reserved., 2020.

[96] E. Zastrow, S. K. Davis, M. Lazebnik, F. Kelcz, B. D. Van Veen, and S. C. Hagness. *Database of 3D Grid-Based Numerical Breast Phantoms for use in Computational Electromagnetics Simulations*. Department of Electrical and Computer Engineering University of Wisconsin-Madison.

[97] Antonio Sarno, Giovanni Mettivier, Francesca di Franco, Antonio Varallo, Kristina Bliznakova, Andrew M. Hernandez, John M. Boone, and Paolo Russo. Dataset of patient-derived digital breast phantoms for in silico studies in breast computed tomography, digital breast tomosynthesis, and digital mammography. *Medical Physics*, 48(5):2682–2693, 2021.

[98] Ashim K. Datta and Ramaswamy C. Anantheswaran. *Handbook of microwave technology for food applications*. Food science and technology ; 109. Marcel Dekker, New York, 2001.

[99] Siying Qi, Jiping Han, Camel Lagnika, Ning Jiang, Chunlu Qian, Chunquan Liu, Dajing Li, Yang Tao, Zhifang Yu, Libin Wang, Zhongyuan Zhang, Chunju Liu, Yadong Xiao, and Min Zhang. Dielectric properties of edible fungi powder related to radio-frequency and microwave drying. *Food production, processing and nutrition*, 3(1):1–13, 2021.

[100] Viktor G Veselago. The electrodynamics of substances with simultaneously negative values of ϵ and μ. *Soviet physics. Uspekhi*, 10(4):509–514, 1968.

[101] Amit Kumar Singh. *Metamaterials for antenna applications*. CRC Press, Boca Raton, FL, 2022.

[102] N I Landy, S Sajuyigbe, J J Mock, D R Smith, and W J Padilla. Perfect metamaterial absorber. *Physical review letters*, 100(20):207402–207402, 2008.

[103] Thamer S. Almoneef and Omar M. Ramahi. Metamaterial electromagnetic energy harvester with near unity efficiency. *Applied physics letters*, 106(15):153902–, 2015.

[104] Christopher L. Holloway, Edward F. Kuester, Joshua A. Gordon, John O'Hara, Jim Booth, and David R. Smith. An overview of the theory and applications of metasurfaces: The two-dimensional equivalents of metamaterials. *IEEE Antennas and Propagation Magazine*, 54(2):10–35, 2012.

[105] Dawood Alsaedi, Mohamed El Badawe, and Omar M. Ramahi. A breast cancer detection system using metasurfaces with a convolution neural network: A feasibility study. *IEEE transactions on microwave theory and techniques*, 70(7):3566–3576, 2022.

[106] Hou-Tong Chen, Antoinette J Taylor, and Nanfang Yu. A review of metasurfaces: physics and applications. *Reports on progress in physics*, 79(7):076401–076401, 2016.

[107] Vasileios G Ataloglou, Sajjad Taravati, and George V Eleftheriades. Metasurfaces: physics and applications in wireless communications. *National science review*, 10(8):nwad164–nwad164, 2023.

[108] Omar M. Ramahi, Thamer S. Almoneef, Mohammed AlShareef, and Muhammed S. Boybay. Metamaterial particles for electromagnetic energy harvesting. *Applied Physics Letters*, 101(17):173903, 10 2012.

[109] Aobo Li, Shreya Singh, and Dan Sievenpiper. Metasurfaces and their applications. *Nanophotonics*, 7(6):989–1011, 2018.

[110] Mahdiyeh Shamsi and Jalil Pirayesh Islamian. Breast cancer: early diagnosis and effective treatment by drug delivery tracing. *Nuclear medicine review. Central & Eastern Europe*, 20(1):45–48, 2017.

[111] Shay Shraga, Albert Grinshpun, Aviad Zick, Luna Kadouri, Yogev Cohen, Ofra Maimon, Yael Adler-Levy, Galina Zeltzer, Avital Granit, Bella Maly, Einat Carmon, Vardiella Meiner, Tamar Sella, Tamar Hamburger, and Tamar Peretz. "high-risk breast cancer screening in brca1/2 carriers leads to early detection and improved survival after a breast cancer diagnosis". *Frontiers in Oncology*, 11, 2021.

[112] UK M G Marmot, D G Altman, D A Cameron, J A Dewar, S G Thompson, and Maggie Wilcox. The benefits and harms of breast cancer screening: an independent review. *The Lancet (British edition)*, 380(9855):1778–1786, 2012.

[113] Madeleine Hertel, Resam Makvandi, Steffen Kappler, Ralf Nanke, Petra Bildhauer, Sylvia Saalfeld, Marcus Radicke, Daniel Juhre, and Georg Rose. Towards a biomechanical breast model to simulate and investigate breast compression and its effects in mammography and tomosynthesis. *Physics in Medicine & Biology*, 68(8):085007, apr 2023.

[114] Daniel B Kopans. Antecedents: A Half-Century of Imaging the Breast. *Journal of Breast Imaging*, 1(1):2–8, 03 2019.

[115] Baoying Chen, Yingmei Wang, Xin Sun, Wei Guo, Ming Zhao, Guangbin Cui, Lina Hu, Pei Li, Yan Ren, Jun Feng, and Jun Yu. Analysis of patient dose in full field digital mammography. *European Journal of Radiology*, 81(5):868–872, 2012.

[116] Robert S Saunders, Jr, Ehsan Samei, Joseph Y Lo, and Jay A Baker. Can compression be reduced for breast tomosynthesis? monte carlo study on mass and microcalcification conspicuity in tomosynthesis. *Radiology*, 251(3):673–682, 2009.

[117] The uwcem numerical breast phantom repository.

[118] W. Paul Segars, Alexander I Veress, Jered R Wells, Gregory M Sturgeon, Nooshin Kiarashi, Joseph Y Lo, Ehsan Samei, James T Dobbins, Christoph Hoeschen, and Bruce R Whiting. Population of 100 realistic, patient-based computerized breast phantoms for multi-modality imaging research. In *Population of 100 realistic, patient-based computerized breast phantoms for multi-modality imaging research*, volume 9033, pages 90331X–90331X–6. SPIE, 2014.

[119] Andriy Fedorov, Reinhard Beichel, Jayashree Kalpathy-Cramer, Julien Finet, Jean-Christophe Fillion-Robin, Sonia Pujol, Christian Bauer, Dominique Jennings, Fiona Fennessy, Milan Sonka, John Buatti, Stephen Aylward, James V Miller, Steve Pieper, and Ron Kikinis. 3d slicer as an image computing platform for the quantitative imaging network. *Magnetic resonance imaging*, 30(9):1323–1341, 2012.

[120] Paolo Cignoni, Marco Callieri, Massimiliano Corsini, Matteo Dellepiane, Fabio Ganovelli, and Guido Ranzuglia. Meshlab: an open-source mesh processing tool. In *MeshLab: an Open-Source Mesh Processing Tool.*, volume 1, pages 129–136, 01 2008.

[121] the open source system for processing and editing 3D triangular meshes. It provides a set of tools for editing, cleaning, healing, inspecting, rendering, texturing and converting meshes. It offers features for processing raw data produced by 3D digitization tools/devices and for preparing models for 3D printing., howpublished = https://www.meshlab.net/. Accessed: 2024-12-31.

[122] Steve A Maas, Benjamin J Ellis, Gerard A Ateshian, and Jeffrey A Weiss. Febio: Finite elements for biomechanics. *Journal of biomechanical engineering*, 134(1):011005–10, 2012.

[123] N. Perry, M. Broeders, C. de Wolf, S. Törnberg, R. Holland, and L. von Karsa. European guidelines for quality assurance in breast cancer screening and diagnosis. fourth edition—summary document. *Annals of oncology*, 19(4):614–622, 2008.

[124] E. K. Hughes, L. Nassar, A. Lim, N. Barrett, S. Comitis, D. Cunningham, S. Flais, A. Gupta, G. Ralleigh, V. Stewart, W. Svensson, R. Williamson, N. Zaman, and K. Satchithananda. Automated breast volume scanner: an initial experience. *Breast Cancer Research*, 13(1):O1, 2011.

[125] Citation:Vajuhudeen Z, Schmidt R, and Haouimi A. Compression in mammography. *Reference article, Radiopaedia. org (Accessed on*, 24, 2020.

[126] Koichi Chida, Yuka Komatsu, Masahiro Sai, Asuka Nakagami, Takayuki Yamada, Takuya Yamashita, Issei Mori, Tadashi Ishibashi, Shin Maruoka, and Masayuki Zuguchi. Reduced compression mammography to reduce breast pain. *Clinical Imaging*, 33(1):7–10, 2009.

[127] Mireille J. M. Broeders, Marloes ten Voorde, Wouter J. H. Veldkamp, Ruben E. van Engen, Cary van Landsveld – Verhoeven, Machteld N. L. 't Jong – Gunneman, Jos de Win, Kitty Droogh-de Greve, Ellen Paap, and Gerard J. den Heeten. Comparison of a flexible versus a rigid breast compression paddle: pain experience, projected breast area, radiation dose and technical image quality. *European radiology*, 25(3):821–829, 2015.

[128] W. Boonzaier and S. Acho. O53. dosimetric data for diagnostic digital mammography employing fully automated self adjusting tilt compression. *Physica Medica*, 32:159, 2016. Abstracts of the 54th National Congress of the South African Association of Physicists in Medicine and Biology (SAAPMB).

[129] Claire E. Mercer, Katy Szczepura, Judith Kelly, Sara R. Millington, Erika R.E. Denton, Rita Borgen, Beverley Hilton, and Peter Hogg. A 6-year study of mammographic compression force: Practitioner variability within and between screening sites. *Radiography*, 21(1):68–73, 2015.

[130] Hang Si. Tetgen, a delaunay-based quality tetrahedral mesh generator. *ACM Trans. Math. Softw.*, 41(2), feb 2015.

[131] A. Pérez del Palomar, B Calvo, J Herrero, J López, and M Doblaré. A finite element model to accurately predict real deformations of the breast. *Medical engineering & physics*, 30(9):1089–1097, 2008.

[132] J. A. Solves Llorens, M. J. Rupérez, C. Monserrat, E. Feliu, M. García, and M. Lloret. Segmentation of the breast skin and its influence in the simulation of the breast compression during an x-ray mammography. *TheScientificWorld*, 2012:876489–8, 2012.

[133] Alok Sutradhar and Michael J. Miller. In vivo measurement of breast skin elasticity and breast skin thickness. *Skin research and technology*, 19(1):e191–e199, 2013.

[134] Christian G Graff, Joseph Y Lo, Despina Kontos, and Thomas G Flohr. A new, open-source, multi-modality digital breast phantom. volume 9783, pages 978309–978309–10. SPIE, 2016.

[135] Maximilian Eder, Fee v. Waldenfels, Alexandra Swobodnik, Markus Klöppel, Ann-Kathrin Pape, Tibor Schuster, Stefan Raith, Elena Kitzler, Nikolaos A. Papadopulos, Hans-Günther Machens, and Laszlo Kovacs. Objective breast symmetry evaluation using 3-D surface imaging. *The Breast*, 21(2):152–158, April 2012.

[136] Yoshihiko Kuwahara and Tomoya Ozaki. Radar imaging using bilateral symmetry of breast tissue. In *2018 48th European Microwave Conference (EuMC)*, pages 499–502, 2018.

[137] Marianne Holm, Anne Tjønneland, Eva Balslev, and Niels Kroman. Prognosis of synchronous bilateral breast cancer: a review and meta-analysis of observational studies. *Breast cancer research and treatment*, 146(3):461–475, 2014.

[138] Evgeny N Imyanitov and Kaido P Hanson. Molecular pathogenesis of bilateral breast cancer. *Cancer Letters*, 191(1):1–7, 2003.

[139] S.M Schmid, C Pfefferkorn, M.E Myrick, C.T Viehl, E Obermann, A Schötzau, and U Güth. Prognosis of early-stage synchronous bilateral invasive breast cancer. *European journal of surgical oncology*, 37(7):623–628, 2011.

[140] Ankita Dey, Ebrahim Ali, and Sreeraman Rajan. Bilateral symmetry-based abnormality detection in breast thermograms using textural features of hot regions. *IEEE Open Journal of Instrumentation and Measurement*, 2:1–14, 2023.

[141] Sagar E Shirsath, R H Kadam, K M Batoo, Danyang Wang, and Sean Li. Co-al-substituted strontium hexaferrite for rare earth free permanent magnet and microwave absorber application. *Journal of physics. D, Applied physics*, 54(2):24001–, 2021.

[142] Mengqiu Huang, Lei Wang, Wenbin You, and Renchao Che. Single zinc atoms anchored on mof-derived n-doped carbon shell cooperated with magnetic core as an ultrawideband microwave absorber. *Small (Weinheim an der Bergstrasse, Germany)*, 17(30):e2101416–n/a, 2021.

[143] W. J. Padilla, M. T. Aronsson, C. Highstrete, Mark Lee, A. J. Taylor, and R. D. Averitt. Electrically resonant terahertz metamaterials: Theoretical and experimental investigations. *Physical review. B, Condensed matter and materials physics*, 75(4), 2007.

[144] Paul I. Deffenbaugh, Raymond C. Rumpf, and Kenneth H. Church. Broadband microwave frequency characterization of 3-d printed materials. *IEEE Transactions on Components, Packaging and Manufacturing Technology*, 3(12):2147–2155, 2013.

[145] Jacob D. Shea, Panagiotis Kosmas, Susan C. Hagness, and Barry D. Van Veen. Three-dimensional microwave imaging of realistic numerical breast phantoms via a multiple-frequency inverse scattering technique. *Medical Physics*, 37(8):4210–4226, 2010.

[146] N. Dalal and B. Triggs. Histograms of oriented gradients for human detection. In *2005 IEEE Computer Society Conference on Computer Vision and Pattern Recognition (CVPR'05)*, volume 1, pages 886–893 vol. 1. IEEE, 2005.

[147] Alireza Dehghani, David Moloney, and Xiaofan Xu. Face detection speed improvement using bitmap-based histogram of oriented gradien. In *2017 International Conference on Systems, Signals and Image Processing (IWSSIP)*, pages 1–5. IEEE, 2017.

[148] Divyesh Khanvilkar and Abhishek Bhatt. Skin cancer detection from rgb images using the lbp and hog texture feature descriptors with help of machine learning algorithm. In *2022 International Conference on Signal and Information Processing (IConSIP)*, pages 1–5. IEEE, 2022.

[149] Sevcan Aytaç Korkmaz and Hamidullah Binol. Classification of molecular structure images by using ann, rf, lbp, hog, and size reduction methods for early stomach cancer detection. *Journal of molecular structure*, 1156:255–263, 2018.

[150] Stefania Romeo, Loreto Di Donato, Ovidio Mario Bucci, Ilaria Catapano, Lorenzo Crocco, Maria Rosaria Scarfi, and Rita Massa. Dielectric characterization study of liquid-based materials for mimicking breast tissues. *Microwave and optical technology letters*, 53(6):1276–1280, 2011.

[151] Guido Van Rossum and Fred L. Drake. *Python 3 Reference Manual*. CreateSpace, Scotts Valley, CA, 2009.

[152] The pandas development team. pandas-dev/pandas: Pandas, February 2020.

[153] Wes McKinney. Data Structures for Statistical Computing in Python. In Stéfan van der Walt and Jarrod Millman, editors, *Proceedings of the 9th Python in Science Conference*, pages 56 – 61, 2010.

[154] J. D. Hunter. Matplotlib: A 2d graphics environment. *Computing in Science & Engineering*, 9(3):90–95, 2007.

[155] Charles R. Harris, K. Jarrod Millman, Stéfan J. van der Walt, Ralf Gommers, Pauli Virtanen, David Cournapeau, Eric Wieser, Julian Taylor, Sebastian Berg, Nathaniel J. Smith, Robert Kern, Matti Picus, Stephan Hoyer, Marten H. van Kerkwijk, Matthew Brett, Allan Haldane, Jaime Fernández del Río, Mark Wiebe, Pearu Peterson, Pierre Gérard-Marchant, Kevin Sheppard, Tyler Reddy, Warren Weckesser, Hameer Abbasi, Christoph Gohlke, and Travis E. Oliphant. Array programming with NumPy. *Nature*, 585(7825):357–362, September 2020.

[156] Adam Paszke, Sam Gross, Soumith Chintala, Gregory Chanan, Edward Yang, Zachary DeVito, Zeming Lin, Alban Desmaison, Luca Antiga, and Adam Lerer. Automatic differentiation in pytorch. In *NIPS-W*, 2017.

[157] Itseez. *The OpenCV Reference Manual*, 2.4.9.0 edition, April 2014.

[158] L Tabar, SW Duffy, B Vitak, H-H Chen, and UB Krusemo. The swedish two-county trial 20-years on: updated mortality results and new insights from long-term follow-up. *Breast cancer research : BCR*, 2(Suppl 2):A3–A3, 2000.

[159] S Koscielny, M Tubiana, M G Lê, A J Valleron, H Mouriesse, G Contesso, and D Sarrazin. Breast cancer: Relationship between the size of the primary tumour and the probability of metastatic dissemination. *British journal of cancer*, 49(6):709–715, 1984.

[160] Maximilian Eder, Fee v Waldenfels, Alexandra Swobodnik, Markus Klöppel, Ann-Kathrin Pape, Tibor Schuster, Stefan Raith, Elena Kitzler, Nikolaos A Papadopulos, Hans-Günther Machens, and Laszlo Kovacs. Objective breast symmetry evaluation using 3-d surface imaging. *Breast (Edinburgh)*, 21(2):152–158, 2012.

[161] Amit K. Singh, Mahesh P. Abegaonkar, and Shiban Kishen Koul. Miniaturization of microstrip patch antennas using metamaterials. In *Metamaterials for Antenna Applications*, pages 37–75. CRC Press, 1 edition, 2022.

[162] Zeyang Zhang, Xiangxuan Liu, Xuanjun Wang, Youpeng Wu, and Rong Li. Effect of nd–co substitution on magnetic and microwave absorption properties of srfe12o19 hexaferrites. *Journal of Alloys and Compounds*, 525:114–119, 2012.

[163] J.G. Lyng, L. Zhang, and N.P. Brunton. A survey of the dielectric properties of meats and ingredients used in meat product manufacture. *Meat Science*, 69(4):589–602, 2005.

[164] K.W. Farag, J.G. Lyng, D.J. Morgan, and D.A. Cronin. Dielectric and thermophysical properties of different beef meat blends over a temperature range of -18° to +10°c. *Meat Science*, 79(4):740–747, 2008.

[165] Stephen Wolfram. Statistical mechanics of cellular automata. *Reviews of modern physics*, 55(3):601–644, 1983.

[166] Yanxia Liu, Lotfollah Shafai, Dustin Isleifson, and Cyrus Shafai. Split ring antennas and their application for antenna miniaturization. *Sensors (Basel, Switzerland)*, 23(2):846–, 2023.

[167] Ahmed M. Hassan and Magda El-Shenawee. Review of electromagnetic techniques for breast cancer detection. *IEEE Reviews in Biomedical Engineering*, 4:103–118, 2011.

[168] Sarah Benmazou, Hayet Farida Merouani, Soumia Layachi, and Beledjhem Nedjmeddine. Classification of mammography images based on cellular automata and haralick parameters. *Evolving systems*, 5(3):209–216, 2014.

[169] D. Byrne, M. O'Halloran, E. Jones, and M. Glavin. Support vector machine-based ultrawideband breast cancer detection system. *Journal of electromagnetic waves and applications*, 25(13):1807–1816, 2011.

[170] Adam Santorelli, Yunpeng Li, Emily Porter, Milica Popovic, and Mark Coates. Investigation of classification algorithms for a prototype microwave breast cancer monitor. In *The 8th European Conference on Antennas and Propagation (EuCAP 2014)*, pages 320–324. European Association on Antennas and Propagation, 2014.

[171] Samaneh Aminikhanghahi, Sung Shin, Wei Wang, Seong Son, and Soon Jeon. An optimized support vector machine classifier to extract abnormal features from breast microwave tomography data. In *Proceedings of the 2014 Conference on research in adaptive and convergent systems*, RACS '14, pages 111–115. ACM, 2014.

[172] Jenni A M Sidey-Gibbons and Chris J Sidey-Gibbons. Machine learning in medicine: a practical introduction. *BMC medical research methodology*, 19(1):64–64, 2019.

[173] Colin. Campbell. *Learning with support vector machines*. Synthesis lectures on artificial intelligence and machine learning, # 10. Morgan & Claypool, San Rafael, Calif. (1537 Fourth Street, San Rafael, CA 94901 USA), 2011.

[174] Maheshwar and Gautam Kumar. Breast cancer detection using decision tree, naïve bayes, knn and svm classifiers: A comparative study. In *2019 International Conference on Smart Systems and Inventive Technology (ICSSIT)*, pages 683–686, 2019.

[175] J Quinlan. Learning decision tree classifiers. *ACM computing surveys*, 28(1):71–72, 1996.

[176] Hyun-chong Cho, Lubomir Hadjiiski, Berkman Sahiner, Heang-Ping Chan, Mark Helvie, Chintana Paramagul, and Alexis V. Nees. A similarity study of content-based image retrieval system for breast cancer using decision tree. *Medical physics (Lancaster)*, 40(1):012901–n/a, 2013.

[177] N. Karssemeijer and G.M. te Brake. Detection of stellate distortions in mammograms. *IEEE transactions on medical imaging*, 15(5):611–619, 1996.

[178] H.D. Cheng, X.J. Shi, R. Min, L.M. Hu, X.P. Cai, and H.N. Du. Approaches for automated detection and classification of masses in mammograms. *Pattern recognition*, 39(4):646–668, 2006.

[179] W. R. Ashby. Principles of the self-organizing dynamic system. *The Journal of general psychology*, 37(2):125–128, 1947.

[180] R. Doursat. The myriads of alife: Importing complex systems and self-organization into engineering. In *2011 IEEE Symposium on Artificial Life (ALIFE)*, pages 1–8. IEEE, 2011.

[181] Edward N. Trifonov. Vocabulary of definitions of life suggests a definition. *Journal of biomolecular structure & dynamics*, 29(2):259–266, 2011.

[182] Carlos Gershenson, Vito Trianni, Justin Werfel, and Hiroki Sayama. Self-organization and artificial life. *Artificial life*, 26(3):391–408, 2020.

[183] Carlos Gershenson and Dirk Helbing. When slower is faster. *Complexity (New York, N.Y.)*, 21(2):9–15, 2015.

[184] Xin-She Yang and Y. Young. Cellular automata, pdes, and pattern formation, 2010.

[185] E. Golees and Servet Martiinez. *Cellular automata and complex systems*. Nonlinear Phenomena and Complex Systems ; Volume 3. Springer Science+Business Media, B.V., Dordrecht, 1st ed. 1999. edition, 1999.

[186] Hiroki Sayama. A new structurally dissolvable self-reproducing loop evolving in a simple cellular automata space. *Artificial life*, 5(4):343–365, 1999.

[187] Yu-Cih Peng and Chung-I Chou. Simulation of pedestrian flow through a "t" intersection: A multi-floor field cellular automata approach. *Computer physics communications*, 182(1):205–208, 2011.

[188] Hossein Nikravesh Matin and Saeed Setayeshi. A computational tumor growth model experience based on molecular dynamics point of view using deep cellular automata. *Artificial intelligence in medicine*, 148:102752–102752, 2024.

[189] Lotfi Ladhar, Mohamed Zarouan, Donia Oueslati, Jean-Marie Floch, and Hatem Rmili. Investigation on cellular-automata irregular-fractal ultrawideband slot-antennas. *Microwave and optical technology letters*, 57(11):2506–2514, 2015.

[190] Iulia-Andreea Ion, Cristiana Moroz-Dubenco, and Anca Andreica. Breast cancer images segmentation using fuzzy cellular automaton. *Procedia computer science*, 225:999–1008, 2023.

[191] Surasak Tangsakul and Sartra Wongthanavasu. Deep cellular automata-based feature extraction for classification of the breast cancer image. *Applied sciences*, 13(10):6081–, 2023.

[192] Xiaoran Lai, Håkon A. Taskén, Torgeir Mo, Simon W. Funke, Arnoldo Frigessi, Marie E. Rognes, and Alvaro Köhn-Luque. A scalable solver for a stochastic, hybrid cellular automaton model of personalized breast cancer therapy. *International journal for numerical methods in biomedical engineering*, 38(1):e3542–n/a, 2022.

[193] Tom Fawcett. Data mining with cellular automata. *SIGKDD explorations*, 10(1):32–39, 2008.

[194] Andrew. Adamatzky. *Game of life cellular automata*. Springer, London, 1st. ed. edition, 2010.

[195] Martin Gardner. Mathematical games: The fantastic combinations of john conway's new solitaire game "life", 1970.

[196] Oliver Kramer. Chapter 2 - genetic algorithms. In *Genetic algorithm essentials*, Studies in computational intelligence, volume 679, pages 11–12. Springer, Cham, Switzerland, 2017.

[197] Melanie Mitchell, Peter Hraber, and James P. Crutchfield. Revisiting the edge of chaos: Evolving cellular automata to perform computations, 1993.

[198] Anna Piwonska, Franciszek Seredynski, and Miroslaw Szaban. Learning cellular automata rules for binary classification problem. *The Journal of supercomputing*, 63(3):800–815, 2013.

[199] Antonio Sarno, Giovanni Mettivier, Francesca Franco, Antonio Varallo, Kristina Bliznakova, Andrew M. Hernandez, John M. Boone, and Paolo Russo. Dataset of patient-derived digital breast phantoms for in silico studies in breast computed tomography, digital breast tomosynthesis, and digital mammography. *Medical physics (Lancaster)*, 48(5):2682–2693, 2021.

[200] NanoVNA is a handheld Vector Network Analyzer (VNA), howpublished = https://nanovna.com. Accessed: 2024-12-30.

[201] NanoVNA-App is the very powerful windows software developed by OneOfEleven for NanoVNA and LibreVNA., howpublished = https://nanovna.com/?page_id=141. Accessed: 2024-12-30.